Forschungszentrum Jülich
in der Helmholtz-Gemeinschaft
50 Jahre / Zukunft

Piezoresponse Force Microscopy and Surface Effects of Perovskite Ferroelectric Nanostructures

Frank Peter

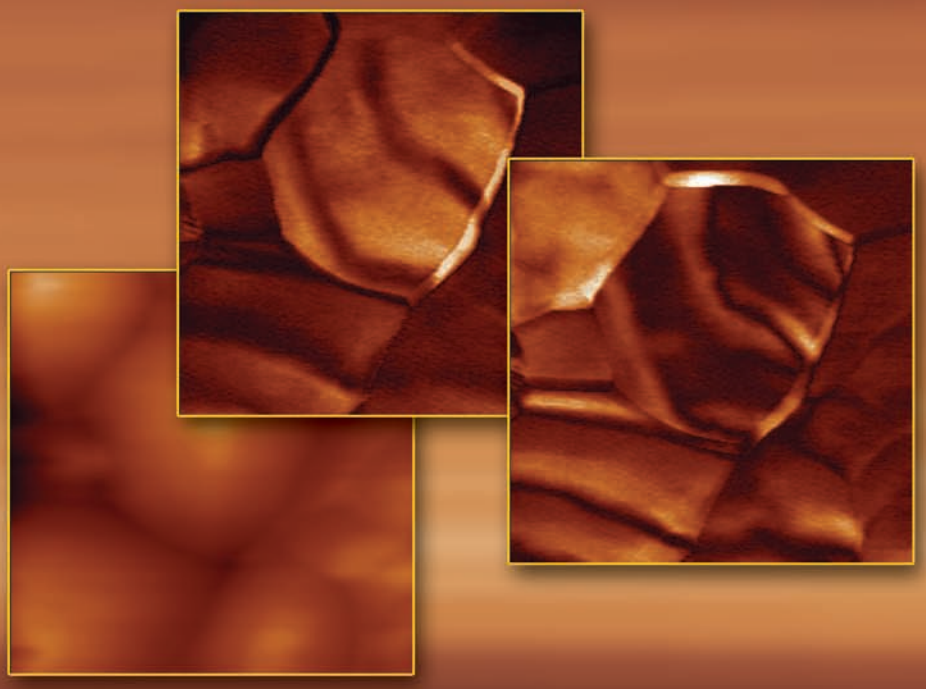

Informationstechnik
Information Technology

Schriften des Forschungszentrums Jülich
Reihe Informationstechnik / Information Technology Band / Volume 11

Forschungszentrum Jülich GmbH
Institut für Festkörperforschung:
Elektronische Materialien

Piezoresponse Force Microscopy and Surface Effects of Perovskite Ferroelectric Nanostructures

Frank Peter

Schriften des Forschungszentrums Jülich
Reihe Informationstechnik / Information Technology Band / Volume 11

ISSN 1433-5514 ISBN 3-89336-444-7

Bibliographic information published by Die Deutsche Bibliothek.
Die Deutsche Bibliothek lists this publication in the Deutsche Nationalbibliografie; detailed bibliographic data is available in the Internet at <http://dnb.ddb.de>.

Publisher and Distributor: Forschungszentrum Jülich GmbH
Zentralbibliothek, Verlag
52425 Jülich
Phone: +49 2461 61-5368 · Telefax: +49 2461 61-6103
e-mail: zb-publikation@fz-juelich.de
Internet: http://www.fz-juelich.de/zb

Cover Design: Grafische Betriebe, Forschungszentrum Jülich GmbH

Printer: Grafische Betriebe, Forschungszentrum Jülich GmbH

Schriften des Forschungszentrums Jülich
Reihe Informationstechnik / Information Technology Band / Volume 11

D 82 (Diss., Aachen, RWTH, 2006)

ISSN 1433-5514
ISBN-10: 3-89336-444-7
ISBN-13: 978-3-89336-444-2

Abstract

With the advancing miniaturization of ferroelectric, non-volatile memories, the question arises how the spontaneous polarization and the displacement current scale with size. Piezoresponse Force Microscopy (PFM) is the method of choice to study these properties. Notwithstanding the huge success of this method, many aspects of the contrast formation mechanisms are not yet understood. The aim of this work is a systematic investigation of the intrinsic and extrinsic contributions to PFM measurements of ferroelectric nanostructures.

X-Ray Photoelectron Spectroscopy and PFM measurements confirm that perovskite ferroelectrics are covered by adsorbates under ambient conditions. In PFM this leads to a severe reduction of the electric field applied to the sample and attenuates the piezoresponse by up to one order of magnitude. Heat treatment in high vacuum is successfully employed to lessen the amount and impact of adsorbates and to substantially recover the piezoresponse.

Due to the cantilever geometry the optical amplification for the in-plane response is about 20 times larger than for the out-of-plane response. This large optical amplification makes the in-plane piezoresponse measurements highly attractive. However, in c-axis oriented thin films no in-plane piezoresponse should be detected at all due to the radial potential distribution underneath the tip. Measurements and simulations are presented showing that an in-plane response can be detected whenever the radial symmetry is broken. This can be due to an asymmetric cantilever, local variations of material parameters or an uneven surface.

Especially on the slopes of ferroelectric nanoislands, the topography has a significant influence on the in-plane PFM signal. As a result of the broken symmetry of the radial potential distribution and the unbalanced amount of material underneath the tip a significant enhancement of the in-plane response occurs at the perimeter even of c-axis oriented grains. Due to the cantilever geometry, this enhancement is restricted to slopes of the grain parallel to the axis of the cantilever. However, the enhancement may also be observed on the slopes perpendicular to the cantilever-axis in out-of-plane measurements as a result of a mechanical crosstalk.

Another kind of crosstalk originates from a misalignment of the cantilever with respect to the four sector photo diode. In this case the pronounced in-plane response supersedes the out-of-plane signal and in some lateral force microscopy configurations this may even result in the in-plane signal impacting the z-feedback-loop of the Atomic Force Microscope. A novel mechanical compensation scheme is suggested to eliminate this crosstalk.

Similar to other imaging measurement techniques, PFM suggests a very intuitive access to the acquired data. In this sense the present work addresses new critical aspects of the measurement technique with an emphasis on the tip-sample interaction in the presence of adsorbates.

Kurzfassung

Mit der fortschreitenden Miniaturisierung ferroelektrischer, nicht-flüchtiger Speicher stellt sich die Frage, wie die Spontanpolarisation und damit der verfügbare Verschiebungsstrom mit der Größse skalieren. Diese Eigenschaften lassen sich sehr gut mittels der piezoelektrischen Rasterkraftmikroskopie (engl.: PFM) untersuchen. Ungeachtet des großen Erfolgs der Methode sind viele Aspekte der Kontrastbildung noch nicht verstanden. Das Ziel dieser Arbeit ist die systematische Untersuchung der intrinsischen und extrinsischen Beiträge zu PFM-Messungen von ferroelektrischen Nanostrukturen.

Mittels Röntgenstrahl-Photoelektronen Spektroskopie und PFM wird gezeigt, dass ferroelektrische Perowskite unter normalen Bedingungen mit einer Adsorbatschicht bedeckt sind. Diese Schicht reduziert als Spannungsteiler das angelegte Feld und damit die PFM-Antwort um etwa eine Größenordnung. Im Rahmen dieser Arbeit wird eine Methode entwickelt, die durch thermische Behandlung im Hochvakuum den Einfluss der Adsorbate auf die Messung reduziert.

Aufgrund der Cantilevergeometrie ist die optische Verstärkung lateraler PFM-Messungen etwa 20mal höher als die vertikaler, wodurch diese Messart erheblich an Attraktivität gewinnt. Es blieb die Frage, wieso auf axial-symmetrischen, c-Achsen orientierten Proben überhaupt eine laterale Piezoantwort detektiert werden kann, die aus Symmetriegründen verboten ist. In der vorliegenden Arbeit werden verschiedene Szenarien, in denen die axiale Symmetrie unter der PFM-Spitze gebrochen wird, aufgeführt und experimentell oder numerisch überprüft.

Insbesondere die Topographie hat einen erheblichen Einfluss auf die Piezoantwort von Nanoinseln. Am Rande der Inseln sorgt die gebrochene Symmetrie der radialen Spannungsverteilung unter der Spitze für eine erhebliche Überhöhung des gemessenen lateralen PFM-Signals. Bedingt durch die Messanordnung kann diese Überhöhung in dem lateralen Signal nur an dem oberen und unteren Rand von Körnern beobachtet werden. Die im vertikalen Kanal detektierbare Randüberhöhung wird verursacht durch ein mechanisches Übersprechen.

Ist die Vier-Quadranten-Photodiode des Rasterkraftmikroskops nicht exakt zum Cantilever ausgerichtet, führt eine laterale Bewegung zu einem vertikalen Signal. Zudem beeinflusst manche laterale Bewegung die Nachregelung in z-Richtung und damit auch die gemessene Topographie. Dieser Effekt fällt stark ins Gewicht, da die optische Verstärkung in lateraler Richtung erheblich stärker ist als in vertikaler. Ein neues, im Rahmen dieser Arbeit entwickeltes Verfahren gewährleistet eine zuverlässige Unterdrückung des Übersprechens.

Bei sorgfältiger Berücksichtigung der hier aufgezeigten Besonderheiten stellt die PFM eine vielseitige Methode mit ausgesprochen hoher Ortsauflösung für die Untersuchung ferroelektrischer Nanostrukturen dar.

Contents

Abbreviations

AFM Atomic Force Microscopy

BTO $BaTiO_3$

CSD Chemical Solution Deposition

FEM Finite Element Method

HSQ Hydrogen Silsesquioxane

KNO $KNbO_3$

PFM Piezoresponse Force Microscopy

PLD Pulsed Laser Deposition

PZT $Pb(Zr,Ti)O_3$

PTO $PbTiO_3$

SEM Scanning Electron Microscopy

SPM Scanning Probe Microscopy

STM Scanning Tunneling Microscopy

SRO $SrRuO_3$

STO $SrTiO_3$

UHV Ultra High Vacuum

XPS X-ray Photoelectron Spectroscopy

1 Introduction

1.1 Motivation

A ferroelectric is a polar material exhibiting a spontaneous polarization P_S that can be reversed by an external electric field. All ferroelectrics are also pyroelectric and piezoelectric. Pyroelectricity was first reported by the ancient Greeks 400 B.C. [1]. Piezoelectricity is known since 1880 [2], but it was only in 1920 that Joseph Valasek discovered the ferroelectric properties of Rochelle Salt [3].

Since charged adsorbates are omnipresent under ambient conditions, the bound surface charges of the spontaneous polarization are thoroughly compensated and therefore virtually impossible to detect in a steady state. Both pyroelectricity and piezoelectricity are transient effects that disturb this equilibrium. The charge compensation process may even be visible to the naked eye as e.g. reported in 1707: "... a precious stone called tourmaline, turmale, or tip, which had the property of not only attracting the ashes from the warm or burning coals, as the magnet does iron, but also repelling them again." [4]. In contrast, the observation of ferroelectricity explicitly requires the polarization reversal in an external electric circuit.

From the 1940's ferroelectric materials found their way into many applications based on their dielectric properties (capacitors), piezoelectric attributes (electric lighter, sensors and actuators), pyroelectric features (temperature sensors and thermal imaging) as well as their nonlinear optical properties (holographic data storage, optical transistors, optical multiplexer) [5, 6].

The developments of deposition techniques for epitaxial thin films and advanced ceramic fabrication have resulted in numerous novel applications such as micro- and nanomechanical systems in the last decade. Since ferroelectrics exist in two polarized states with the possibility to be toggled by an external electric field, they became a key material for non-volatile storage media with high potential for mobile applications such as mobile phones and laptops [7].

In the quest for the technological limit of these Ferroelectric Random Access Memories (FeRAM), questions about data retention, fatigue and imprint but also about the minimum feature size have to be addressed. With respect to scaling, up to now most work has been devoted to the operating voltage (vertical dimension), whereas the lateral dimensions are crucial for high storage densities. In particular, the detectable displacement charges upon switching scale with the area of the memory cell.

In recent years tremendous progress in the fabrication of nano-sized ferroelectrics has been achieved, resulting in epitaxial films only a few unit cells thick and laterally confined sub-50 nm islands with reproducible quality [8–12]. In terms of metrology Piezoresponse Force

Microscopy (PFM) has become an indispensible tool to study size effects in nanoscale ferroelectrics due to its high lateral resolution.

Parallel to the advances in sample preparations the versatility of PFM has been continuously enhanced. Similar to other imaging measurement techniques, PFM suggests a very intuitive access to the acquired data. In this sense the present work addresses new critical aspects of the measurement technique with an emphasis on the tip-sample interaction in the presence of adsorbates.

1.2 Literature

In the mid 1990's several groups modified an Atomic Force Microscopy (AFM) introducing the tip as a mobile top electrode. At first Gruverman et al. [13, 14] and Hidaka et al. [15] used this method to measure Pb(Zr,Ti)O_3 (PZT) thin films. Later Eng et al. [16, 17] and Aplanalp et al. [18] employed a four-quadrant photo diode to monitor the in- and out-of-plane piezoresponse of potassium titanyl phosphate (KTP), $BaTiO_3$ and Triglycine Sulphate (TGS) single crystals. Roelofs et al. [19] measured the in-plane and out-of-plane response of thin films. Colla et al. [20] modified the setup by deposition of a thin Pt top electrode to observe fatigue in PZT thin films.

While these groups focused on using PFM to characterize ferroelectrics, other scientists studied the actual imaging process: Kalinin et al. [21, 22] set up a model for the tip-induced electroelastic fields inside the material to establish a complete continuum-mechanics description of the PFM contact and the imaging mechanism. Depending on the contact, strong (classical), contact limited and weak (field induced) indentation limits are distinguished. From these regimes contrast mechanism maps were set up that elucidate the effect of experimental conditions on the measurement.

Harnagea et al. [23] claim that for soft cantilevers the piezoresponse signal is governed by the elastic properties of the cantilever. Furthermore they emphasized the dependence of the measurement on the excitation frequency. In order for the cantilever to follow the piezoelectric expansion and contraction of the sample, the frequency of the excitation voltage must be below the mechanical resonance of the probe. However, the resonance of a specific cantilever in contact mode is significantly higher compared to the non-contact mode, typically above 100 kHz.

PFM measurements and three-dimensional numerical models of a domain wall have recently been published by Scrymgeour et al. [24]. At the antiparallel ferroelectric domain wall a drastic increase in the in-plane piezoresponse is reported.

The influence of the anisotropic dielectric tensor on the electric field induced by the AFM-

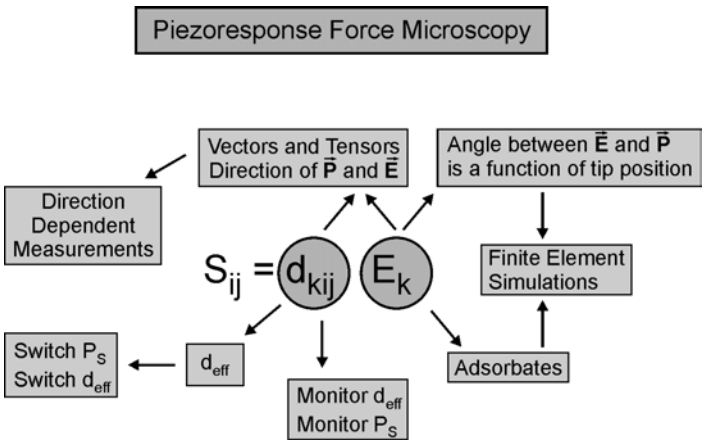

FIGURE 1.1: Overview of this work. The strain S_{ij} is a function of the piezoelectric tensor d_{kij} and the applied electric field E_k. The variety of possible interactions provides a wealth of information from PFM measurements.

tip bias was investigated by Otto et al. [25]. They numerically modeled the electric field in a tetragonal dielectric showing the radial field distribution underneath the tip. Harnagea et al. [26] showed that the effective piezoelectric tensor and thus the strain are a function of relative orientation of the electric field and the spontaneous polarization.

1.3 Objective

The main aim of this work is to identify and analyze extrinsic effects of PFM on ferroelectric nanostructures and to discriminate them against intrinsic contributions. Despite the successful application of PFM to ferroelectric thin films and nanoislands, many aspects of the method are still under discussion. This is why special attention is now devoted to the extrinsic contributions on the piezoresponse as a prerequisite to the identification of intrinsic properties.

The concept of this work is sketched in Fig. 1.1. The aim is to analyze and whenever possible to reduce the external influences on the measured piezoresponse. PFM detects a length variation of the sample in response to an external electric field. If this applied field E is known, the strain and thus the piezoelectric tensor d and the polarization orientation can be partially reconstructed i.e. ferroelectric domains can be imaged. Switching the polarization results in an inversion of the piezoelectric tensor, therefore the detection of a subsequent 180° phase shift between excitation and piezoresponse constitutes a sufficient criterion for ferroelectricity.

The polarization, the piezoelectric coefficients as well as the applied electric field are all direction dependent and described by vectors and tensors.

Harnagea's description of the piezoresponse assumes a globally homogeneous relative orientation of d and E while Otto emphasizes a strong local variation of E underneath the tip. The present work merges both ideas in a dedicated Finite Element Method (FEM) simulation that provides deeper insight into the tip-sample interaction for various PFM scenarios.

Furthermore for the first time a comprehensive direction analysis of the PFM setup is performed. The cantilever geometry imposes several constraints on the measurable quantities. Nonetheless it is this very geometry that optically enhances the detection sensitivity by more than one order of magnitude on the accessible slopes of nanoislands.

As one of the most substantial influences on quantitative PFM the occurrence and effects of adsorbates are analyzed by temperature-dependent X-ray Photoelectron Spectroscopy (XPS) in combination with variable temperature PFM. The experimental results are in excellent agreement with the aforementioned FEM simulations. This combined approach paves the way to access the intrinsic piezoresponse of ferroelectric nanograins.

2 Ferroelectrics

In this chapter the fundamentals of ferroelectrics for this work are reviewed. For a more comprehensive treatment of the subject the reader is referred to standard textbooks [27–30].

2.1 Fundamentals

Depending on their symmetry crystals can be classified into one of 32 crystal classes (point groups). Their dielectric behaviour is given by

$$D_i = \varepsilon_{ij} E_j$$

where D_i denotes the electrical displacement in direction i, E_j the electric field in direction j and ε_{ij} the dielectric constant[1].

Of the 21 non-centrosymmetric groups all except one (crystal class 432) allow for at least one non-vanishing component of the piezoelectric constants d_{ijk}. These are the 20 piezoelectric groups which permit a crystal to exhibit electric polarity when subject to a mechanical stress T and vice versa. The dielectric displacement is now given as[2]:

$$D_i = \varepsilon_{ij} E_j + d_{ik} T_k$$

From the piezoelectric groups 10 are characterized by the fact that they have a unique polar axis and they are termed pyroelectric. The magnitude of this polarization is temperature dependent. For small temperature changes ΔT, uniform over a polar crystal, the pyroelectric coefficients p_i add an additional contribution to the dielectric displacement [31]:

$$D_i = \varepsilon_{ij} E_j + d_{ik} T_k + p_i \Delta T.$$

If the polarization of the pyroelectric crystal has two stable states and this polarization can be switched from the one state to the other by application of an electric field, the crystal is

[1] Throughout this work the Einstein summation convention will be used. The convention states that repeated indices are implicitly summed over and the summation sign Σ is omitted. For example: $a_i = b_{ij} c_j$ instead of writing $a_i = \Sigma_j b_{ij} c_j = b_{i1} c_1 + b_{i2} c_2 + b_{i3} c_3$

[2] The piezoelectric constants d_{ijk} form a third-rank tensor. Due to the symmetry of $d_{ij,k}$ it is possible to use the Voigt notation according to the scheme,

tensor notation	11	22	33	23, 32	31,13	12,21
voigt notation	1	2	3	4	5	6

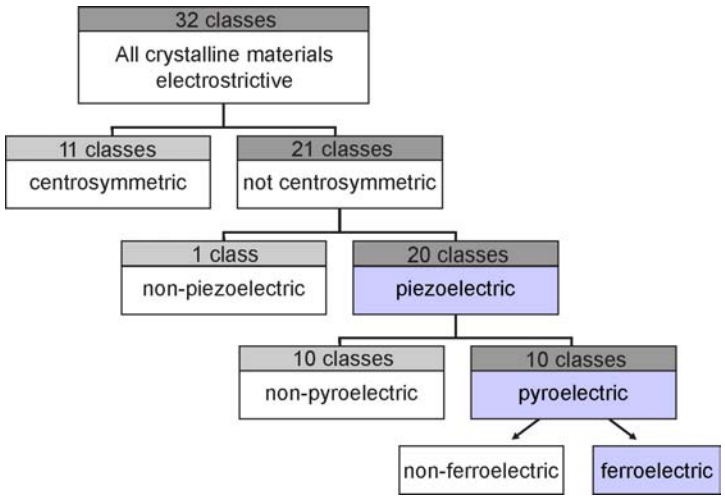

FIGURE 2.1: Classification of the 32 crystal classes. 20 classes exhibit piezoelectricity and among those 10 are pyroelectric. If the polarization of a pyroelectric material is reversible in an applied electric field, the material is denoted as ferroelectric (adapted from [32]). Ferroelectricity is not solely a structural property.

ferroelectric. The inherent spontaneous polarization P_{Si} directly influences the electrical displacement:

$$D_i = \varepsilon_{ij} E_j + d_{ik} T_k + p_i \Delta T + P_{Si}$$

In case of an isothermal setup, the pyroelectric effect does not contribute to the dielectric displacement. A graphical overview of the crystal classification is given in Fig. 2.1. Note that piezoelectricity is only a necessary and not an sufficient criterion for ferroelectricity.

The orientation of the spontaneous polarization is the dominant contribution to the dielectric Displacement in most ferroelectrics. Both the dielectric displacement D and the polarization P are expressed by a charge density measured in $\left[\frac{C}{m^2}\right]$.

The primary feature distinguishing ferroelectrics from the other pyroelectrics is that the spontaneous polarization can be reversed with an applied electric field. The polarization reversal can be demonstrated by the dielectric hysteresis. A typical loop is shown in Fig. 2.2. In a non-polarized crystal the polarization is randomly orientated, i.e. the overall polarization is zero. If we apply a very small electric field the relationship between P and E will behave like a normal dielectric, decreasing the field will again lead to a zero overall polarization. Increasing the electric field sufficiently will cause the polarization to be aligned in one direction. In this saturation

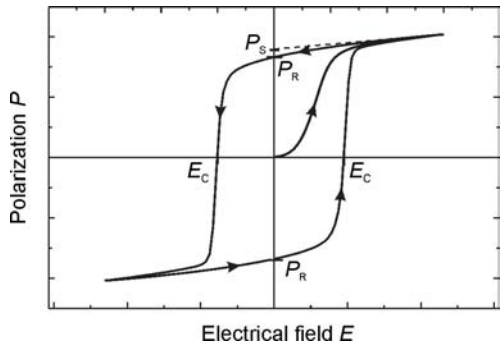

FIGURE 2.2: Schematic of a hysteresis loop. The characteristic points of the hysteresis are the remanent polarization P_R, the spontaneous polarization P_S and the coercive field E_C [27].

state the polarization is proportional to the applied electric field $[P_i = \chi_{ij} E_j = (\varepsilon_{ij} - 1) E_j]$. To switch the polarization into the negative state a so called coercive field E_C must be applied.

Lets have a look at the microscopic origin of the polarization. The materials used in this work are $BaTiO_3$ (BTO), $PbTiO_3$ (PTO), PZT and $KNbO_3$ (KNO), all having the general formula ABO_3 and a perovskite structure[3]. At different temperatures the materials undergo phase transitions (see section 2.5). In the cubic, centrosymmetric and unpolar phase the A^{x+} ions are on the corners of the cubed unit cell (Fig. 2.3*a*). The oxygen ions are arranged on the face centers forming an octahedron. The B^{y+} ion is in the center of the unit cell. In the ferroelectric phase (Fig. 2.3*b*) the unit cell is distorted and two different position exists for the B^{y+} ion: above or below the barycenter of the oxygen octahedron. The two polarization states are thermodynamic ground states where the center of the negative charges does not coincide with the center of the positive charges. When the polarization of the unit cell is switched by an external electric field, the B^{y+} ion moves into the other stable position.

The six directions (including the positive and negative orientations) along the three a_C-axes of the cubic cell are equivalent, and the spontaneous polarization may arise with equal probability along any of them when the crystal is cooled through the ferroelectric phase transition temperature. Electrical and mechanical boundary conditions imposed on the sample dictate the directions along which the polarization develops. The regions of the crystal with uniformly oriented spontaneous polarization are called ferroelectric domains. Two adjacent domains are separated by a domain wall. Domain walls separating regions with oppositely orientated polarization are called 180° walls and those which separate regions with mutually perpendicular polarization are called 90° walls [33]. Due to the tetragonal distortion the angle between the polar axes of 90° domains differs from 90° by an angle $\Delta\alpha = 2 \arctan(a/c)$ [32]. There are

[3]The natural representative of this structure is $CaTiO_3$, called perovskite.

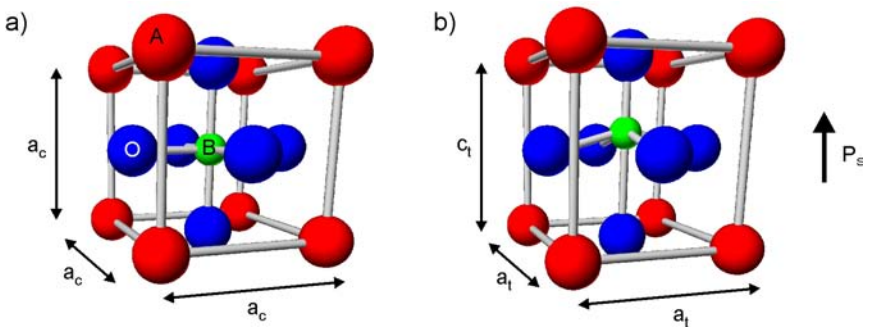

FIGURE 2.3: The unit cell of a material of ABO_3 type with perovskite structure in the cubic (a) and the tetragonal (b) phase. In the tetragonal phase the B ion can occupy two different sites (shown here in the upper position) [28, 32].

indications that charges accumulate at 90° domain walls in semiconducting ferroelectrics [34].

In the drive towards smaller capacitors, the direct measurement of the electric displacement is becoming more and more challenging as the influence of the parasitic capacitance of the contacting AFM increases. The smallest individual capacitors reported to have been measured have a size of 300 nm × 300 nm [35]. In parallel, even sub 100 nm capacitors have successfully been investigated [12].

Merz has shown in [36] that the following relationship holds true for BTO at temperatures between 90° and 120°:

$$P_S^2 \propto \frac{\Delta c}{c}$$

where $\Delta c/c$ is the lattice strain. However, as it is impossible to determine the lattice parameters of nanometer sized crystals (especially if grown on non–epitaxial substrates), this method is unsuited for determining the polarization of these grains.

Another way to obtain the spontaneous polarization is by measuring the piezoelectric coefficient according to the formula:

$$d_{33} = 2\varepsilon_{33} Q P_s$$

where Q is the electrostrictive coefficient. In the following I will present a short derivation of this formula [33].

The Gibbs free energy G is given by

$$G = U - TS - X_{ij}x_{ij} + E_i D_i$$

where U is the free energy, T the temperature, S the entropy, X_{ij} the strain, x_{ij} the stress, E the electric field and D the dielectric displacement. It follows for the derivative:

$$\frac{\partial^2 G}{\partial X \partial D} = \frac{\partial E}{\partial X}. \tag{2.1}$$

For small changes in the variables the elastic Gibbs free energy can be expanded in a Taylor series around the equilibrium state $G_{10}(T)$. In the simplest one-dimensional case where the polarization may occur only in one direction and when the fields are applied parallel to the polarization one obtains the following expression:

$$G = G_{10}(T) + \frac{1}{2}\alpha_1 D^2 + \frac{1}{4}\alpha_2 D^4 + \frac{1}{6}\alpha_3 D^6 + \frac{1}{2}sX^2 + QXD^2 + \cdots.$$

With $D = P_S$:

$$\frac{\partial^2 G}{\partial D \partial X} = 2QD = 2QP_S \tag{2.2}$$

The piezoelectric equations can be written in terms of the strain or voltage coefficient g. This coefficient is given by

$$g = \left(\frac{\partial E}{\partial X}\right). \tag{2.3}$$

Combining Eq. 2.1, Eq. 2.2, Eq. 2.3 and taking the assumptions into account results in

$$d_{33} = 2\varepsilon_{33} Q P_S. \tag{2.4}$$

The Landau-Ginsberg-Devonshire theory predicts a quantitative behavior for the size dependence of P and ε [37, 38]. Equation 2.4 provides a quantitative handle on d_{33} and Q as a function of size. If ε can be determined independently, then $d_{33} \propto P_S$ in the case of measuring the first harmonic.

2.2 Piezoelectric Effect

Piezoelectric materials can be polarized by an electric field and by the application of a mechanical stress . The linear relationship between stress T_{jk} applied to a piezoelectric material and the resulting surface charge density D_i,known as the direct piezoelectric effect, is given by

$$D_i = d_{ijk} T_{jk}$$

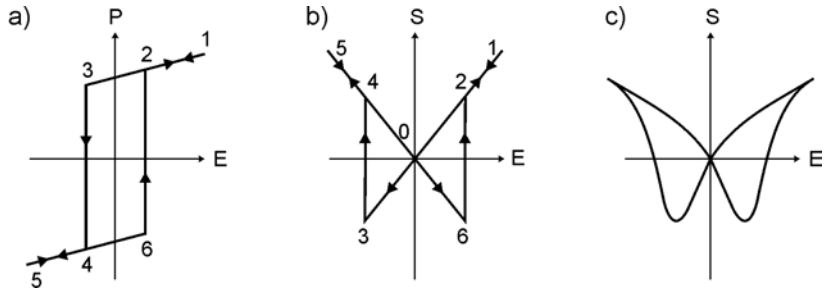

FIGURE 2.4: Schematic description of the converse piezoelectric effect: a) Hysteresis loop, b) ideal quadratic hysteresis loop of strain vs. field and c) real "butterfly" loop [28].

where d_{ijk} [C N^{-1}] is a third-rank tensor of piezoelectric coefficients.

Additionally, piezoelectric materials contract or expand when an electric field E is applied. The converse piezoelectric effect describes the strain that is developed in a piezoelectric material due to the applied electric field:

$$\eta_{ij} = S_{ij} = d_{kij}E_k = d^t_{ijk}E_k \tag{2.5}$$

where ^{t} denotes the transposed tensor. The units of the converse piezoelectric coefficient are [m V^{-1}]. The piezoelectric coefficients d for the direct and converse piezoelectric effects are identical and can be either positive or negative. It is common to call a piezoelectric coefficient measured in the direction of applied field the longitudinal coefficient, and that measured in the direction perpendicular to the field the transverse coefficient. Other piezoelectric coefficients are known as shear coefficients [33].

In addition to the polarization-electric field hysteresis loop, polarization switching by an electric field in ferroelectric materials leads to a strain-electric field hysteresis, as shown in Fig. 2.4. The strain-electric field hysteresis loop resembles the shape of a butterfly and is due to three types of effects: the normal converse piezoelectric effect, the switching and the movement of domain walls. The following description illustrates how the strain of the crystal changes during field cycling [33, 39].

A monodomain single crystal is assumed as well as a polarization which can be instantaneously switched by 180°. At zero field (point 0 in Fig. 2.4) the strain of the crystal is taken to be zero. The electric field is then applied in the direction of the spontaneous polarization. As the field is increased, the crystal expands through the piezoelectric effect, according to equation 2.5 and the strain follows the line 0→1. The expansion continues up to point 1. Here the field is decreased, but is still parallel to P_S. The strain of the sample follows the same line but in the opposite direction (1→0), being again zero at point 0. The field direction is then changed,

resulting in an electric field antiparallel to P_S. As the field strength increases in the negative direction, the crystal contracts with respect to point 0, again according to equation 2.5. At point 3 the field is large enough to switch the direction of polarization. Thereafter, the polarization is parallel to the field, and the strain becomes positive again (point 4). During further increase of the field in negative direction, the strain increases up to point 5, and then decreases back to point 0 as the field is decreased. The reversal of the polarization and sudden change of the strain occurs again at point 6. The strain-field curve is linear, indicating that the strain is purely piezoelectric except at the switching points 3 and 6.

In reality, the strain-field relationship is more complicated, as shown in Fig. 2.4c. Ceramic samples usually contain a number of non-180° domains. The movement and switching of non-180° walls may involve a significant change in dimensions of the sample, in addition to the pure piezoelectric response of the material within each domain. The switching of the a and c axes of the tetragonal unit cell is accompanied by a strain of approximately 1% in BTO and 6% in PTO at room temperature. Such large strains are not achieved in ferroelectric ceramics because only some parts of the sample contain non-180 walls, their orientation may be unfavourable and some of these domains will never switch under realizable experimental conditions.

2.3 Electrostrictive Effect

The electrostrictive effect is an example of nonlinear coupling between elastic and electrical fields. If an electric field E is applied on a material, the electrostrictive strain S is defined by

$$S_{ij} = \underbrace{d_{kij}E_k}_{\substack{\text{Piezoelectric} \\ \text{effect}}} + \underbrace{M_{ijkl}E_kE_l}_{\text{Electrostriction}}$$

where M_{ijkl} are components of the fourth-rank tensor and called electrostrictive coefficients. The electrostrictive effect is present in all materials, irrespective of the crystal symmetry.

In PFM the electric field which is applied to measure the converse piezoelectric or electrostrictive effect is sinusoidal. The relationships

$$E_k = E_l = E_0\cos(\omega t) \quad \Rightarrow \quad E_kE_l = E_0^2\frac{1}{2}\left(1+\cos(2\omega t)\right)$$

show that the response occurs at the second harmonic of the excitation field [40].

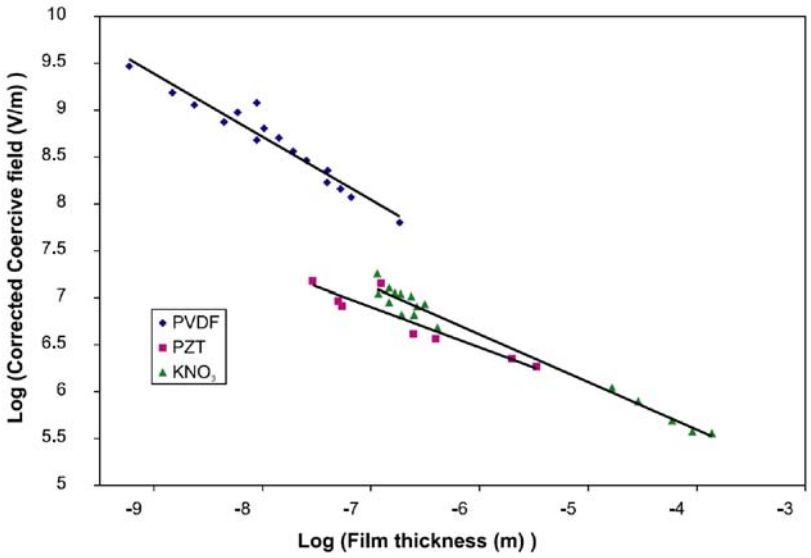

FIGURE 2.5: The log(coercive field) versus log(thickness) for different ferroelectric films [41].

2.4 Kay-Dunn Law

The hysteresis loops of good single crystals of BTO exhibit rather sharp corners and a marked rectangular appearance. The value of the coercive field, measured at room temperature, varies from a minimum of 500 V/cm to a maximum of about 2000 V/cm. When measuring the piezoresponse the applied electric field should be small, so as to be in the linear part of the "butterfly" loop and clearly below the coercive field.

In PFM (see section 5.2) an electric field is applied to the sample by an AFM tip. Typical values are in the range of 1 V being applied to samples only 10 nm thick in some cases [42,43]. Assuming a plate capacitor setup, this leads to an applied field above 10^5 V/cm which in in line with the values obtained by Otto et al. [25] for a simulated non-ideal contact of the AFM-tip on a BTO crystal. This is one order of magnitude larger than the theoretical value and three orders of magnitude larger than the experimental values of the coercive field E_c of common bulk ferroelectric materials.

Back in 1962 H. Kay and J. Dunn described the dependence of the coercive field E_c by a semi-empirical law [44]. They found that on Triglycine Suplphate crystals between 0.15 mm and 4.00 mm thick the coercive field shows a variation with the crystal thickness d according to

$$E_c(d) \propto d^{-2/3}. \tag{2.6}$$

M. Dawber et al. have shown [45] that the law holds true for different materials (PVDF, PZT, KNO_3) for films ranging from 100 μm down to 1 nm (see Fig. 2.5). For a 50 nm thick film a corrected coercive field of around 10^5 V/m has been found for PZT and KNO_3, both materials also used in this work. The extrapolated value for a 10 nm thick film is around 3×10^5 V/cm.

Another aspect which has to be considered in PFM are adsorbates on the surface which act as a voltage divider. It will be shown in section 7.1 that nearly up to one order of magnitude of the applied potential drops over the physisorbates (another part drops over the chemisorbates). In most PFM experiments, ferroelectric switching is induced for a DC voltage >3 V applied to the tip. This indicates that with an applied AC voltage of 1 V the electric field is below the coercive field of the material under investigation.

2.5 Properties

In this section the data of the relevant materials will be presented. Unless specified otherwise, all data are for room temperature and cited from [46].

2.5.1 Barium Titanate

BTO is one of the most extensively investigated ferroelectric and a model system for this class of materials. It is interesting as it is mechanically and chemically stable and exhibits ferroelectric properties at and above room temperature.
The material exhibits four phase transitions:

at -90°C:	rhombohedral → orthorombic
at 5°C:	orthorhombic → tetragonal
at 130°C:	tetragonal → cubic
at 1460°C:	cubic → hexagonal.

At room temperature i.e. in the ferroelectrically active phase, the unit cell parameters are a = 0.39920 nm and c = 0.40361 nm, resulting in a tetragonality of 1.1%. These parameters have to be taken into account when depositing BTO in order to select an appropriate substrate to minimize the strain (see section 6.4).

The dielectric constants are ε_{33} = 1500 and ε_{11} = 75.

The values for the piezoelectric coefficients are d_{33} = 85.6 pm/V, d_{31} = -34.5 pm/V and d_{15} = 392 pm/V.

2.5.2 Potassium Niobate

KNO exhibits three phase transitions:

at -10°C:	rhombohedral → orthorombic
at 225°C:	orthorhombic → tetragonal
at 418°C:	tetragonal → cubic.

In the orthorhombic phase, the unit cell parameters are a = 0.3973 nm, b = 0.5695 nm and c = 0.5721 nm. The dielectric constants measured at constant strain at are ε_{11} = 37, ε_{22} = 780 and ε_{33} = 24.

The values of the piezoelectric coefficients are d_{31} = 9.9 pm/V, d_{32} = 19.2 pm/V, d_{33} = 30.5 pm/V, d_{15} = 103.0 pm/V and d_{24} = 78.0 pm/V.

2.5.3 Lead Titanate

At 450°C PTO has a phase transition from a tetragonal to a cubic crystal system. Another phase transition was reported to occur at about -100°C or -160°C.

At room temperature (tetragonal phase) the unit cell parameters are a = 0.3904 nm and c = 0.4152 nm, resulting in a tetragonality of 6.0%.

For single crystals, the piezoelectric coefficients are d_{33} = 11.7 pm/V, d_{31} = -2.5 pm/V and d_{15} = 6.5pm/V.

2.5.4 Lead Zirconate Titanate

The Curie temperature of PTO is among the highest for perovskite-type ferroelectrics [28]. Almost any substitution of Pb or Ti with suitable atoms which are likely to form a perovskite-type lattice causes a lowering of the Curie point. Due to its high piezoelectric coupling factors, Ti is often substituted by Zr. Depending on the ratio of $PbTiO_3$ to $PbZrO_3$ the critical temperature, the lattice parameters, the crystal structure and the electrical properties of $PbZr_xTi_{1-x}O_3$ can be modified.

A morphotropic phase boundary divides the ferroelectric phase into a Ti-rich tetragonal phase region and a Zr-rich rhombohedral phase region. At room temperature the morphotropic phase boundary is at a Zr-content of 53%. The lattice parameters of the solid $PbZr_xTi_{1-x}O_3$ solution exhibit an abrupt change near the morphotropic phase boundary, where the dielectric constant, the piezoelectric constants and the piezoelectric coupling factors show anomalously high values. Therefore this composition is especially suited for piezoelectric applications [32].

3 Finite Element Simulations

Finite Element Simulations are the most powerful technique to calculate the integral behavior of a continuous system. These systems are usually described by field distributions like temperature, mechanical stress or electric potential and are modeled with three sets of equations:

- single or partial differential equations for independent field vectors
- equations for the boundary conditions
- material laws correlating the independent and dependent system variables.

The number of $degree\text{-}of\text{-}freedom$ variables indicates how many variables can be independently changed without violating any boundary conditions. For each degree of freedom a differential equation has to be set up and solved.

In order to solve the differential equations, the continuous system is discretized into a mesh of elements. Each element is defined by at least 2 nodes. The differential equations are solved at every node and the field values between the nodes are calculated by a polynomial interpolation function. An example of a meshed system is given in Fig. 3.1.

Three major steps are required for a finite element analysis:

- Preprocessing: definition of the problem and the material, modeling of the device
- Solution: assigning loads and constrains, solving the set of equations
- Postprocessing: viewing and further processing of the resulting data and comparison with experiments

Further details on FEM simulations can be found e.g. in [48, 49].

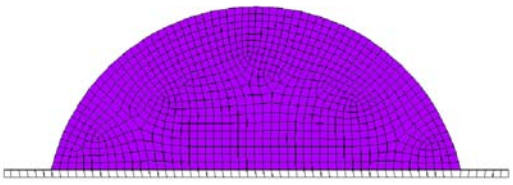

FIGURE 3.1: Model of a piezoelectric nanograin on an electrode meshed by a FEM program. The differential equations are solved at every node. This configuration has been used for publication [47] and the simulations given in section 7.4. Note that the mesh has neither mirror, nor radial or any other symmetry. This causes the numerical errors in Fig. 7.28.

3.1 Linear Piezoelectric Equations

The relationship between the mechanical stress T_{ij} [Nm^{-2}] applied to an elastic material and the resulting strain S_{ij} can be linearly approximated by Hooke's law:

$$S_{ij} = s_{ijkl} T_{kl} \tag{3.1}$$

where the elastic compliance s_{ijkl} [m^{2}N^{-1}] is a fourth-rank tensor and S_{ij} and T_{ij} are second-rank tensors.

The inverse relationship

$$T_{ij} = c_{ijkl} S_{kl} \tag{3.2}$$

defines the elastic stiffness tensor c_{ijkl} [Nm^{-2}]. The relationship between the elastic compliance and the stiffness tensor is given by $s_{ijkl} c_{klmn} = c_{ijkl} s_{klmm}$ [33].

The strain and stress are by definition symmetrical second-rank tensors, i.e. $S_{ij} = S_{ji}$ and $T_{ij} = T_{ji}$. The symmetry of the strain and stress tensors requires that $s_{ijkl} = s_{jilk}$ so that the number of independent elements of the compliance and stiffness tensors is reduced from 81 to 36. Using thermodynamics it can be further shown that s_{ijkl} is a symmetrical tensor, i.e. $s_{ijkl} = s_{klij}$ and the number of independent elements is therefore reduced to 21. Further reduction of independent components is possible using material symmetry according to the *von Neumann* principle. For the piezoelectric materials used in this work the compliance matrix s is given by [50]

$$\begin{pmatrix} s_{11} & s_{12} & s_{13} & 0 & 0 & 0 \\ s_{21} & s_{22} & s_{23} & 0 & 0 & 0 \\ s_{31} & s_{32} & s_{33} & 0 & 0 & 0 \\ 0 & 0 & 0 & s_{55} & 0 & 0 \\ 0 & 0 & 0 & 0 & s_{55} & 0 \\ 0 & 0 & 0 & 0 & 0 & s_{66} \end{pmatrix}$$

with $s_{66} = 2\,(s_{11} - s_{12})$. For isotropic materials this matrix can be reduced down to Young's modulus E and the poisson ratio ν:

$$E = \frac{1}{s_{11}} = \frac{1}{s_{22}} = \frac{1}{s_{33}}$$
$$\nu_{12} = -\frac{s_{12}}{s_{13}}$$
$$\nu_{13} = -\frac{s_{13}}{s_{33}}$$

The expansion of Hooke's law for piezoelectric materials in the presence of an electric field leads to the piezoelectric equations in Voigt notation with linear small signal material characteristics

$$S_i = s_{ij}^E T_j + d_{ik}^t E_k$$
$$D_m = d_{mj} T_j + \varepsilon_{mk}^T E_k$$

with the compliance matrix s at a constant electric field E, the piezoelectric coefficients d_{ik}, the direction dependent permittivity ε at constant mechanical stress T, applied electric field E and dielectric Displacement D. The superscript ^{t} denotes a transposed tensor.

An equivalent equation system is used in the Finite Element Program ANSYS [51–53]:

$$T_i = c_{ij}^E S_j + e_{ik}^t E_k$$
$$D_m = d_{mj} T_j + \varepsilon_{mk}^T E_k$$

with the stiffness matrix c_{ij}^E at a constant electric field E and the piezoelectric coefficient matrix e_{ik}.

3.1.1 Relations between the mechanical coefficients

The correlations between the elastic compliance s [m^2/N] and the stiffness coefficients c [N/m^2=Pa] are:

$$c_{11} = \frac{s_{11} s_{33} - s_{13}^2}{f(s)}$$
$$c_{12} = \frac{s_{12} s_{33} - s_{13}^2}{f(s)}$$
$$c_{13} = \frac{s_{13} \left(s_{11} - s_{12}\right)}{f(s)}$$
$$c_{33} = \frac{s_{11}^2 - s_{12}^2}{f(s)}$$
$$c_{44} = \frac{1}{s_{44}}$$
$$f(s) = \left(s_{11} - s_{12}\right) \left[s_{33} \left(s_{11} + s_{12}\right) - s_{13}^2\right]$$

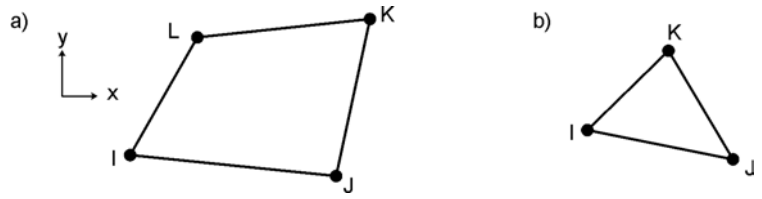

FIGURE 3.2: Geometry of the element (Plane13) used for the simulation with ANSYS. Two different options can be implemented; either with 4 nodes (a) or the triangle with 3 nodes (b). The triangle being to stiff is not recommended for structural applications.

3.1.2 Relations between piezoelectric coefficients

The d_{ij} coefficients [m/V = C/N] describe the mechanical strain produced by an electrical field, whereas the e_{ij} coefficients [C/m^2=N/Vm] correlate the mechanical strain with the applied charge density [50]. Their relationship is given by the following equations:

$$
\begin{aligned}
e_{31} &= d_{31}\left(c_{11}^E + c_{12}^E\right) + d_{33}c_{13}^E \\
e_{33} &= 2d_{31}c_{13}^E + d_{33}c_{33}^E \\
e_{15} &= d_{15}c_{44}^E \\
d_{31} &= e_{31}\left(s_{11}^E + s_{12}^E\right) + e_{33}s_{13}^E \\
d_{33} &= 2e_{31}s_{13}^E + e_{33}s_{33}^E \\
d_{15} &= e_{15}s_{44}^E
\end{aligned}
$$

3.2 Implementation

For the simulations in this work, I use the commercial finite-element program ANSYS version 8.1. The piezoelectric thin films or the nanograins are modeled in a 2-D cross section. The system is meshed with the element Plane13, which has 2-D magnetic, thermal, electrical, piezoelectric and structural field capability with limited coupling between the fields [54]. Only linear material characteristics can be used for the dielectric and electromechanic coupling coefficients. Static, modal, harmonic, and transient analyses can be performed [55].

The element Plane13 can be used in two different ways: either as a quadrilateral with 4 nodes or as a triangle with 3 nodes. For structural analyses the 4-node option is a better description of the system and will in most cases yield an accurate solution in a reasonable amount of computing time. Assume a triangle-shaped element with a force acting in direction -y onto it (Fig. 3.2): this option offers more structural stability than a 4-node quadrilateral. Therefore the triangle form is inappropriate for the investigation of piezoelectric deformations.

Therefore it is important to avoid this triangle form. For a curved shell, the elements must be small enough to model the bent surface adequately. Fig.3.1 shows a meshed system where nearly exclusively quadrilaterals have been used in dividing a round system.

As the investigated nanograins often show an axial symmetry, the simulation has been reduced to only a cross section of it to minimize the calculation time (e.g. Fig. 7.28).

In all simulations in this work the following material tensors (numerical values from [46]) are specified:

- Dielectric constant (relative permittivity)
- Elastic moduli (Young's moduli)
- Poisson's ratio
- Density of the material
- Piezoelectric coefficient matrix e

4 X-Ray Photoelectron Spectroscopy

4.1 XPS Principle

In XPS a photon of energy $h\nu$ penetrates the surface under investigation and is absorbed by an electron with a binding energy E_{BE} below the vacuum level, which then emerges from the solid with a kinetic energy $(h\nu - E_{BE})$. Taking the known energy offset between the surface and the spectrometer into account leads to the following equation:

$$E_{kin} = h\nu - E_{BE} - \Delta\phi$$

Figure 4.1 depicts an example of a 2p photoelectron emitted from copper after the absorption of an X-ray photon. An illustration of the setup is given in 4.2. Any photon whose energy

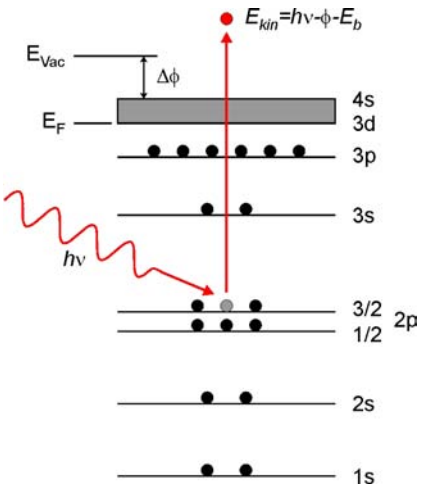

FIGURE 4.1: A 2p photoelectron is emitted from copper after the excitation of the atom by absorption of an X-ray photon (Adapted from [56]).

exceeds the work function of the solid $(h\nu > \Delta\phi)$ can be used for photoelectron spectroscopy, which excludes the near ultraviolet, visible and higher wavelength radiation. In practice the spectroscopy is nearly exclusively performed in two relative narrow energy ranges. The first one (also known as Ultraviolet Photoelectron Spectroscopy) is provided from gas discharge (e.g. He with two main lines of a photon energy of 21.2 eV and 40.8 eV) which is not capable of accessing a significant number of core levels. The second readily available photon energy range is the Al and Mg k_α X-ray emissions at 1486.6 eV and 1253.6 eV respectively [57].

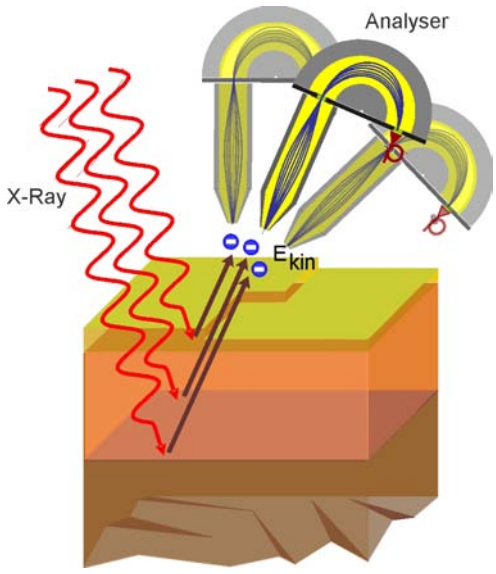

FIGURE 4.2: Principle of X-Ray Photoelectron Spectroscopy.

The background signal in the photoelectron spectrum arises from the multiply scattered secondary electrons which are generated in the deeper layers of the sample. If these secondaries are inelastically scattered before they can escape from the surface, then they will contribute to the background rather than to the characteristic peaks. It follows that the observed peaks in the spectrum are due to photoelectrons which are generated in the surface layers only, at a depth which is less than the mean free path of the secondaries in the material [56]. The maximum depth resolution is in the range of 4 nm to 6 nm.

The electron binding energies of interest may exceed 1 keV. The relationship between the X-ray energy and its wavelength is $\lambda = hc/E = 1.24/\text{V m}$, where c is the speed of light, E the energy of the quantum and V is in keV, so the suitable excitation wavelength is in the order of 0.1 nm to 1 nm, i.e. X-rays.

4.2 Contamination

If we are to study the properties of a surface it is mandatory that the composition of the surface must remain essentially constant over the duration of the experiment. This implies that the rate of arrival of reactive species from the surrounding gas phase should be low. The following expression for the rate of arrival for atoms or molecules can be determined from the kinetic

Incident and adsorbing species	No. of molecules arriving (cm^{-2})	Coverage with unity sticking factor (monolayers)
H_2 adsorbing as H	1.43×10^{15}	1.80
O_2 adsorbing as O	3.58×10^{14}	0.44
CO adsorbing as CO	3.83×10^{14}	0.24

TABLE 4.1: Effect of 1 Langmuir exposure of different adsorbates at 300 K [56]

theory of gases [57]:

$$r = 3.51 \times 10^{22} \frac{P}{\sqrt{TM}} \tag{4.1}$$

with the pressure P expressed in torr (1 torr = 1.332 mbar), T in K and M is the molecular weight; this leads to r being given in $cm^{-2}s^{-1}$. For example, N_2 molecules (M = 28) at T = 293 K at 1 torr have an arrival rate of 3.88×10^{20} molecules $cm^{-2}s^{-1}$. It is convenient to define a monolayer adsorption time in terms of the pressure. In defining this, we assume that a monolayer, i.e. a single complete atomic layer, consists of about 10^{15} atoms/cm^2 and that all molecules arriving at the surface stick and are incorporated into this monolayer. For the given example the monolayer time is about 3×10^{-6} s at 1 torr or almost 1 hour at 10^{-9} torr. If all gas atoms or molecules arriving at a surface in a vacuum system do indeed stick to it, then contamination of a few percent of a monolayer in an experimental time of 1 hour requires pressures of 10^{-10} torr or better. Although these are worst case assumptions, some surfaces do react easily with H and CO, the main molecules in an Ultra High Vacuum (UHV) chamber.

Equation 4.1 forms the basis for the definition for a unit of exposure. The unit which is firmly established is the Langmuir L, with 1 L = 10^{-6} torr s exposure. A major disadvantage is that the actual number of atoms or molecules arriving at a surface in 1 L of exposure depends on their molecular weight and the gas temperature. Table 4.1 illustrates this effect, showing the number of molecules striking 1 cm^2 of surface in 1 L with a gas temperature of 300 K. The last column shows the coverage which would result if all the molecules were to stick on the surface.

The purpose of UHV is therefore to keep a surface in its clean or otherwise well-characterized condition once produced. While this guarantees that a surface should not be influenced by the arrival of ambient atoms and molecules on a time scale of the order or one hour or more, a further requirement to study the properties of the ideal surface is to be able to clean them. The main methods used to achieve this $in\ situ$ cleaning are

- cleavage

- heating
- ion bombardment (typically Ar ions)
- chemical processing.

4.3 Adsorbates

In chapter 7 of this work I frequently distinguish between chemisorbates and physisorbates. The distinction between these two types of adsorption lies in the form of the electronic bond between the adsorbate and the substrate. If an adsorbed molecule forms a covalent or ionic chemical bond with the surface it is said to be chemisorbed. If, on the other hand, it is held to the surface only by van der Waals' forces, relying on the polarisability of the otherwise undisturbed molecule, it is said to be physisorbed [56]. Physisorption produces weak bonds while chemisorption often produces strong bonds. It is usual to regard the upper limit of the bond strength in physisorption as around 0.6 eV per atom or molecule. However, the distinction is strictly in terms of the form of the bond, and not its energy, and there are cases in the literature in which electronic modifications characteristic of chemisorption are seen in far more weakly bound species.

5 Scanning Probe Microscopy

5.1 Scanning Force Microscopy

The principle of Scanning Probe Microscopy (SPM) is quite elegant: a sharp tip scanns over a sample. This is achieved by moving the tip line by line and recording the spatial variation of the interaction. Depending on the sample and the probe, various interactions between the two can be measured, e.g. electrical, magnetic, mechanical.

The focus of this work is on AFM. First, the fundamental hardware operations are introduced, especially those related to the contact mode. Secondly, both general and new aspects of the contact mode and certain effects related thereto will be presented. In the third part PFM, an extension of contact mode AFM, will be discussed.

5.1.1 Atomic Force Microscopy

During the night of March 16th 1981 the first log I-s characteristics between a tip and a sample were obtained by Binnig, Rohrer, Gerber and Weibel at the IBM Rüschlikon laboratory [58]. The real breakthrough for the Scanning Tunneling Microscopy (STM) however came with the first atomic resolution image of the Si(111) 7×7 surface obtained in autumn 1982 [59] and shown in Fig. 5.1. This first atomic resolution made the STM different and superior compared to other microscopes and lead to Binnig and Rohrer being awarded the Nobel Prize of Physics 1986 for their invention.

Although unsurpassed for its vertical and lateral resolution, the STM has one serious constraint: the sample must be conducting or at least semi-conducting. This limitation was overcome by Binning et al. [59] by mouting a tip as a probe onto a cantilever. The force interaction between the sample and the tip approaching each other causes the cantilever to bend according to Hooke's law. These deflections can be monitored in different ways, e.g. piezoelectric sensors, changes in capacitance or optically.

A generalized set-up of an AFM is given in Fig. 5.2. The sample is moved, scanned and brought into contact to the cantilever by three piezo-elements. Rough positioning and approaching is realized by the macroscopic adjustment. In certain cases it might be desirable to cool or heat the sample; this requires a cooling system and a heater respectively. The construction of the heating and cooling system must take an expansion and contraction of the setup due to the temperature change into account. To detect the movement of the cantilever, a laser is focused onto the cantilever and the reflected beam is adjusted to illuminate the two sectors of the diode equally. For simplicity, a two sector diode, capable of monitoring only a vertical deflection, is

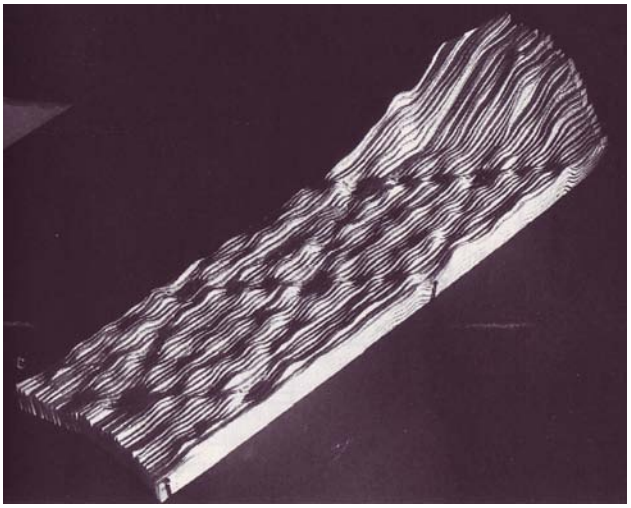

FIGURE 5.1: First STM topograph of the 7×7 reconstruction of the Si(111) surface, showing two complete rhombohedral unit cells [59].)

illustrated. If the cantilever bends upwards during scanning, a larger part of the upper sector than the lower sector of the diode is illuminated. This normalized difference is electronically compared to the given set-point and used by the PID-Controller to readjust the height of the sample. The high voltage amplifier driving the z-piezo is fed by the output of the PID-loop. The actual scanning is usually computer-controlled. As the microscope is extremely sensitive to external mechanical distortions, it has to be mounted on an anti-vibration system. Further details on the construction of the SPM can be found in [60–67]. An excellent review on the basic operation principles of scanning tunneling microscopy and spectroscopy can be found in [68].

5.1.2 Optical Lever Arm Method

Nowadays the deflection of the cantilever is typically detected by measuring the reflected laser beam on a two or four sector diode [69, 70]. This optical lever arm method is depicted in Fig. 5.3.

The cantilever can be regarded as a beam which is clamped on one side and acted upon by a force on the other side . The deformation angle Θ at the unclamped side (Fig. 5.3) for a given vertical displacement is [71]

$$\Theta = \frac{3\Delta z}{2L} \tag{5.1}$$

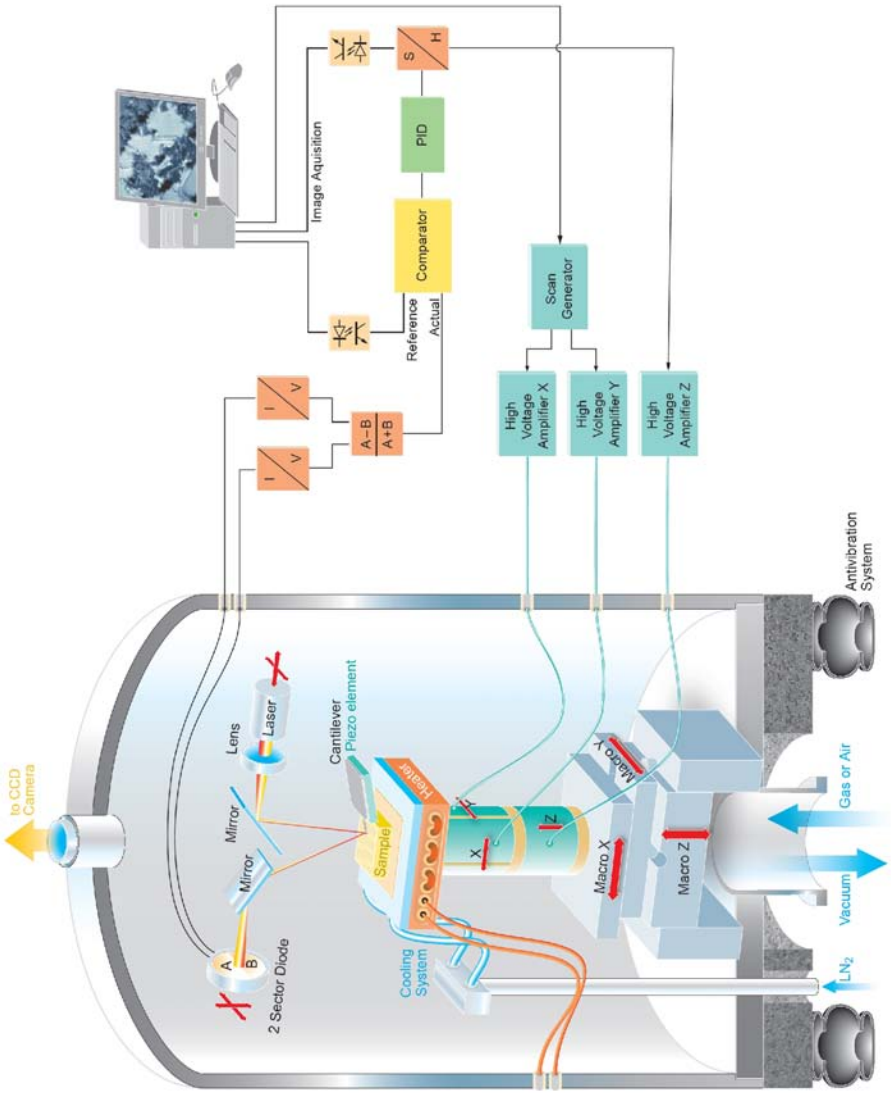

FIGURE 5.2: Setup of an AFM consisting of a damped vacuum chamber, macro-positioners, x, y and z piezo-scanners, a variable temperature system, sample, cantilever and the optical system. The signal of the photo diode is electronically compared with a reference value and used to regulate the z-position (image courtesy of T. Pössinger).

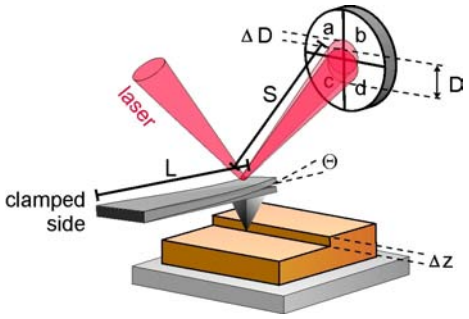

FIGURE 5.3: Scanning Force Microscope utilizing the optical lever arm method. A laser beam is reflected by the cantilever and the cantilever deflection is detected by the quadrupole diode (adapted from [32]).

where L is the length of the cantilever and Δz the vertical movement of the tip, e.g. the step height.

Initially, all four sectors of the photo diode have the same irradiation:

$$\jmath_{tot} = \sum_{i=1}^{4} \jmath_i = 4\jmath_i$$

where $\jmath_{tot}$ is the total laser intensity. For small deflections the change of the irradiated area in the quadrants is a linear function of the tip displacement Δz. For a vertical displacement the two top quadrants (a and b) and the two bottom quadrants (c and d) have to be regarded as one and this results in

$$\jmath_a = \jmath_b = \frac{\jmath_{tot}}{4} \cdot \frac{D + \Delta D}{2}$$
$$\jmath_c = \jmath_d = \frac{\jmath_{tot}}{4} \cdot \frac{D - \Delta D}{2}$$

where D is the diameter of the laser spot on the diode. From simple geometric considerations [72] and by including Eq. 5.1 the movement ΔD of the laser spot is given by

$$\Delta D = \sin(2\Theta) \cdot S \approx 2\Theta \cdot S = \frac{3\Delta z S}{L} \tag{5.2}$$

where S is the distance from the cantilever to the photo diode. Inserting Eq. 5.1 into Eq. 5.2 leads to a difference of the top quadrants minus the bottom quadrants of

$$(\jmath_a + \jmath_b) - (\jmath_c + \jmath_d) = \jmath_{tot} \cdot \frac{3\Delta z S}{DL}$$

which is a function of the displacement Δz as well as the total laser intensity $\jmath$. This would make a variation of the laser indistinguishable to a change of the cantilever position and can be overcome by using the normalized difference

$$\frac{(\jmath_a + \jmath_b) - (\jmath_c + \jmath_d)}{\jmath_{tot}} = \frac{3\Delta z S}{DL}$$

which is independent from the laser intensity. The difference only depends on the dimensions S, L and D. The vertical "optical amplification" (from Eq. 5.2)

$$\frac{\Delta D}{\Delta z} = \frac{3S}{L}$$

is typically a factor of 1000 [73].

Similar to the presented vertical deflection the lateral torsion can be evaluated by measuring the normalized difference of the left and right parts of the photo diode, i.e.

$$\frac{(\jmath_a + \jmath_c) - (\jmath_b + \jmath_d)}{\jmath_{tot}}.$$

In chapter 7.2 I will show that the lateral optical amplification is −for commercially available cantilevers− substantially higher than for the vertical case.

5.1.3 Cantilever Properties

The cantilever is a crucial component in any AFM [59]. To achieve a high sensitivity, a large deflection for a given force is desired. On the other hand, a high resonant frequency is necessary in order to minimize sensitivity to mechanical vibrations while scanning. The resonance frequency of the spring system is given by

$$\omega_0 = \sqrt{\frac{k}{m}}$$

where k is the spring constant and m the mass loading of the spring. As a result the mass m and therefore the geometrical dimensions of the sensor must be as small as possible. Microfabrication techniques are used to produce cantilevers with a length of 50 μm - 500 μm, a width of 20 μm - 50 μm and a thickness of 1 μm - 2 μm.

However, unlike a simple one-dimensional spring, the stiffness of the cantilever is direction dependent. For a given direction, the stiffness can be expressed as a small set of elastic constants.The largest errors in determining the constants arise from uncertainties from Young's

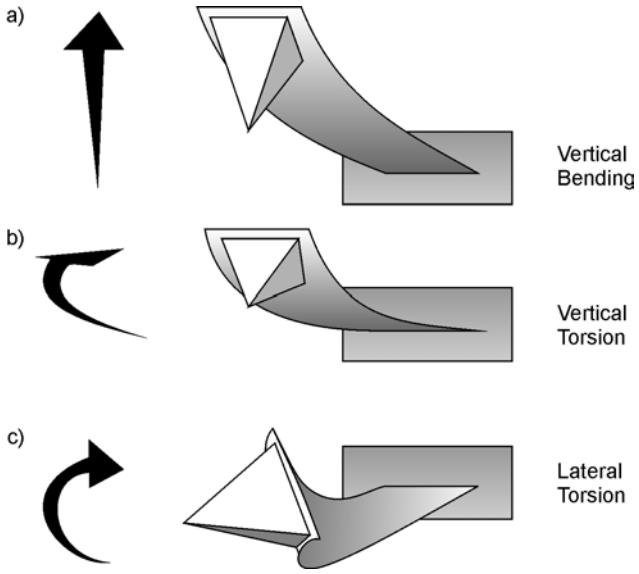

FIGURE 5.4: Three basic deformation types for a bar shaped cantilever. a: vertical bending, in which the beam length is a moment arm. b: vertical torsion is caused by a force parallel to the cantilever beam using the tip height as lever. c: lateral torsion caused by a tip moment perpendicular to the cantilever beam (adapted from [74]).

modulus, Poisson's constant and the actual thickness of the cantilever [74]. Experimental methods have been derived to determine these values [75, 76]. These experimental values for the beam stiffness can be used to predict other −e.g. torsional− elastic constants, which are much harder to determine experimentally.

For a bar-shaped cantilever, three basic deformation modes exist, namely vertical bending, pure vertical torsion and pure lateral torsion (Fig. 5.4). By the principle of superposition, any arbitrary deformation can be split up into these separate deformation modes. The cantilever is thought to be subject to a force N perpendicular to the cantilever, a vertical bending moment M and a lateral bending moment T, all acting at the tip end. The dependence of the back end angles α and Θ (see also Fig. 5.3) and the vertical deflection Δz on the loading forces and moments are:

$$\begin{bmatrix} \alpha \\ \Theta \\ \Delta z \end{bmatrix} = \begin{bmatrix} C_\alpha & 0 & 0 \\ 0 & C_\Theta & C_{\Theta z} \\ 0 & C_{\Theta z} & C_z \end{bmatrix} \begin{bmatrix} T \\ M \\ N \end{bmatrix} \tag{5.3}$$

with L the cantilever length and $C_{z\Theta} = C_{\Theta z}$. In Table 5.1 the compliances associated with the three deformation modes are presented. To determine these compliances the mechanical

Force Direction	Compliance	Back Angle	Elastic Curve
Load Force N	$C_z = \frac{4L^3}{Ewt^3}$	$\Theta_{\max} = \frac{6NL^2}{Ewt^3}$	$\Theta(x) = \frac{6F_x x(2L-x)}{Ewt^3}$
Vertical Moment M	$C_{\Theta_z} = \frac{6L^2}{Ewt^3}$	$\Theta_{\max} = \frac{12ML}{Ewt^3}$	$\Theta(x) = \frac{3F_x hx}{Ewt^3}$
Lateral Moment T	$C_\alpha = \frac{3L}{Gwt^3}$	$\alpha_{\max} = \frac{3TL}{Gwt^3}$	$\alpha(x) = \frac{3F_y hx}{Gwt^3}$

TABLE 5.1: Deflection and reflection properties of a bar shaped cantilever where L denotes the length, w the width and t the thickness of the cantilever. h stands for the height of the tip, F_x and F_y for the vertical and lateral force acting on the tip, Θ and α the vertical and lateral back angle, E the elastic modulus and G the shear modulus with $G = E/2(1+\nu)$ of the cantilever [74, 77].

properties of the normally used cantilevers in this work ("ContPt" from Nanosensors) are given in Table 5.2. The stiffness and force constants in the different directions are as follows:

- Vertical Bending
  In this case the force constant k_z is inversely proportional to the stiffness C_z.
  C_z = 3 m/N
  k_z = 0.33 N/m
  This value is close to the nominal value of 0.2 N/m from the manufacturer and well within the specified range of 0.02 N/m - 0.77 N/m.

- Vertical Torsion
  Here the effective force constant is the inverse of the stiffness multiplied by the effective height H of the cantilever, where H is the height of the tip plus half the height of the cantilever [74].
  C_Θ=10^4 N^{-1}
  k_Θ = 6.25 N/m
  Note that this value is more than one order of magnitude larger than the force constant for vertical bending.

- Lateral Torsion
  In this case the force constant is the inverse of the stiffness multiplied by the squared effective height H of the cantilever [74].
  C_α=2.75·10^7 $N^{-1}m^{-1}$
  k_α = 141.88 N/m
  This value is again more than one order of magnitude larger than the force constant of the vertical bending. This result has to be taken into account when performing friction related measurements. If the force acting laterally on the tip is smaller than the restoring force of the cantilever, no torsion can be detected. However, when using in-plane PFM on

grains the lateral force created by the grains is extremely large in comparison to restoring force so that the high force constant does not pose a constraint on the measurement.

Geometry		
Cantilever length	L	450 μm
Cantilever width	w	50 μm
Cantilever thickness	t	2 μm
Tip length	h	15 μm
Bulk E-modulus	E	304 GPa
Poisson's ratio	ν	0.24

TABLE 5.2: Mechanical properties of the used cantilever ("ContPt" from Nanosensors).

5.2 Piezoresponse Force Microscopy

PFM is the most widely used scanning method to visualize ferroelectric domains by the converse piezoelectric effect [78]. The high spatial resolution has made PFM an indispensable tool in the study of ferroelectric structures, ferroelectric switching, direction of polarization and the ferroelectric limit [9, 79–82].

In PFM a conductive tip is used in an AFM. As shown in Fig. 5.5 this tip is brought into contact with the surface of a piezoelectric material and acts as a movable top electrode. An AC voltage is applied via the tip to the sample leading to a piezoelectric response (converse piezoelectric effect). This response is mechanically passed on to the cantilever and can be optically detected by the movement of the reflected laser on the four quadrant AFM photo diode. The piezoelectric response having the same frequency as the excitation frequency can be extracted from the signal of the photo diode. One method to achieve this is to use a lock-in amplifier. In order to analyze the response in the two directions parallel and vertical to the sample the signal of the photo diode is grouped into $t-b' = (a+b)-(c+d)$ for the out-of-plane movement and $l - r = (a + c) - (b + d)$ for the in-plane movement (Fig. 5.5).

As standard lock-in amplifiers display the measured signal in different ways (R and φ or real and imaginary part) the question arises which one has to be used for PFM. This issue will be addressed next. Furthermore in an effort to fully characterize ferroelectric materials with respect to the polarization vector, a 3-dimensional analysis is mandatory [19]. This requires a complete measurement of in-plane and out-of-plane piezoresponse and also a sample stage

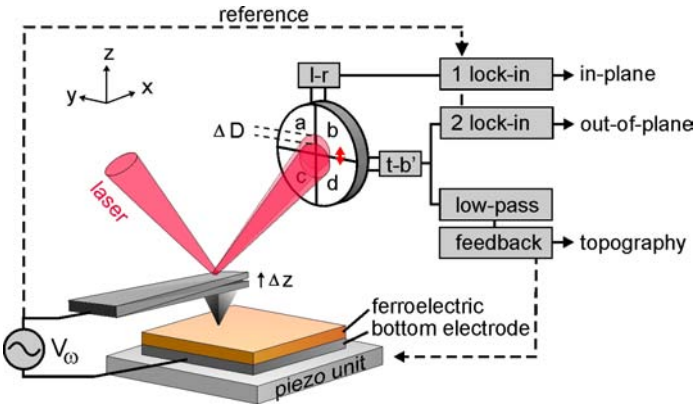

FIGURE 5.5: Principle of Piezoresponse Force Microscopy. The mechanical movement of the cantilever is optically detected by the four quadrants a, b, c and d of the photo diode. To differentiate between the two directions z and x, the signals from the quadrants are grouped into $t = a + b$ and $b' = c + d$ (for out-of-plane movement) as well as $l = a + c$ and $r = b + d$ (for in-plane movement) and connected to lock-in amplifiers. The output of the two amplifiers is proportional to the piezoresponse in the respective direction (adapted from [32]).

which can be rotated by 90°. Therefore I present a setup and measurement results where all the required properties (out-of-plane and in-plane amplitudes as well as their phases) can be measured simultaneously. Finally the potential distribution beneath the tip as well as the distortion factor of the PFM-setup will be addressed.

5.2.1 Amplitude and Phase

Lock-in amplifiers can be used to detect and measure very small AC signals, even when the signal is obscured by noise orders of magnitude larger [83]. To achieve this the detected signal

$$V_{in} = A \cdot \cos(\omega t)$$

is multiplied by a reference signal

$$V_{ref} = B \cdot \cos(\omega t + \varphi),$$

where A and B represent the amplitudes of the respective signals, φ the phase shift between them, ω their angular frequency, and t the time. Multiplying these two signals and applying the

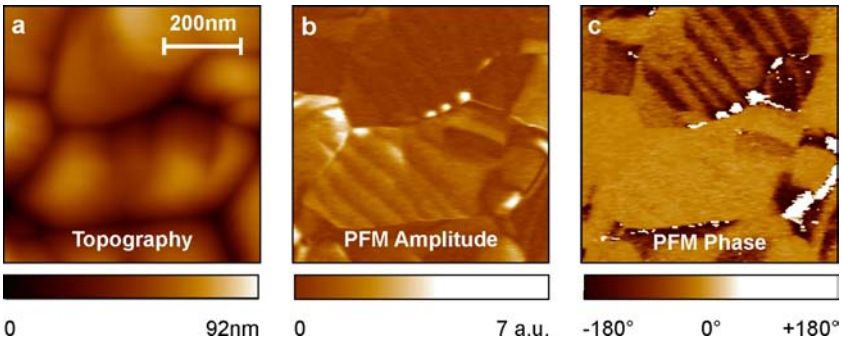

FIGURE 5.6: In-plane PFM scan showing the importance of measuring both the amplitude and the phase. Judging from the amplitude (part *b*) only the bottom left area is assumed to consist of domains. From the phase image (part *c*) it can be seen that 180° domains exist in the top right area.

trigonometric formulas leads to [84]:

$$V_{out_X} = V_{in} \cdot V_{ref} = \underbrace{\overbrace{\frac{1}{2}AB}^{R}\cos\varphi}_{X} + \frac{1}{2}AB\cos(2\omega t + \varphi). \tag{5.4}$$

As the magnitude B of the reference frequency is kept constant, the DC part of the output V_{out_X} can be seen from equation 5.4 to be proportional to the magnitude of the input signal A as well as to the cosine of the angle φ between both signals. The AC part of V_{out_X} is found at a frequency of 2ω, which can easily be suppressed by a low pass filter. If the measured and the reference signal have a phase shift of $90°$ the frequency-independent part of equation 5.4 becomes zero. This can be counterbalanced by calculating the output relative to a $90°$ shifted reference signal V'_{ref}:

$$V'_{ref} = B \cdot \cos(\omega t + \varphi - 90°)$$

$$V_{out_Y} = V_{in} \cdot V'_{ref} = \underbrace{\overbrace{\frac{1}{2}AB}^{R}\sin\varphi}_{Y} + \frac{1}{2}AB\sin(2\omega t + \varphi)$$

The output signal can be represented by the complex amplitudes X (real part) and Y (imaginary part). Alternatively, it can be displayed as an amplitude R and a phase shift φ between the excitation and the detected signal. Mathematically these are equivalent descriptions:

$$R = \sqrt{X^2 + Y^2} \qquad\qquad X = R \cdot \cos\varphi$$

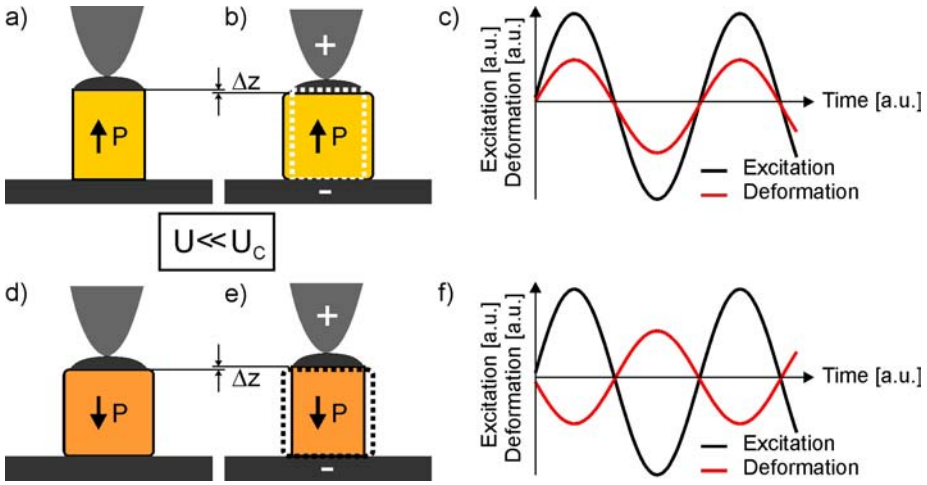

FIGURE 5.7: Principle of a phase shift originating from different polarizations. In the upper images the polarization is pointing upwards. Parts (a) and (b) show the piezoelectric contraction if a positive voltage is applied to the material. The height difference between before and after applying a voltage is given as Δz. In case of a sinusoidal voltage no phase shift exists between the excitation and the deformation (part c) as long as a contraction is defined as a positive deformation. For a polarization pointing downwards (d-f) -this is in combination with the top images equivalent to 180° domains- a 180° phase shift can be monitored.

$$\varphi = -\arctan\frac{Y}{X}, \quad 0^\circ \leq \varphi \leq 180^\circ \qquad\qquad Y = R \cdot \sin\varphi$$

Many standard lock-in amplifiers have a higher bandwidth for X and Y than for R and φ [83]. Recording X and Y thus results in clearer and sharper images. However, in most cases R and φ are the more meaningful values. The amplitude R corresponds to the piezoresponse without taking a phase shift into account. This is important if the piezoresponse is compared at different places. The phase shift φ is essential to determine the kind of domains present i.e. 90° or 180° domains. Although this information is also contained in the real and imaginary part, it cannot be extracted at a glance. Furthermore, when recalculating the amplitude and phase from the real and imaginary part the noise is doubled. Especially when presenting the phase, the real and the imaginary part, the used scale is important in order to be able the compare responses directly and to properly locate the values where a sign change occurs.

To obtain a complete piezoelectric picture, both amplitude and phase (or alternatively the real and the imaginary part) have to be recorded. Fig. 5.6 demonstrates the importance of measuring the PFM amplitude and the phase. In-plane piezoresponse is recorded on PTO nanograins prepared by a Chemical Solution Deposition (CSD) method described in chapter 6.1. The measurement is done on a commercial JEOL JSPM4210 AFM by applying 1 V at 7 kHz to

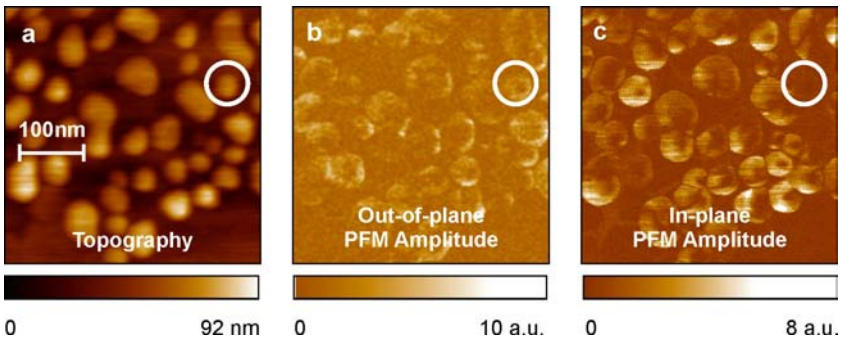

FIGURE 5.8: Topography (part a), out-of-plane PFM amplitude (part b) and in-plane PFM amplitude (part c) of PTO nanograins measured under UHV conditions. Note that the circled grain does not show any in-plane response but a clear out-of-plane response.

PtIr-coated tips from Nanosensors. Judging from the PFM amplitude only the bottom left part is assumed to consist of domains. From the phase image it can be seen that 180° domains exist in the top right area. Fig. 5.7 schematically depicts this situation. In the top images the polarization is pointing upwards. If a positive voltage (part b) is applied via the tip the undeformed piezoelectric grain (part a) contracts vertically. The excitation and deformation are in-phase, provided that a contraction is regarded as being positive on the length scale (part c). Parts ($d - f$) show the case where the polarization is pointing downwards, i.e., a change of 180° compared to the previous case. Using the same conventions for the direction a 180° phase shift (and no amplitude change) can be observed between the excitation signal and the deformation.

5.2.2 In-plane and Out-of-plane Response

In order to be able to partially determine the direction of the spontaneous polarization, an in-plane and out-of-plane piezoresponse image has to be recorded [73]. An example of such a measurement is given in Fig. 5.8. The measurement is done on a Jeol JSPM 4610 under UHV conditions after desorption according to chapter 7.1. The used PTO sample is also fabricated by CSD. Note the circled grain: it shows a relatively clear out-of-plane piezoresponse but no in-plane response. In 7.4 it is shown that in crystalline (001) orientated grains contacted by an AFM tip the out-of-plane piezoresponse is a function of the applied electric field in all three directions whereas the in-plane response only depends on the electric field in two directions. The magnitude of the electric field in one particular direction is strongly dependent on the shape of the grain as well as that of the cantilever. If the polarization is not perpendicular to the surface and for certain piezoelectric constants, the situation can occur where the response

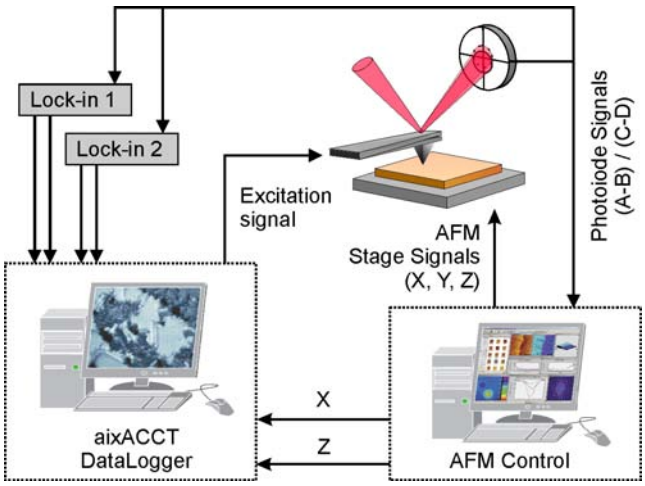

FIGURE 5.9: Overview of the multichannel measuring system consisting of an AFM, two lock-in amplifiers, an I/V converter and an aixACCT data acquisition system.

only exists in one direction. This aspect is especially important in the quest for the ferroelectric limit, where the main focus lies in distinguishing between ‘response’ and ‘no response’. Unless it becomes possible to sequentially fabricate a ferroelectric capacitor unit cell by unit cell the limit is necessarily determined by negative findings for capacitors below a certain size. In other words, this limit is investigated by crossing it experimentally. For a meaningful analysis it is vital to record both the in-plane and the out-of-plane response.

5.2.3 Multichannel Measurements

From the previous sections it follows that four different images have to be recorded in order to reliably differentiate between ’response’ and ’no response’ of piezoelectric nanograins: Out-of-plane amplitude and phase as well as in-plane amplitude and phase. Unfortunately most AFM’s have at most two additional input channels. It is not possible to measure all required signals simultaneously. Obtaining the images one after another has two major drawbacks: Especially when the scan size is very small the system drift can be considerable. Secondly, depending on the sample and the applied voltage, a scan can manipulate the material which in some cases is even used as a patterning method [85]. This manipulation influences the second scan. Therefore it is highly desirable to measure the four signals simultaneously.

In order to record more channels an 8-channel aixACCT Datalogger has been adapted to the needs of this work. This makes it possible to measure up to 7 channels concurrently (the eighth channel is required for synchronization). A schematic of the setup is shown in Fig. 5.9.

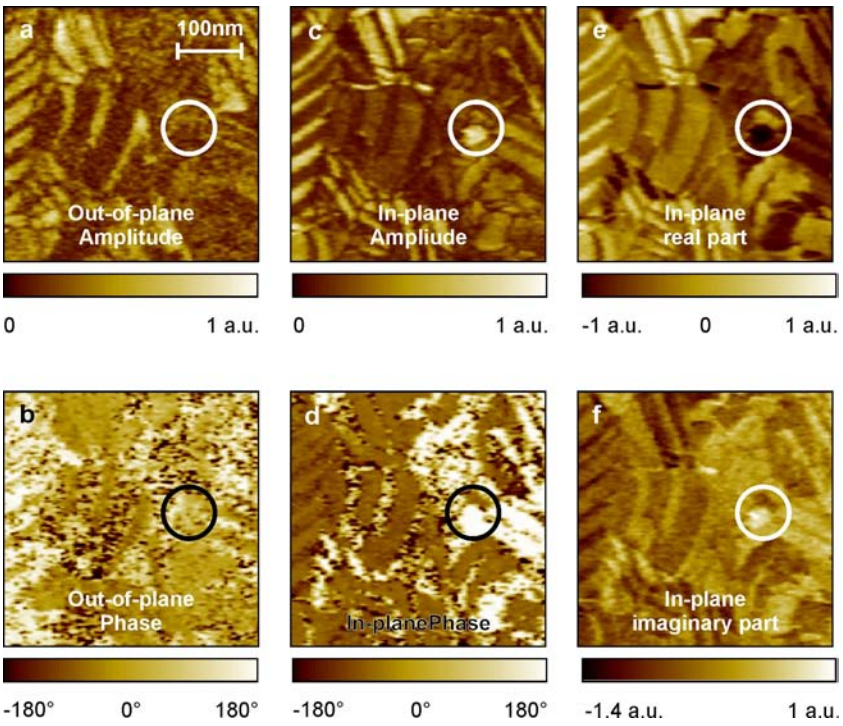

FIGURE 5.10: Multichannel measurements showing the out-of-plane piezoresponse amplitude and phase (parts a and b), the in-plane piezoresponse amplitude and phase (parts c and d) the real and imaginary part of the in-plane response (parts e and f). Note the better resolution in the real and imaginary images due to a higher bandwidth of the lock-in amplifier in this measuring mode.

Comprehensive PFM results are given in Fig. 5.10. PTO nanograins prepared by chemical solution deposition have been measured under ambient conditions. The same sample as for Fig. 5.6 has been used. A voltage of 1 V at 7 kHz is applied to the tip. Here a situation comparable to the one given in Fig. 5.8 can be seen in the circled area. In the lower half of this area practically no out-of-plane piezoresponse is monitored (part a and b) whereas the in-plane response (part c and d) is the maximum of the complete scan. Note the different optical impression given of the in-plane image when plotting the amplitude (part b), the real part (part e) and the imaginary part (part f).

5.2.4 Potential Distribution

Changing the size of the top electrode from a macroscopic size > 1 μm down to a electrode of only a few nm diameter created by an AFM cantilever has a drastic influence on the potential

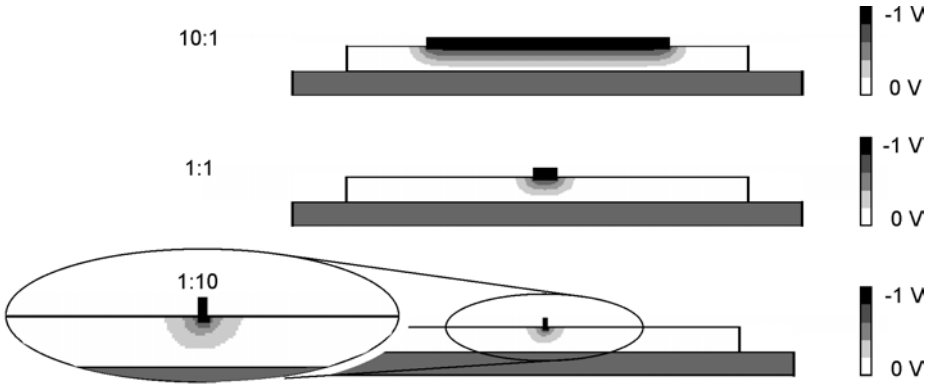

FIGURE 5.11: Influence of the top-electrode size on the potential distribution [86].

distribution. Figure 5.11 shows a FEM simulation. In the model a 50 nm BTO thin film is placed on top on a large platinum bottom electrode. The lateral sizes of the top electrodes used are 500 nm, 50 nm and 5 nm. In the first case the setup can be regarded as a parallel plate capacitor as the ratio between the width of the electrode and the height of the dielectric is ten. Apart from the edges the potential distribution is parallel to the substrate.

Measurement values obtained by a large electrode correspond to the bulk properties of the material. Reducing the lateral size of the electrode to one tenth of the thickness of the dielectric results in a radial potential distribution, as can also be seen in the simulation. For an isotropic material the potential difference ΔU between a spherical point contact with a radius r_0 and a potential U_0 and an observation point P at a distance r from the center of the sphere is given by [87]

$$\Delta U = U_0 \left(1 - \frac{r_0}{r}\right). \tag{5.5}$$

This leads to a potential U at the point P of

$$\frac{U}{U_0} = \frac{r_0}{r}. \tag{5.6}$$

This dependency is depicted in Fig. 5.12. 50% of the potential drops within a distance of the diameter of the tip, 75% in $4r_0$. Using a hemisphere instead of a planar electrode leads to similar results [88]. This opens the door to measure electrical and electromechanical properties such as σ, ε, P and d_{ij} on a local scale. Provided that the measurement problems are overcome, the obtainable resolution is mainly limited by the size of the electrode. The nanometer regime can be reached by using a conductive AFM-tip.

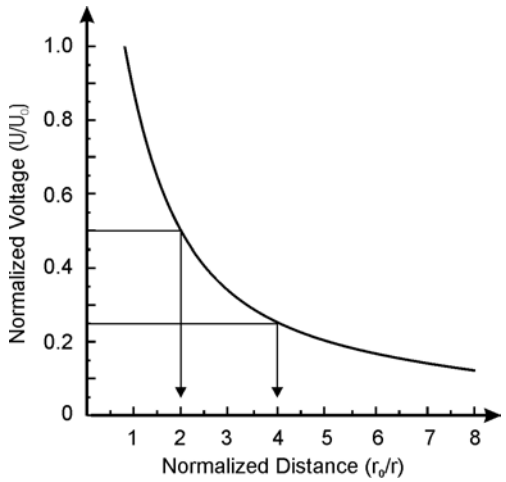

FIGURE 5.12: Potential drop as a function of distance (adapted from [86]).

5.2.5 Distortion Factor

The harmonic distortion k is a measure for the distortions produced by a nonlinear system. Usually it is used for electrical or acoustical signals where the aim is that electronic devices should influence these signals as little as possible. The distortion factor indicates the influence of the higher order harmonics created during the distortion of a sinusoidal signal on the total signal. It gives the relationship of the rms of the first harmonic to the rms of the total signal. Mathematically it is described as [89]

$$k = \sqrt{\frac{U_2^2 + U_3^2 + \ldots}{U_1^2 + U_2^2 + U_3^2 + \ldots}}$$
$$D_k = -20 \cdot \log_{10} k$$

with D_k giving the value in dB.

In PFM the excitation signal is sinusoidal and when a lock-in amplifier is used the sinusoidal response at a given frequency is analyzed. This raises the question of the linearity of the setup. Nonlinearities can arise from material characteristics prevalent at high fields.

As a first approximation of the distortion factor I determined the different harmonics in a normal PFM setup. Both the out-of-plane as well as the in-plane response of a BTO single crystal (1 mm thick, epipolished on both sides) and a PTO thin films (prepared by CSD with a 1:1 diluted precursor) are measured. The calculated distortion factors are given in table 5.3.

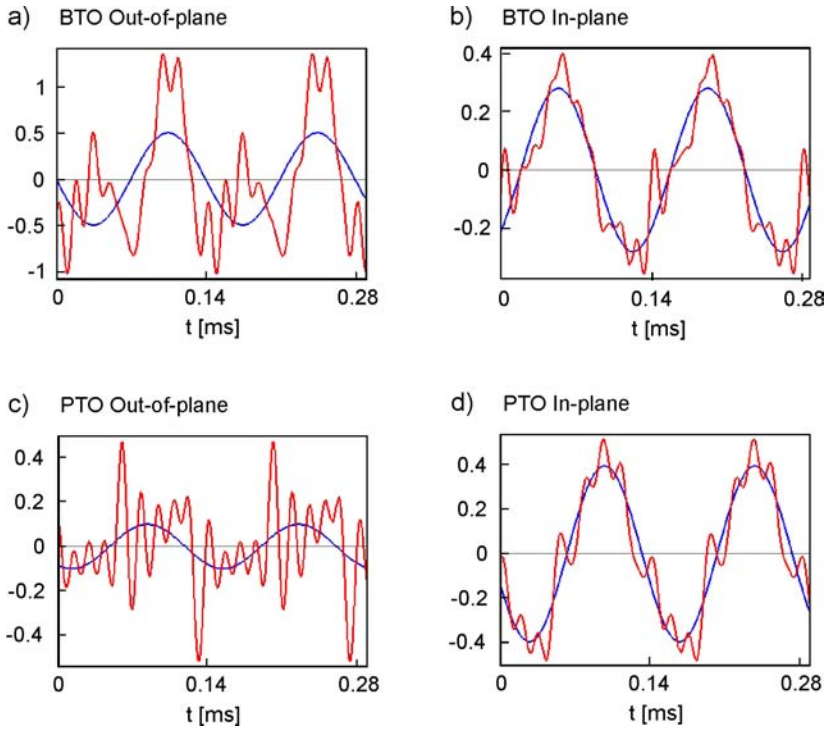

FIGURE 5.13: Distortion factor measured on a BTO single crystal and a PTO thin film. The blue lines indicates the first harmonic, the red lines the sum of the first nine harmonics.

A plot in the time domain of the first nine harmonics of the four different cases is shown by the red lines in Fig. 5.13. For these graphs the amplitude and the phase of the piezoresponse is taken into account. The blue lines indicate the first harmonic and correspond to the signal normally recorded in PFM. In both cases the in-plane response is far less distorted than the out-of-plane response which corresponds to the numerical values given in table 5.3. A possible explanation for this effect is the higher optical amplification in the lateral direction compared to the vertical direction. This is discussed in detail in chapter 7.2. The previous sections have shown that -although the principle is simple and good results have already been obtained- there are many subtleties in PFM. Especially when examining grains instead of thin films and when analyzing the in-plane response, many different aspects have to be taken into account which until now have often been neglected. These extrinsic influences on PFM are presented and discussed in chapter 7.

	BTO [%]	BTO [dB]	PTO [%]	PTO [dB]
Out-of-plane	0.84	1.54	0.93	0.70
In-plane	0.36	8.80	0.32	9.99

TABLE 5.3: Distortion factor measured on a BTO single crystal and a PTO thin film.

5.3 Cantilever Stiffness

In section 5.1.3 the cantilever stiffness has been determined for different cases. The question arises how important the force constant is for PFM. As the piezoelectric forces are very large, one would expect that the influence is rather small. If, however, the force constant is very high and the load on the cantilever also very big (and keeping in mind that the AFM adjusts the height so that the force is constant), a situation can occur where the sample cannot be considered to be in a free but rather in a clamped state. This would alter the measurement quite drastically. As a result, a compromise has to be found between soft cantilevers not clamping the sample and stiffer ones which ensure a good electrical contact. Especially in the presence of adsorbates (see section 7.1) a stiffer contact may penetrate the contamination layer thus creating a better electrical contact.

Fig. 5.14 shows topography (500 nm $\times$ 500 nm), in-plane and out-of-plane PFM measurements made with different cantilevers on a (001) orientated $Pb(Zr_{0.52},Ti_{0.48})O_3$ prepared by chemical solution deposition. In part a "CSC 12/W2C" Cantilever from μmash with a force constant of k = 0.95 N/m are used. Hardly any piezoresponse can be seen. For the measurements presented in part b a "CSC 12/W2C" Cantilever from μmash with a force constant of k = 0.08 N/m is used. The topography is comparable, but the piezoresponse shows more detail. The best piezoresponse can be seen in part c where cantilevers from Nanosensors ("ContPt") with a force constant of k = 0.03 N/m are used. As these cantilevers show the best results, they have been used throughout this work.

5.4 Domain Engineering

An electric field exceeding the coercive field applied by a conductive AFM tip in contact with the ferroelectric toggles the polarization. The tip senses the amplitude and phase of the piezoelectric response at a lower AC modulation. If the tip is moved while the DC voltage is applied, the polarization is orientated beneath the tip. With this method it is possible to write domains in the sub μm range. Often a square is polarized with a positive voltage and afterwards inside the square a smaller square is written with a negative voltage or vice versa [90–92]. This is a

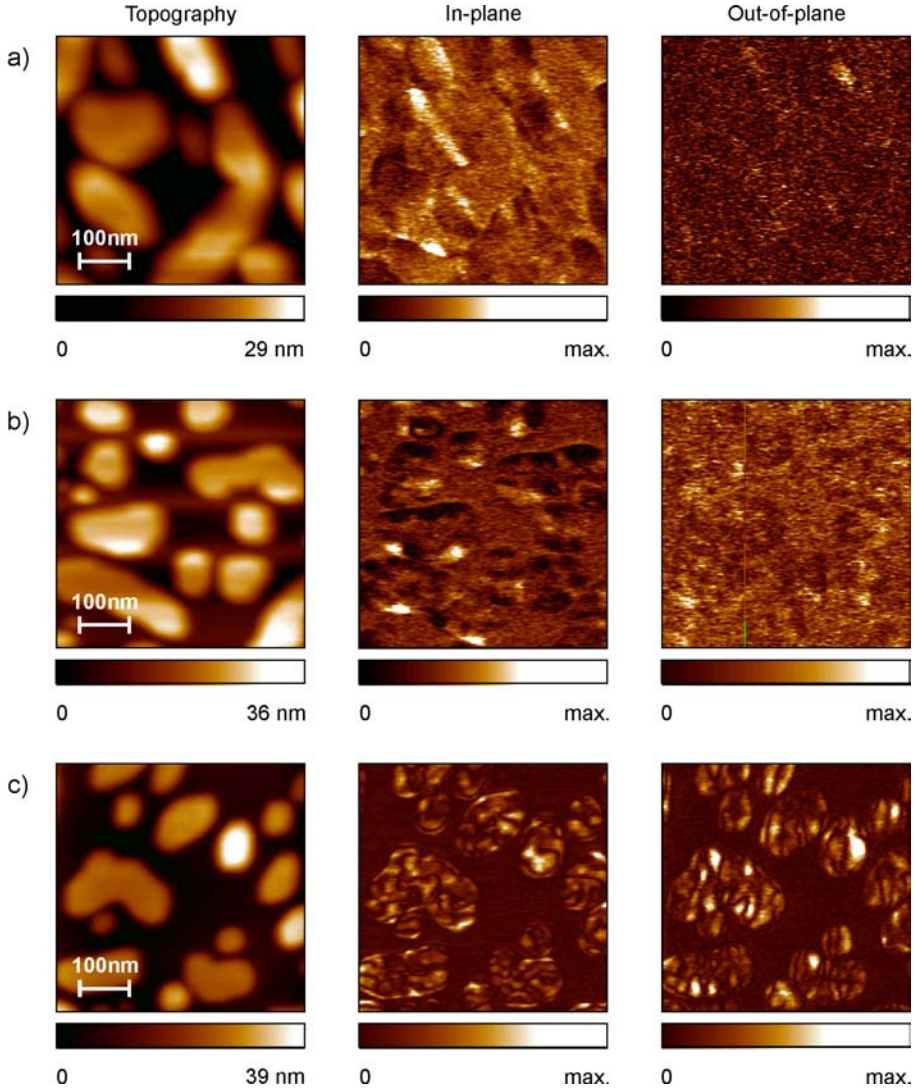

FIGURE 5.14: 500 nm $\times$ 500 nm Topgography and PFM images of the in-plane and out-of-plane amplitude with three different bar shaped cantilevers. The force constants of the cantilevers: a) k = 0.95 N/m b) k = 0.08 N/m and c) k = 0.03 N/m. Note the increasing detail which can be seen in the piezoresponse with a decreasing stiffness. In all cases black represents the lowest value and white the maximum.

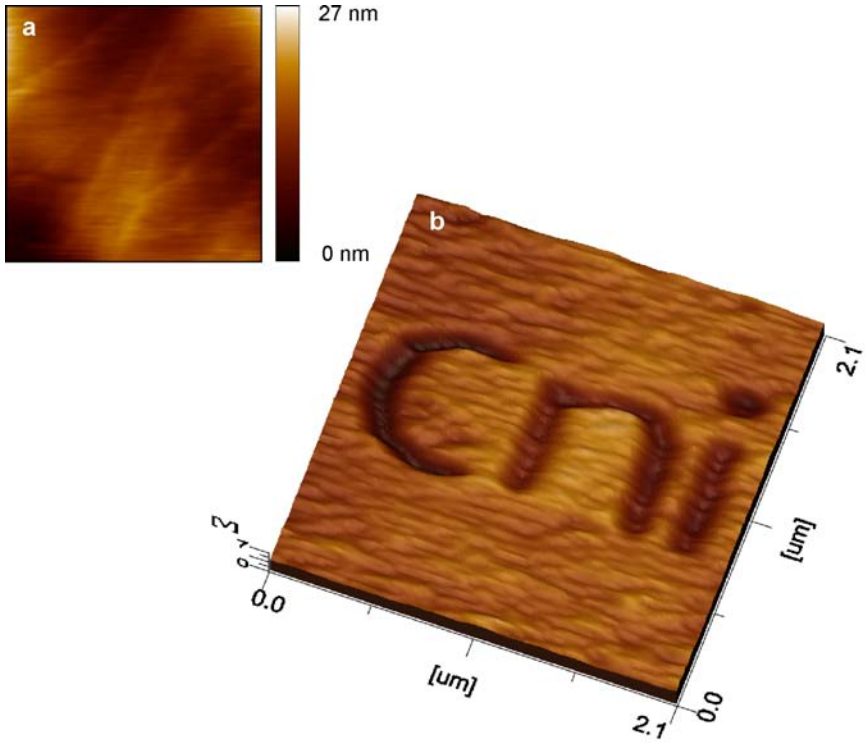

FIGURE 5.15: Topography (a) and in-plane piezoresponse (b) after the local application of +10 V DC. Domains with a width of 100 nm have been created writing the logo of the cni- Center of Nanoelectronic Systems for Information Technology.

convenient way to determine if a thin film is ferroelectric or not.

If the written domains are small enough and stable, this method can also be used to store information on the nanoscale. However, this requires control over the writing speed, the possibility to apply a DC voltage in a controlled way as well as a thorough understanding of domain wall formation, movement and pinning [93]. One result is shown in Fig. 5.15. Here the logo of the Center of Nanoelectronic Systems for Information Technology (cni) has been written into a $Sr_{0.61}Ba_{0.39}Nb_2O_6$ crystal [94] by applying +10 V DC to the tip. The speed of the tip was 100 nm/s. The in-plane readout is done with a tip voltage of 5 V at 7 kHz.

6 Sample Preparation

The nanoscale samples used in this work were fabricated in two ways: CSD and Pulsed Laser Deposition (PLD). At first the CSD-route will be described. The following sections cover two extensions of the technique: firstly to deposit ferroelectric nanograins on predefined areas (Template Controlled Deposition) and secondly to embed the grains into a dielectric layer in order to measure ferroelectric properties macroscopically. The second set of samples used in this work is prepared by PLD which is introduced thereafter. These techniques are normally used to deposit continuous thin films. As the aim of this work is to study ferroelectric nanostructures, the methods have been adapted in order to obtain grains instead of films.

6.1 Chemical Solution Deposition

The process of CSD starts with the preparation of a suitable coating solution which is then deposited onto the substrate. The basis of the solution is to manufacture a precursor that provides the components required for the designated film composition e.g. Pb and Ti for lead titanate thin films. Typically, the precursor molecules contain the metal atoms surrounded by suitable organic groups (ligands). In alkoxides, ketones and carboxylates, the metal atom is bound to the organic group through an oxygen atom. For the sample used in this work the precursor is deposited on to the substrate by spin-coating.

Depending on the chemical route chosen, the wet film may undergo drying, pyrolysis (thermal decomposition of organic solvents) and a heat treatment [32, 95]. The heat treatment for oxide thin films are usually carried out in air or in oxygen atmosphere. Typically, the desired final film thickness is achieved by multiple coating and annealing.

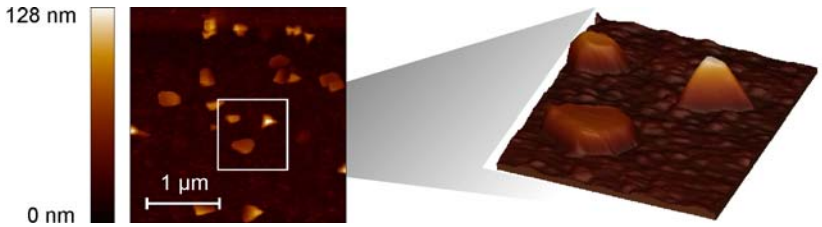

FIGURE 6.1: PTO Nanograins prepared by CSD on a Pt(111) substrate. Three coatings of a 1:50 diluted precursor have been used. Note the different orientations of the crystallites.

6.1.1 Highly Diluted Solutions

Usually the aim of CSD is to obtain a dense, polycrystalline, columnar or even epitaxial thin film. In the introduced route certain materials like PTO tend to build up films from separated grains. It is straightforward to deposit less material than required for a dense film in order to obtain single grains. This results in a bottom-up approach to manufacture nanograins. The crucial idea is to dilute the stock solution so that one coating does not contain enough material to produce a dense film [10]. Using a 1 M PTO-precursor dilution of more than 1:3 leads to single grains with a diameter between 15 nm and 200 nm. Applying more coatings leads to grains growing higher an bigger; already existing grains act as seed. Figure 6.1 shows an example of PTO grains obtained by applying three coatings of a 1:50 diluted precursor. Typically these grains nucleate along the Pt grain boundaries and show a minimum size of 15 nm as also observed by Roelofs et al. [10].

6.1.2 Lead Titanate

For the samples in this work polycristalline PTO is deposited onto commercially available Pt(111)/TiO_2/SiO_2/Si substrates. As a precursor solution the all-propionate-in-propionic acid route developed by Hasenkox et al. [96] is used. A conventional photo resist spinner is used at 4000 rpm for spin coating. The film thickness is determined by the spin speed and the viscosity of the precursor solution. After deposition the film is pyrolyzed on a hot plate at 200°C and thereafter at 400°C for 2 minutes respectively. This leads to an amorphous film exempt from all organic groups. Finally the sample is crystallized in a rapid thermal annealing oven at 700°C in oxygen atmosphere. One coating leads to a film thickness of approximately 50 nm. The film is not dense, but consists of grains with a diameter of about 100 nm to 200 nm. X-Ray diffraction measurements of the grains in combination with simulations reveal lattice constants of a = 0.3906 nm and c = 0.4100 nm. Comparing these lattice parameters of the bulk values of a = 0.3904 nm c = 0.4152 nm confirm a reduced tetragonality of 4.73% (bulk: 5.97%).

6.1.3 Lead Zirconate Titanate

The CSD procedure for $PbZr_{0.52}Ti_{0.48}O_3$ is principally the same as the one described for PTO. Dense films with a columnar structure can be manufactured. From these films the lattice parameters are determined to be a = 0.3905 nm and c = 0.4095 nm [97] resulting in a film tetragonality of 4.27%.

$PbZr_{0.52}Ti_{0.48}O_3$ nanoislands used in this work are crystallized at 800 °C on cubic $SrTiO_3$(001) [98] substrates with a Nb concentration of 0.5% wt that also serve as bottom electrodes [97,99].

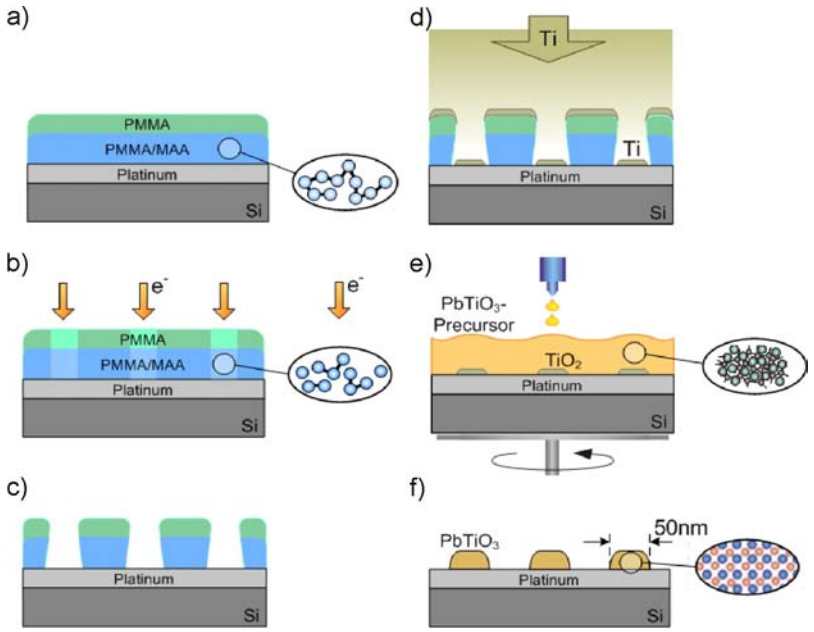

FIGURE 6.2: Schematic of $PbTiO_3$ nanostructure processing on TiO_2 seeds: (a) A two layer resist system consisting of a PMMA top and a PMMA/MAA bottom layer is spin-coated onto a platinized silicon substrate; (b) The resist layers are exposed by e-beam lithography; (c) After development an undercut resist profile is obtained as the lower resist is more sensitive; (d) A 2 nm thick titanium layer is evaporated on top of the structured resist mask. The resist is removed with a lift-off process whereupon the titanium dots are heat treated to ensure full oxidation of the titanium; (e) A highly diluted $PbTiO_3$-precursor solution is spin-coated onto the seeded substrate and dried on a hotplate; (f) Crystallization of the amorphous $PbTiO_3$-layer at 700°C yields small $PbTiO_3$ grains preferentially growing on the nucleation sites [11].

A commercial polymeric precursor [100] is diluted 1:10 with butanol. The obtained gel film is dried on a hot plate at 80°C for 5 min, pyrolized at 300°C for 5 min, and finally crystallized at 800°C for 1 h in a lead oxide atmosphere. During the high-temperature treatment, the ultrathin films break up into islands of 20 nm to 60 nm lateral size.

6.2 Template Controlled Deposition of Ferroelectric Nanograins

One of the major drawbacks of the CSD prepared nanograins introduced in the previous section is that the arrangement and size distribution of the grains can only be controlled in a very limited extent. In order to achieve a high registration which is a requirement for the integration into devices, a pre-patterning becomes mandatory [41]. Schneller et al. have proposed a

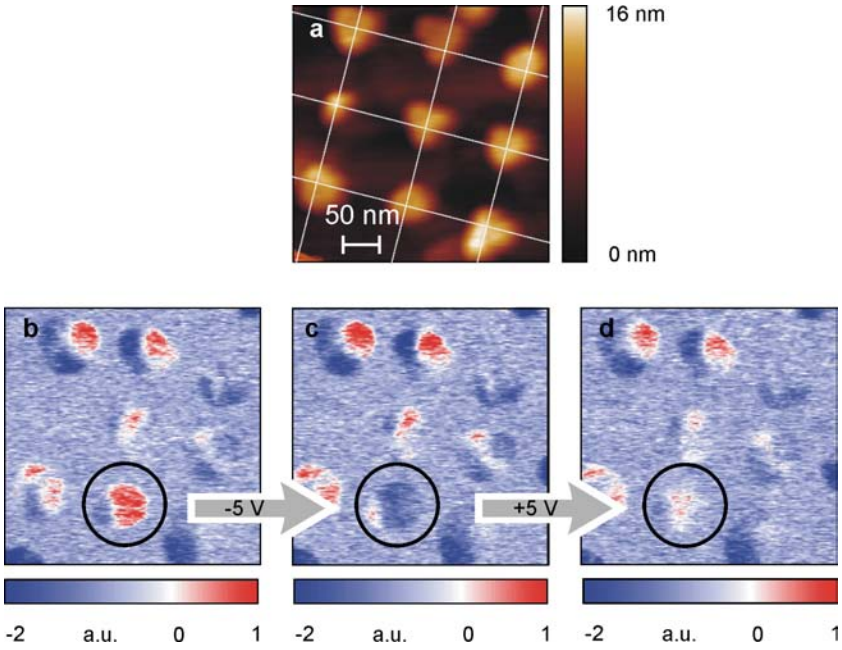

FIGURE 6.3: AFM image of PTO grains nucleated on 50 nm wide TiO_2 seeds (*a*). Inplane piezoresponse signals of the depicted grains are shown on the bottom (*b*-*d*). The polarization state of the accentuated grain is switched between single PFM scans by applying a DC voltage to the grain [11]. Note the regular arrangement of the grains as indicated by the dotted lines in part *a*.

concept which utilizes patterned TiO_2 nanograins on a bottom electrode to act as seeds for the subsequent deposition of lead based ferroelectrics [101].

Figure 6.2 shows the schematic of the process. For electron beam lithography, a two layer resist system is applied onto the platinized substrates, consisting of a polymethylmethacrylate (PMMA) top and a polymethylmethacrylate / methacrylic acid (PMMA/MAA) bottom layer. PMMA has a very high resolution among conventional electron beam resists and is therefore used for nanostructure fabrication. PMMA/MAA is higher in sensitivity, hence, undercut resist profiles can be obtained after exposure and development by using it in combination with PMMA in a two layer resist system. Especially for lift-off this is an important issue as the undercut resist profile is used as a stencil. A 2 nm thick titanium layer is then evaporated on top of the structured resist. Finally, the lift-off is done in N-methyl-2-pyrollidone (NMP). The smallest TiO_2 lines have a line width and edge to edge distance of 50 nm. The smallest dots that were fabricated reproducibly are 30 nm in diameter and have a distance of 75 nm. Similar results -although with bigger structures- have been also reported by Bühlmann et al. [102]. To grow perovskite nanostructures on the patterned TiO_2 dots and lines, a modified 2-butoxyethanol

based CSD process is applied. At first, the platinized substrate with the seed patterns is annealed at 700°C in oxygen environment to ensure full oxidation of the titanium structures. Then a $PbTiO_3$ precursor solution is spin-coated onto the samples under nitrogen atmosphere, pyrolized at 350°C and finally crystallized at 700°C to yield small nanosized perovskite grains on the platinum substrate.

The depicted results in Fig. 6.3a clearly show the promoting influence of TiO_2 seed structures on both nucleation and growth of perovskite crystals deposited by CSD. Figure 6.3b-d show PFM measurements on these grains. The piezoelectric activity is verified by applying a 1 V signal at 7 kHz via the tip to the sample. The highlighted grain is also ferroelectric as it can be switched bi-directionally by applying alternatively +5 V and -5V DC between PFM scans.

6.3 Embedded Nanostructures

Electrical characterization techniques like direct hysteresis measurements that are carried out on microscopic ferroelectric capacitors routinely today are not yet accomplished on the nanoscale, where the smallest capacitor size is limited to 300×300 nm^2 so far [35]. Therefore these measurements cannot be made directly on the nanostructures prepared by CSD as described in the previous chapters. Clemens et al. suggested to embed the ferroelectric nanosized grains in a flowable inorganic low-k dielectric layer and to contact them with collective top-electrodes [12]. In contrast to prior measurements of ferroelectric structures in parallel [103], this technique allows the direct electrical characterization of ferroelectric nanograins with e.g. variable top electrodes.

Self-assembled ferroelectric PTO nanoislands are deposited on 1 cm^2 platinized silicon substrates by the CSD technique as described in the previous sections. The amount of precursor dilution is adjusted to obtain a maximum grain height of 50 nm. After this deposition a 60 nm layer of Hydrogen Silsesquioxane (HSQ) [104] is spin-coated onto the samples, filling the space between the PTO grains and serving as an insulating layer. HSQ is a flowable inorganic polymer of silicon oxide and is widely used as interlayer dielectric due to its high planarization and low dielectric constant (ε_r = 3 at 1 MHz). The samples are then heated on a hot plate for 2 minutes at 150°C and 220°C each to remove the solvent content and to enable a flow of the deposited HSQ film, resulting in a smooth surface with completely embedded PTO structures. The films are cured at 450°C for 1 hour in a rapid thermal processing tool [12].

In order to electrically contact the PTO grains, the thin HSQ layer on top of the grains is removed by a chemical mechanical polishing step carried out on a commercial tabletop-polisher [105]. A very soft polishing pad is used in combination with commercially available Syton polishing slurry. This results in a very uniform material removal across the wafer surface.

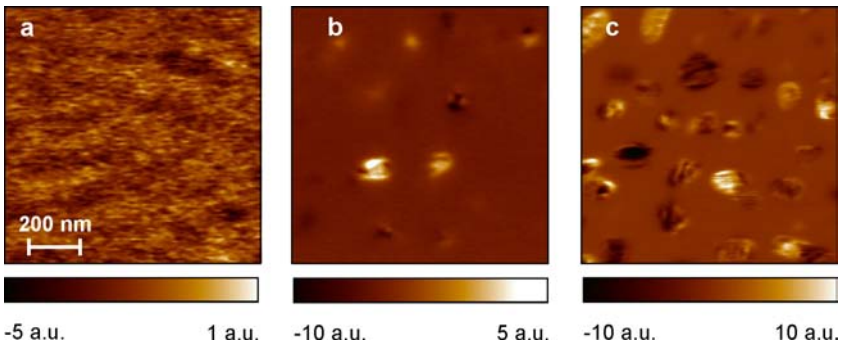

FIGURE 6.4: PFM images demonstrating the gain of piezoelectric activity with increasing polishing time. The sample of part a is unpolished, part b polished for 90 s, part c for 180 s (adapted from [12]).

The samples are polished down to the pinnacles of the PTO grains with material removal rate of about 10 nm/min. After the polishing process, the samples are cleaned in acetone under ultrasonic agitation to remove any abrasive particles. To ensure that the highest PTO grain tops are indeed electrically accessible, PFM is carried out. Figure 6.4 shows the results on a non-polished and two polished samples of different exposed grain areas. The depicted results show the increase in piezoelectric activity depending on the polishing time compared to a sample with an embedding HSQ-layer on top of the PTO grains. The piezoelectric signal indicates an electrical contact between the probe tip and the grains in case of the polished samples. In a further step collective gold top-electrodes are thermally evaporated using a simple shadow-mask technique. As these electrodes have a diameter of at least 75 μm, they contact a large amount of nanograins. With this setup it is possible to perform microscopic characterizations of ferroelectric nanostructures. Results and the interpretation thereof can be found in [12].

6.4 Pulsed Laser Deposition

The concept of PLD is shown in Fig. 6.5. A pulsed laser is focused onto a target which is mounted opposite to a substrate in a vacuum chamber. Depending on the absorbed laser energy, the surface of the target material is vaporized or at higher energies all chemical bonds are broken immediately and the target atoms are ionized so that a plasma is formed [32]. The big advantage of PLD over other deposition methods is that almost all materials can be deposited as long as they absorb the used laser light. Normally krypton flourine (KrF) or argon flourine (ArF) excimer lasers with wavelengths of 248 nm and 193 nm respectively are used. This corresponds to photon energies of 5 eV and 6.4 eV, a value at which only very few materials are still transparent. Being an advantage of the usable materials to be deposited, this is a disadvantage for the possible materials which can be used to focus the laser. Only sapphire

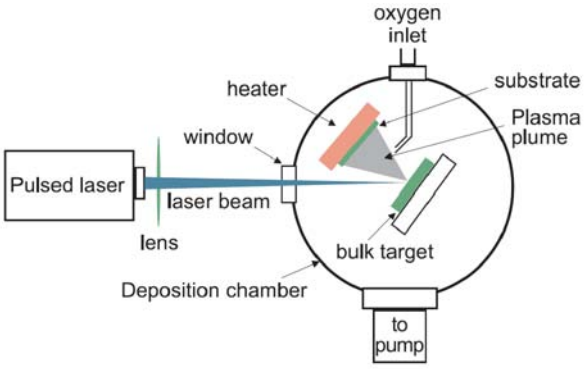

FIGURE 6.5: Set-up of a pulsed laser deposition system [73].

or MgF_2 can be used as lenses. The target can be a single crystal, a ceramic or a metal. In most cases the stoichiometry of the target is accurately transferred to the film, making PLD a convenient tool for depositing complex materials [32].

PLD can be used to grow epitaxial ferroelectric thin films on suitable single crystalline substrates if the deposition parameters like substrate temperature, oxygen partial pressure, laser energy density and substrate-target distance are appropriately chosen. For epitaxial growth the lattice parameter and the thermal expansion coefficient of the substrate and the film have to be compatible.

For this study first a $SrRuO_3$ (SRO) bottom electrode is grown on a $SrTiO_3$ (STO)(001) single crystalline substrate. During the growth of the electrode the substrate is heated to 700°C at a partial oxygen pressure of 0.25 mbar. A deposition time of 5 min results in a 50 nm thick film. Subsequently the BTO is deposited. Comparable to the dilution of the precursor in CSD, only very little material is deposited in order to obtain grains instead of a continuous film. Here a very short deposition time of 16 s is used. The substrate is again heated to 700°C and this time the partial oxygen pressure is set to 1 mbar. For both depositions a KrF excimer laser that emits 16 ns pulses at 10 Hz with an energy density of 5 J/cm^{-2} is used.

The in-plane unit cell parameters for the three materials are: [46, 106].

STO: a = 0.3905 nm
SRO: a^c = 0.3930 nm
BTO: a = 0.3992 nm
c = 0.4036 nm

In the layered STO/SRO/BTO structure, the STO substrate will stress the SRO compressively. As a result the a direction of the BTO unit cell fits better onto the SRO film than the c direction. This leads to the assumption that the BTO grains are (001) orientated. As the deposited grains

only cover an extremely small part of the substrates surface, it is up to now impossible to verify these assumptions by X-ray diffraction. However the PFM results presented in section 7.4 provide evidence that the BTO grains are indeed c-axis oriented.

7 Results and Discussion

The main focus of this work is to study surface effects and piezoresponse force microscopy on ferroelectric nanostructures. In the first part of this chapter results on adsorbates are presented. The surfaces of two ferroelectric model materials (BTO and KNO) are analyzed by XPS and PFM. Furthermore a finite element simulation is shown underlining the substantial influence of the adsorbates on the piezoresponse. These adsorbates can be partially removed by heating under vacuum conditions. Especially when determining numerical values from PFM, the experiments should be done under UHV after desorption.

The second section focuses on the different optical amplifications for the in-plane and out-of-plane directions for PFM. It will be shown that the in-plane amplification is significantly larger resulting in a better signal-to-noise ratio, making these measurements very attractive and the focus for the following sections. However, in axially symmetrical samples no in-plane response should be detected. Scenarios where a response can usually be observed are presented in the third section. Thereafter I analyze nanograins as opposed to continuous films, resulting in a number of extrinisic effects in the in-plane piezoresponse which have to be carefully differentiated from the actual intrinsic response. Here the geometry of the setup has to be taken into account as some effects are direction dependent. Finally two different kinds of crosstalk from in-plane piezoresponse into the out-of-plane response are discussed.

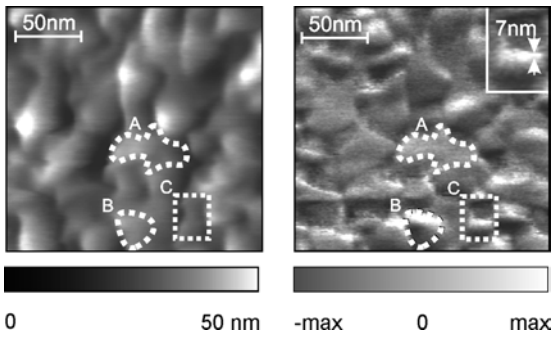

FIGURE 7.1: Topography (left) and in-plane piezoresponse measurement (right) of a $BaTiO_3$ sample prepared by CSD. The inset in the piezoresponse measurement displays an enlargement of area C and shows a domain width of 7 nm whereas practically no piezoresponse can be seen in area A [107].

7.1 Adsorbates on Ferroelectric Perovskites

One important aspect of any electrical measurement performed with an AFM concerns the contact between the probe and the sample, especially if no additional top-electrode is used and

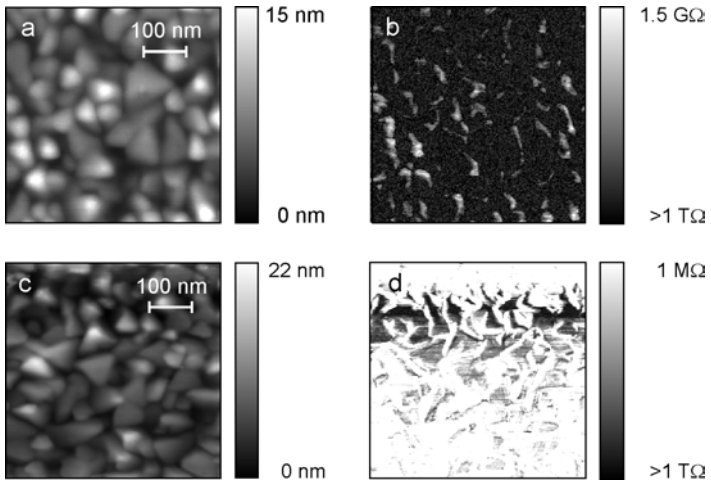

FIGURE 7.2: Local conductivity scan on platinum measured with a soft conductive PtIr coated AFM cantilever. Parts a and b show the topography and current image with contamination, parts c and d show the same sample after thermal treatment. The change in the maximum grain height is due to statistical variations at a different area [86].

the AFM tip acts as a nano-probe. The challenge is to control the interface between the tip and the specimen as shown in the following examples.

Fig. 7.1 depicts the topography and the in-plane piezoresponse of a CSD fabricated BTO sample measured under ex-situ conditions. In regions B and C domains < 10 nm can be detected, whereas in other areas (region A) no piezoelectric activity can be seen. With PFM it is impossible to determine if the chemical composition is different in regions A and B, the surface is covered by something or if size-effects are responsible for the different piezoelectric activity in the two regions. A related result can be seen in Fig. 7.2. Here a voltage of 1 V is applied to a platinum coated cantilever and the current is measured. No trend can be seen in the image e.g. that the signal reduces towards one side of the sample. A trend in the measurements could indicate that the conductive coating of the cantilever is wearing off leading to a deteriorating electrical contact. When using a new tip and measuring the resistance of a platinum coated silicon sample one would suspect to obtain a homogeneous result over the specimen. This is not the case as can be seen in the top images of Fig. 7.2. Apart from a deteriorating tip a contamination layer on top of the sample could influence the measurement significantly. This assumption is supported by the fact that the current increases drastically after heating the sample at 200°C for five minutes as presented in the bottom images of Fig. 7.2 [86].

These measurements confirm that ferroelectric samples are generally covered by some sort of contamination. The best method to analyze this is by surface sensitive methods like XPS [108].

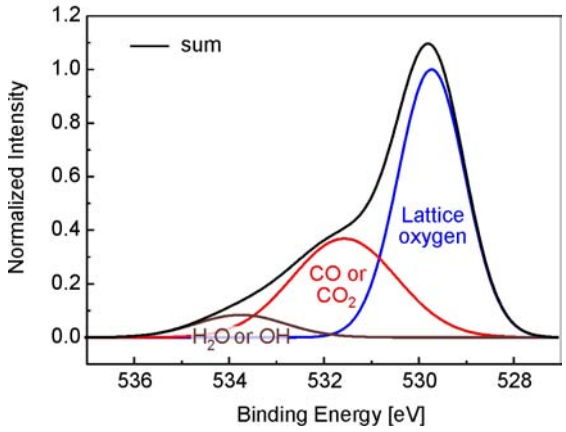

FIGURE 7.3: Core lines of a BTO single crystal at room temperature.

In this chapter the focus lies on these adsorbates, their influence on PFM measurements and a method on how they can be removed.

7.1.1 Barium Titanate

In order to have a defined chemical composition and to single out the other effects I studied the adsorbates on a stoichiometric archetype perovskite, a 5 mm $\times$ 5 mm $\times$ 1 mm BTO $(100)_{pc}$ single crystal epipolished on both sides (RMS: $\approx$ 2 nm). The structure of the real surface layer of BTO single crystal shows two additional components. The O 1s core line of this single crystal measured at room temperature by XPS is shown in Fig. 7.3. In case of an ideally clean surface only the lattice oxygen with an energy of E_1=529.8 eV exists. However, two additional components with binding energies of E_2=531.5 eV and E_3=533.8 eV are observed. These can be identified according to [109] as chemisorbed CO or CO_2 (E_2) and as physisorbed OH or H_2O (E_3). As the lattice oxygen can be detected, the thickness of the contamination layer can only be a few nm. From measurements at different angles we deduce that the chemisorbated CO or CO_2 is directly on top of the surface of the bulk material and the physisorbated OH or H_2O forms the top layer. A schematic cross-section of a contaminated surface is given in Fig. 7.4.

As the top layer is physisorbed OH or H_2O, it should be possible to evaporate it, at least partially. Heating a BTO single crystal has a big influence on the physisorbates. A treatment under UHV conditions is necessary so that no new physisorbates form from the moisture in the air. In situ XPS measurements show that above $\approx$ 350 °C H_2O and OH is removed to a large extent (Fig. 7.5). Increasing the temperature up to 800 °C leads to a reduction of the chemisorbed layer. The relative high temperature suggests that the OH groups and the last monolayers of

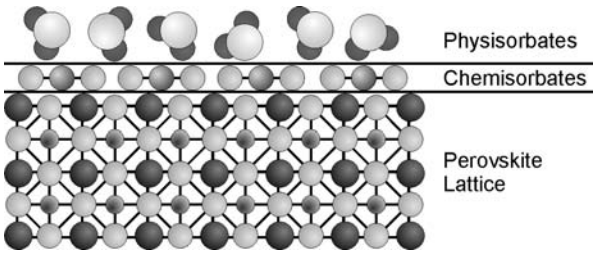

FIGURE 7.4: Model of adsorbate layers on a perovskite material

BTO form a chemical bond. After heating the sample in UHV to 800 °C it is cooled down in situ. No change in the core lines can be detected after cooling. A short exposure to ambient surrounding results in a restoration of the physisorbate layer of the surface similar to the condition before heating [107].

Having seen that perovskites are covered by physi- and chemisorbates, the question arises how these additional layers influence piezoelectric measurements. In the following I present experimental results of the impact of the adsorbates on piezoactivity measurements. All PFM

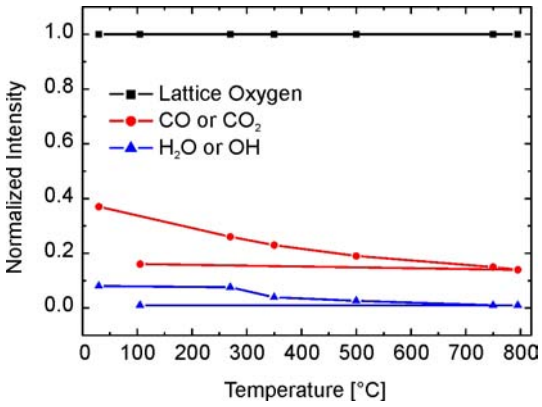

FIGURE 7.5: XPS results showing the influence of heating under UHV on the adsorbates

measurements are done on a modified Jeol 4210 AFM fitted with the commercially available heating element. To facilitate desorption the sample is heated and cooled under high vacuum ($3 \cdot 10^{-5}$ mbar) conditions. For the piezoresponse measurements of the single crystal a voltage of U=50 V_{pp} at 7 kHz is applied to the PtIr coated cantilever ("ContPt" from Nanosensors, f_0=13 kHz). The magnitude of the piezoresponse is checked to be a function of the applied generator voltage.

For the presented measurements the aim is to determine an average value of the piezoactivity

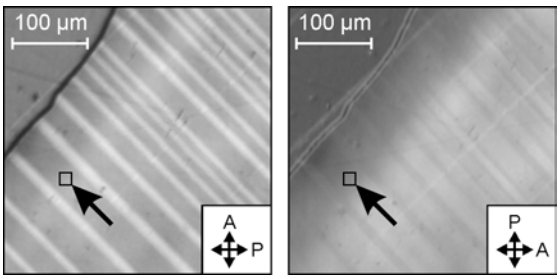

FIGURE 7.6: a- and c- domains of the BTO crystal as observed by a optical polarization microscope. In the right image the polarization of the light has been turned 90° relative to the left image. The arrows point to a typical place of a a-domain where the following PFM investigations have been made

over a relative large area as a function of the physisorbates. In the single crystal the inherent domains or those which are created by cooling the sample from above the Curie temperature T_c of 120°C are relatively large, as can be seen by the inspection with an optical polarisation microscope (Fig. 7.6). In all experiments PFM is first done under ambient conditions, thereafter under high vacuum. To be in line with the XPS measurements the sample is then heated under high vacuum to 350°C and kept at this temperature for 5 minutes. After it has cooled down to room temperature the piezoactivity is measured. Thereafter the sample is exposed to ambient conditions for a few minutes before another PFM scan is performed. In this order new domains are created between the first two and the last two measurements. Between these two sets of measurements the crystal is heated above T_c, so these results of the piezoelectric activity may not be compared directly as the domain structure might have changed. In all four scans (scan size 20 μm $\times$ 20 μm) the same area of the sample is examined. The whole series is repeated 4 times at different places. The total piezoelectric activity of the scan has been calculated as the average of the absolute value of each measurement point. From the optical inspection (Fig. 7.6) it can be seen that most domains are a-domains which can best be detected by the in-plane PFM signal. The average piezoelectric activity of all experiments is shown in table 7.1.

Condition	Piezoresponse
Ambient	100%
High vacuum	115%
High vacuum after heating to 350°C	250%
Ambient after heating cycle	100%

TABLE 7.1: Average piezoelectric activity under different surface conditions

These measurements of BTO$(100)_{\mathrm{pc}}$ single crystals reveal that a chemi- and physisorbate layer is prevalent on the surface of the perovskite leading to an additional potential drop between

the tip and the sample. In PFM measurements the layer reduces the effective amplitude of the piezoresponse by 250% in comparison to the adsorbate-free surface (in one extreme case a reduction of 800% was measured). Similar results were observed by Sugimura et al. by Kelvin Probe Microscopy on silicon structures covered by a hydrophilic oxide layer [110]. To be able to determine quantitative values for d_{ij} only samples which have been freed $in\ situ$ of the physi- and chemisorbates can be used.

The desorption measurements done by XPS under UHV conditions give the opportunity to determine the critical desorption temperature required to free the BTO surface of OH groups. This temperature is in the range of 350°C. The relative high temperature suggests that the OH groups and the last monolayers of BTO have formed a chemical bond by electron transfer. I assume that the BaO-terminated surfaces reacts in *ex situ* conditions to form $BaOH_2$ which decomposes under vacuum at higher temperatures (for bulk materials $\approx 370\ ^{\circ}\mathrm{C}$ [111]): $\mathrm{Ba(OH)_2 \rightarrow BaO + H_2O}$. However the analysis of the C 1s line shows that some CH_x is still existent after the heat treatment indicating that a complete removal of the adsorbates from the BTO surface was impossible under the available treatment.

7.1.2 Potassium Niobate

In order to provide a broader basis for this observation I will present comparable XPS and PFM measurements on KNO, another ferroelectric model material with perovskite structure. Two different situations will be compared: on the one hand a epipolished surface and on the other hand a freshly cleaved specimen of a $KNO(100)_{\mathrm{pc}}$ single crystal [112]. The KNO surface is analyzed by XPS with $\mathrm{Al_{k\alpha-mono}}$ excitation. The result for the O 1s core line at room temperature of the cleaved sample is shown in Fig. 7.7a. Four different compounds of core lines can be detected which are classified as follows [109] [111]:

- lattice oxygen with an energy of 529.8 eV
- K_2CO_3 at 531.2 eV
- KOH with an energy maximum at 532.4 eV
- H_2O or OH at 533.4 eV

The KOH and K_2CO_3 can be regarded as chemisorbates whereas the H_2O or OH is physisorbed. From measurements taken at different angles it can be deduced -similar to BTO- that the H_2O or OH layer is the topmost layer.

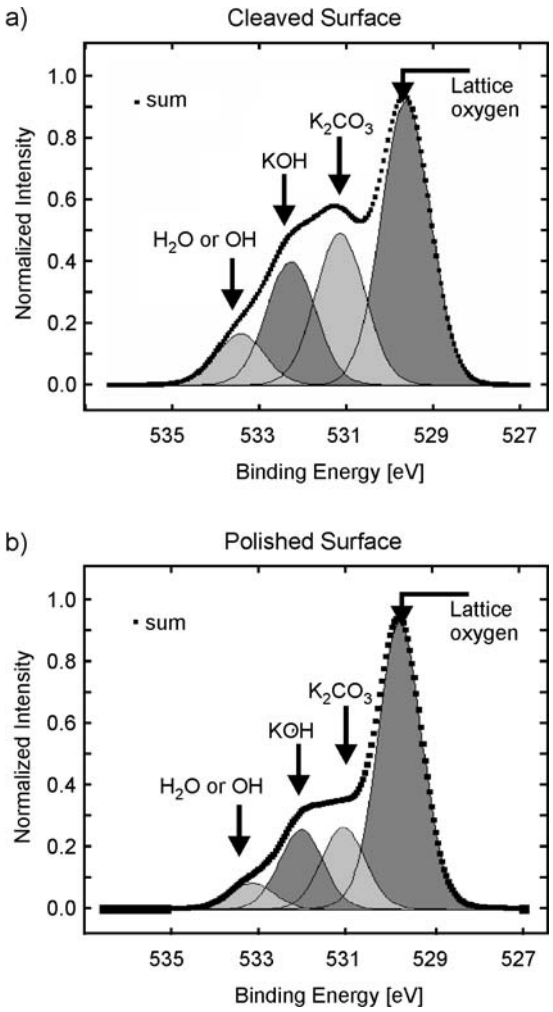

FIGURE 7.7: Deconvoluted O 1s core lines of a freshly cleaved KNO single crystal (part a) and deconvoluted O 1s core lines of a ex-situ prepared polished KNO single crystal measured by XPS at room temperature (part b)

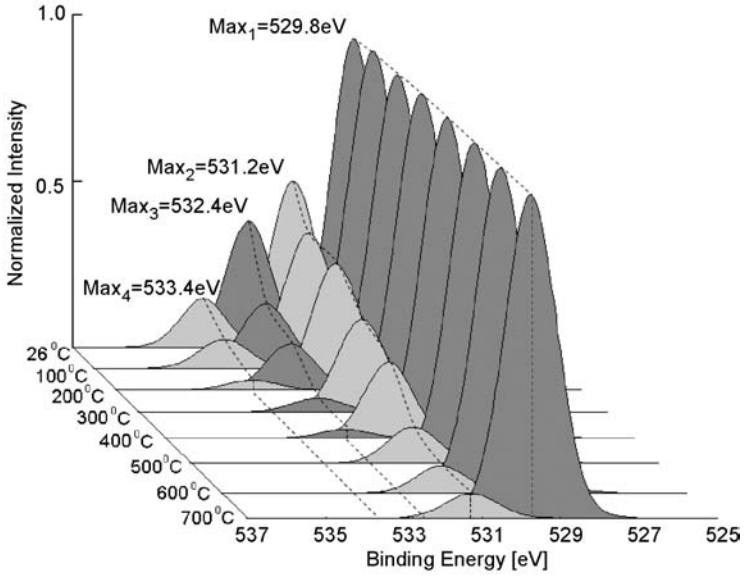

FIGURE 7.8: XPS *in situ* measurement of the 1s energy state of different oxygen compounds as a function of temperature in a freshly cleaved KNO single crystal

In Fig. 7.7*b* the O 1s core lines of an epipolished KNO single crystal are presented. Comparing these results with the cleaved sample shows that the surface of the cleaved sample is more reactive, due to new facets relative to the $(100)_{\mathrm{pc}}$ surface having an increased chemical affinity. Furthermore the cleaved sample has a better stoichiometry.

The temperature dependence of the different compounds of the cleaved crystal is depicted in Fig. 7.8. For these measurements the sample has been heated $in\ situ$ under ultra high vacuum conditions. The intensity of the lattice oxygen stays constant irrespective of the temperature. K_2CO_3 cannot be removed up to temperatures of 700°C. The other chemisorbate layer (KOH) is unstable above 400°C. The physisorbate layer can be removed when heating the sample above 200°C. These observations are in line with those reported for BTO [107].

The results obtained from the epipolished sample are similar (Fig. 7.9). Although smaller at room temperature, the KOH compound can be detected at 500°C, whereas in the case of a cleaved sample it can only be measured up to 400°C. On the other hand the H_20 or OH layer disappears below 200°C for the polished sample. Due to this lower temperature an epipolished crystal is used for the further experiments.

To facilitate desorption during PFM measurements a 5 mm $\times$ 5 mm $\times$ 2 mm epipolished KNO sample is heated and cooled under high vacuum ($3 \cdot 10^{-5}$ mbar) conditions. The setup is the

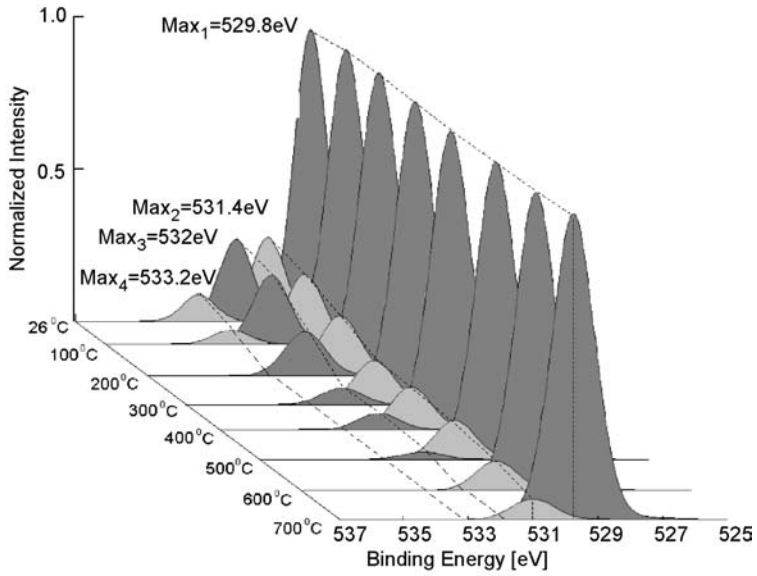

FIGURE 7.9: XPS *in situ* measurement of the 1s energy state of different oxygen compounds as a function of temperature in a polished KNO single crystal

same as for the presented BTO study of the previous section. As an example Figure 7.10 shows the topography (parts a and b) and out-of-plane piezoresponse (parts c and d) of a cleaved and a polished sample at room temperature.

The PFM experiments are first done under ambient conditions. To be in line with the XPS measurements, the sample is then heated under high vacuum to 210°C and kept at this temperature for 5 minutes. This temperature is well below the Curie temperature T_c of 418°C and the transition temperature of 225°C between the orthorhombic and tetragonal phase [46]. This means that the room temperature configuration is preserved. After the sample has cooled down to room temperature under high vacuum the piezoactivity is measured (the cooling down is required as it is impossible to measure piezoresponse at 210°C with the setup). Thereafter the

Condition	Piezoresponse
Ambient	100%
High vacuum after heating	380%
Ambient after heating cycle	115%

TABLE 7.2: Average out-of-plane piezoelectric activity under different surface conditions for the epipolished sample.

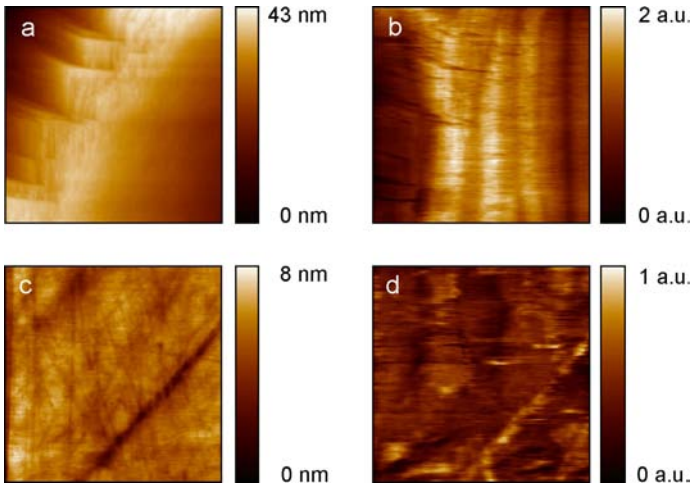

FIGURE 7.10: Topography and out-of-plane PFM measurements of KNO single crystals. In parts a and b a cleaved sample has been used and in parts c and d a polished sample. The topography is depicted in a and c, the amplitude of the out-of-plane piezoresponse in b and d. Note the crystallographic angles and clearer piezoresponse of the cleaved sample.

sample is exposed to ambient conditions for a few minutes before another PFM scan is performed. The total piezoelectric activity of the scan has been calculated as the average of the absolute value of each measurement point. The normalized out-of-plane piezoactivity is given in Table 7.2. The increased activity of nearly 400% confirms the significant influence of the physisorbates on the piezoresponse.

A finite element model is set up in ANSYS to simulate the influence of an adsorbate layer on the piezoactivity. In the model a 50 nm thick, 200 nm wide KNO crystal is contacted on the bottom by a continuous metal electrode and on the top by a conductive metal-coated AFM cantilever. A cut through the [010] direction is chosen in order to see the influence of the asymmetric piezoelectric coefficients. For the calculations the following coefficients which correlate the mechanical strain with the induced charge density are used [113]:

e_{33}= 4.4 pC/m^2
e_{31}= e_{32} = -1.1 pC/m^2
e_{15}= e_{24} = 11.7 pC/m^2

The diameter of the cantilever is set as 20 nm, which is in reasonable agreement to our used cantilevers. A voltage of 1 V is applied to the cantilever. Fig. 7.11a depicts the potential distribution and Fig. 7.11b the out-of-plane piezoresponse for the case of an ideal contact between the AFM Tip and the surface i.e. without an adsorbate layer. The complete voltage is applied

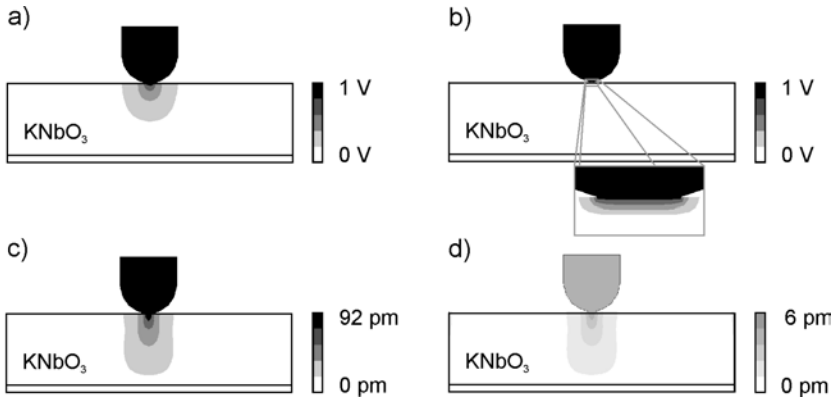

FIGURE 7.11: Simulation of the influence of a low-ε adsorbate layer on the potential distribution of a KNO single crystal. In image a an adsorbate free case is assumed whereas in b a 1 nm thick adsorbate layer has been inserted. Part c shows the out-of-plane piezoresponse an ideally clean surface whereas case d depicts the situation with an adsorbate layer.

to the actual piezoelectric material. Due to the geometry a huge part the potential drop is the highest near the tip [88]. A maximum deformation of 92 pm directly below the tip has been calculated.

A 1 nm thick adsorbate layer on top of the perovskite is considered in the simulation presented in the bottom images of Fig. 7.11. A value of $\varepsilon = 6$ is used for the thin adsorbate layer [114]. Drastic influences compared to the adsorbate-free case on the potential distribution and consequently on the piezoresponse can be seen. With the low-ε layer the voltage drops mainly across this layer whereas in the previous case the voltage drops over large parts of the KNO. As the actual voltage applied to the perovskite is considerably lower in the case of the covered sample the piezoactivity is ≈ 15 times lower compared to the uncovered surface (5.6 pm).

This difference is far more pronounced than the one determined by the measurements (380%) as the simulation is based on an idealized situation whereas in my measurements only the physisorbates could be removed.

The measurements of KNO single crystals reveal that chemi- and physisorbate layers are present on the surface of the perovskite leading to an additional potential drop in series with the tip and the actual sample. In PFM measurements the layer reduces the effective amplitude of the piezoresponse by up to 380% in comparison to the adsorbate-free surface. This follows the trend shown by Känzig in [115], where he describes the influence of a surface layer on an applied electric field. Simulations confirm that an additional adsorbate layer has a huge impact on the potential distribution and therefore on the piezoactivity. In order to determine local quantitative values of the piezoelectric constant yet another problem has to be overcome:

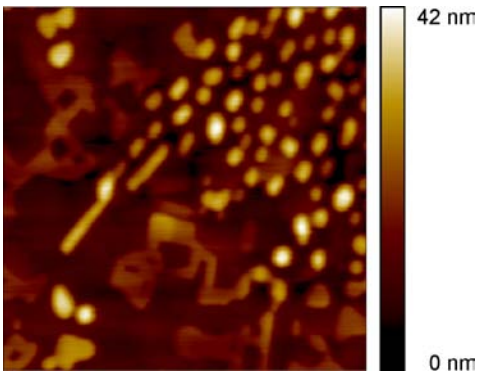

FIGURE 7.12: 750 nm × 750 nm Topography of PTO nanograins after desorption under UHV.

the removal of the adsorbate layers. The desorption measurements done by XPS under ultra high vacuum gives us the opportunity to determine the critical desorption temperature required to free the KNO surface of OH groups. This temperature is in the range of 200°C. In order to determine quantitative PFM values the measurements have to be made under ultra high vacuum conditions after *in situ* heating.

7.1.3 UHV Piezoresponse Force Microscopy

In the previous section it was shown that ferroelectrics are covered by adsorbates under ambient conditions. When measuring the piezoresponse on these samples, a considerable part of the applied electric field drops across the adsorbates so that only part of the field is applied to the crystal. When heating the sample under UHV the physisorbates are partially removed. Apart from a better electrical contact the topography should also be clearer. However, the UHV-setup is experimentally far more complex than measurements conducted in ambient conditions.

Fig. 7.12 shows the topography of a PTO sample prepared by CSD with a precursor dilution of 1:20. The sample is heated for 10 min at 300 °C in the preparation chamber (p = $5 \cdot 10^{-9}$ mbar) before being transported to main chamber (p = $9 \cdot 10^{-10}$ mbar) where the measurement is performed. For the following PFM measurement a PTO sample prepared by CSD with a precursor dilution of 1:1 has been used. The sample is desorbed under UHV analogously to the sample shown in Fig. 7.12. A voltage of 1 V at 7 kHz is applied via a 5.6 kΩ resistor to the sample. The result (Topography (a), out-of-plane amplitude (b) and phase (c), in-plane amplitude (e) and phase (f)) is shown in Fig. 7.13. A cross section given in part d shows domains with a width of 8 nm.

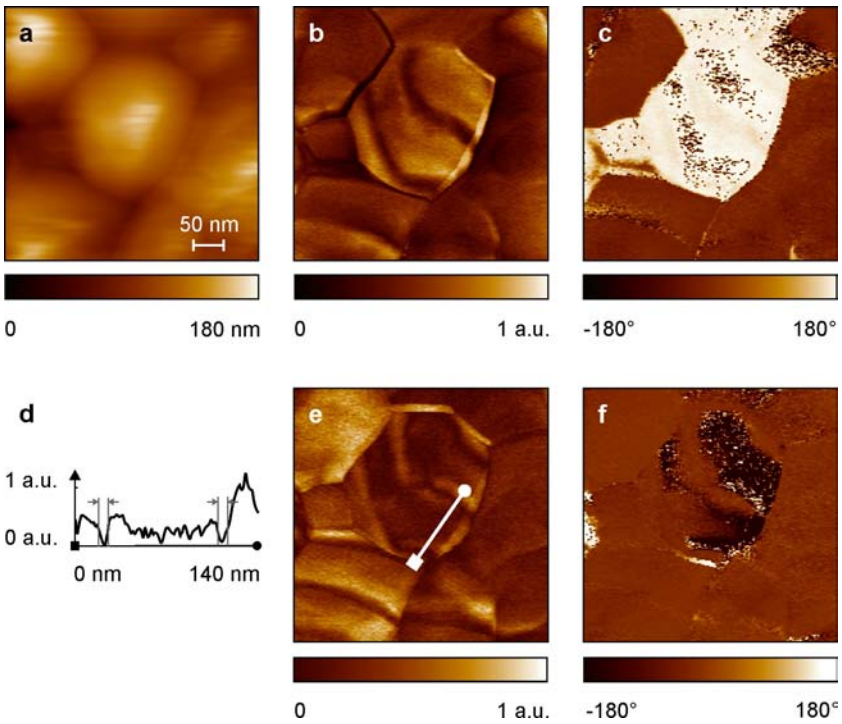

FIGURE 7.13: 400 nm $\times$ 400 nm Topography (a), out-of-plane amplitude (b) and phase (c), in-plane amplitude (e) and phase (f) measurements of PTO nanograins. The cross section given in d shows 90° domains with a width of 8 nm.

7.2 Comparison of In-plane and Out-of-plane Optical Amplification in AFM Measurements

Ferroelectrics have been successfully characterized and manipulated on the micro- and nanometer scale by PFM in recent years [9, 13, 16, 80, 116–118]. A big advance in PFM was the introduction of in-plane measurements [16, 19]. The quadrupole photo diode is used such that both laser deflections from bending as well as lateral torsion of the cantilever can be monitored simultaneously as illustrated in Fig. 7.15. In many cases the in-plane signal is substantially larger than the out-of-plane signal and therefore shows more details and less noise. A typical example of such a measurement on CSD prepared PTO nanograins is shown in Fig. 7.14. Here the in-plane response is roughly one order of magnitude larger than the out-of-plane response. The signal to noise ratio is a factor of 3.5 better in the in-plane image. As the piezoelectric coefficients for PTO vary only by a factor of five for the different directions as shown in table 7.3, the question arises if this effect can be due to a direction dependent amplification.

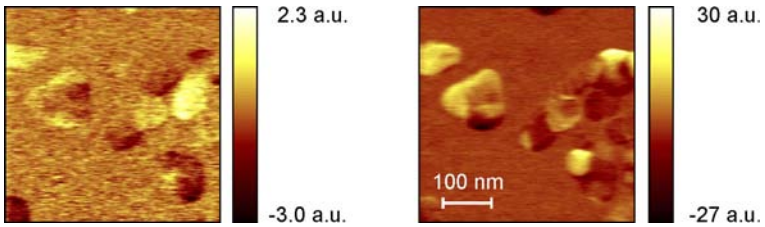

FIGURE 7.14: 450 μm $\times$ 450 μm Out-of-plane (left) and in-plane (right) PFM measurement of PTO nanograins. The signal-to-noise ratio is a factor of 3.5 better in the in-plane image

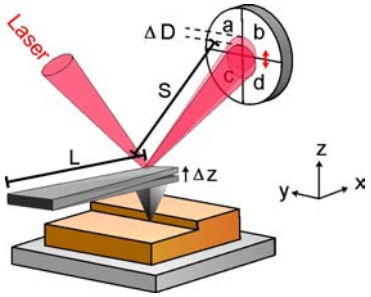

FIGURE 7.15: Optical lever arm method ΔD = movement of laser on photodiode, S = distance between cantilever and photodiode, Δz = out-of-plane cantilever movement, L = length of cantilever

7.2.1 Geometrical Considerations

The most common method used in AFMs to detect the cantilever deflection is by measuring the position of a reflected laser beam on a position sensitive detector. A schematic of this optical lever arm method is given in Fig. 7.15. The out-of-plane lever amplification

$$V_{\mathrm{out-of-plane}} = \frac{\Delta D}{\Delta z} = \frac{3S}{L}$$

is a factor of about one thousand [73]. In this case the two top quadrants (a and b in Fig. 7.15 and the two bottom quadrants (c and d) have to be regarded as one. This same principle is used

	PTO	BTO
d_{33}	11.7 pm/V	85.6 pm/V
d_{31}	-2.5 pm/V	-34.5 pm/V
d_{15}	6.5 pm/V	392 pm/V

TABLE 7.3: Piezoelectric coefficients for single crystals [46]

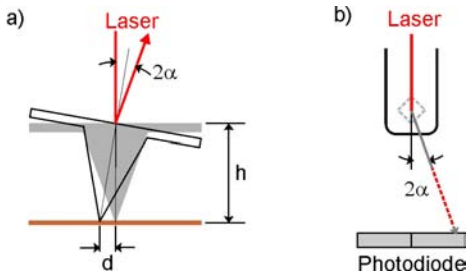

FIGURE 7.16: a) Front view and b) top view of a cantilever being bend in-plane α= tilting angle of the cantilever.

to detect the in-plane deflection; here the two left (a and c) and right (b and d) quadrants of the photo diode have to be considered as one. An in-plane movement of the tip is shown in Fig. 7.16.

I now assume that the apex of the tip moves a lateral distance d whereas the middle of the tip base remains stationary. From Fig. 7.16a and b it follows for small α:

$$\tan\alpha = \frac{d}{h} \approx \alpha \tag{7.1}$$

where h is the height of the tip plus the thickness of the cantilever. The change of the irradiated area of the left and right parts of the photodiode is a linear function of the displacement:

$$\Delta D = \sin(2\alpha) \cdot S \approx 2\alpha \cdot S \tag{7.2}$$

This results in an amplification factor of

$$V_{\mathrm{in-plane}} = \frac{\Delta D}{d} = \frac{2S}{h}. \tag{7.3}$$

The ratio R between the two amplifications is [119]

$$R = \frac{V_{\mathrm{in-plane}}}{V_{\mathrm{out-of-plane}}} = \frac{\frac{2S}{h}}{\frac{3S}{L}} = \frac{2}{3}\frac{L}{h} \tag{7.4}$$

and only depends on the cantilever geometry. This optical amplification has to be taken into account for all kinds of AFM measurements involving the detection of a horizontal and a lateral movement of the cantilever.

For typical cantilevers used in this work with a length of 450 μm and a tip height plus cantilever thickness of 12-17 μm [120] this ratio is:

$$18 < R < 25$$

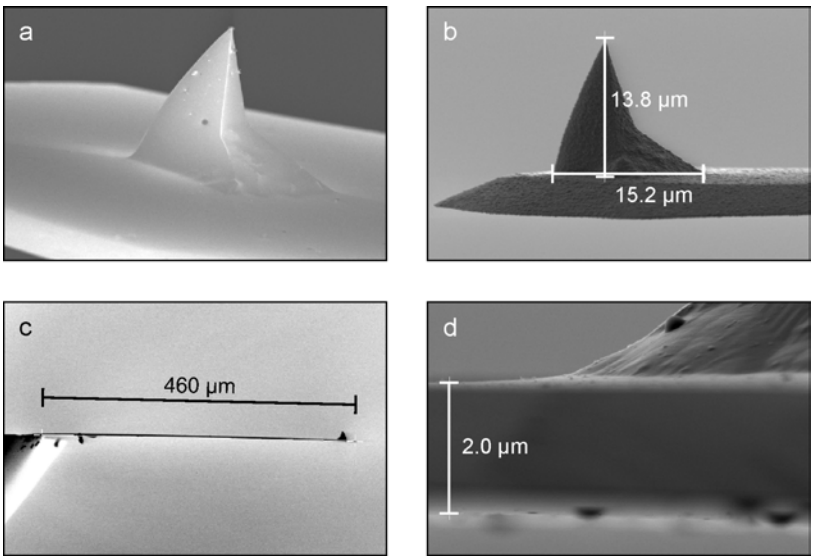

FIGURE 7.17: SEM images of AFM cantilevers [121] showing an overview (a) and different side views (b-d). The measured tip is 13.8 μm high (b), the cantilever 460 μm (c) long and 2 μm thick (d).

To confirm the dimensions given by the manufacturer I measured the used tips with Scanning Electron Microscopy (SEM). The images are shown in Fig. 7.17 and they confirm the specifications. The tip height is measured as 13.8 μm, the thickness of the cantilever as 2.0 μm and the length as 460 μm.

7.2.2 Measurements

To validate the theoretical value I set up an experiment to measure the two optical amplifications and their ratio R. Two identical piezostacks (3 mm $\times$ 3 mm $\times$ 3 mm) are mounted so that one can oscillate in a horizontal direction (equivalent to in-plane PFM measurements) and the other so that it can oscillate in a vertical direction (equivalent to out-of-plane PFM measurements). The cantilever is placed on a piece of Si mounted on top or on the side of the piezostack in order to have a hard, defined and stable SiO_2 surface (see Fig. 7.18). With an applied voltage of 0.1 V_{pp} the piezoelements are well within their undistorted small signal ranges, which is necessary as the measurements are done with lock-in amplifiers. At the applied voltage the expansion of the piezostack is in the order of 1 nm. Before conducting the measurement, the current driving the piezoelement is checked to be a linear function of the frequency. The oscillation amplitude is recorded as a function of the commonly used frequencies in PFM measurements (Fig. 7.19). Harnagea et al. have shown the out-of-plane resonance fre-

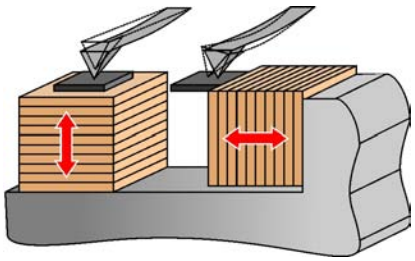

FIGURE 7.18: Setup to measure the out-of-plane (left) and in-plane (right) amplification for PFM measurements. The movement of the piezo-stacks is detected by the deflecting cantilever being positioned on Si glued to the stack.

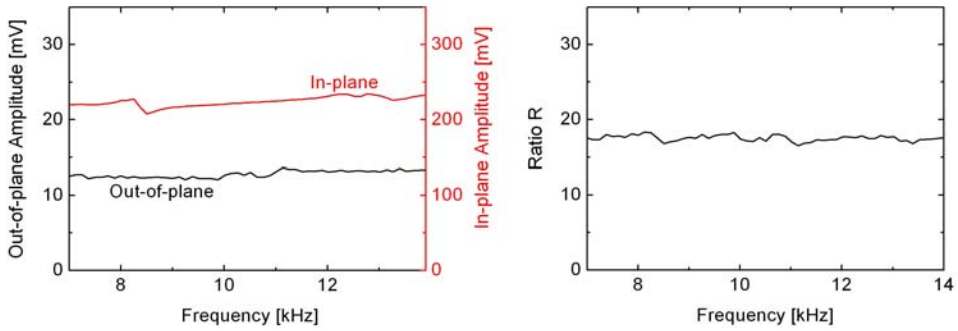

FIGURE 7.19: Measured in-plane and out-of-plane amplitude (left) and the resulting optical amplification ratio R (right).

quency of cantilevers operated in contact mode to be far higher than in non-contact mode [122]. The in-plane resonance frequency is also far higher [123] and both are not within the measured range. The experiment indicates a frequency independent ratio R around 18 which is in line with the value obtained from geometrical considerations. For the calculation I assume that the cantilever completely follows the movement of the piezostack in both cases. In case of a slip the in-plane movement would not be completely transfered to the tip [124] which would lead to a reduced amplification ratio R. Comparison of the obtained values suggest that the influence of the slip can be neglected. These observations are not restricted to PFM, but are valid for other modes of AFM operation where a horizontal and lateral movement of the cantilever is monitored.

In practice the in-plane signal provides a considerably better signal to noise ratio than the out-of-plane response. Subsequently it will be shown that in-plane PFM provides a wealth of additional information that can e.g. be used to identify local heterogeneities of a sample.

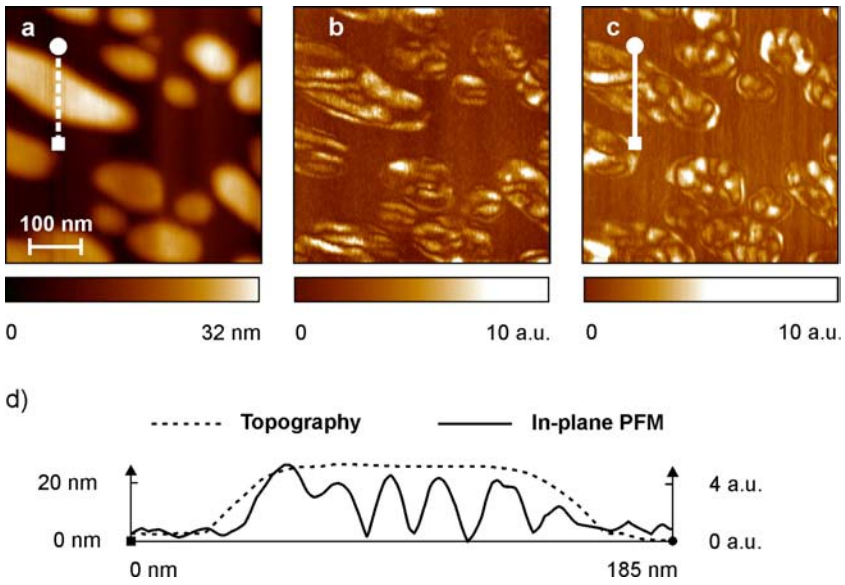

FIGURE 7.20: Topography (part a), out-of-plane piezoresponse (part b), in-plane piezoresponse (part c) of PZT (001) orientated nanograins. Part d shows a profile of the topography and in-plane piezoresponse indicated by the lines in parts a and c. Although the (001) orientated grain is flat within experimental errors, the in-plane piezoresponse varies drastically.

7.3 Contributions to In-plane Piezoresponse on Axially Symmetric Samples

With PFM the piezoelectric properties of ferroelectric materials can be monitored as a vertical and a torsional deformation of an AFM cantilever [16, 19]. These deflections correspond to an out-of-plane and an in-plane deformation of the material under investigation, but *occur only when the tip is in motion*. In other words: any symmetric deformation around the tip that cancels out is impossible to monitor. For example on a thin film with a polarization perpendicular to the surface, no torsional deformation should be monitored. However, a different situation is given in Fig. 7.20 . Here PFM measurements on (001) orientated $Pb(Zr_{0.52},Ti_{0.48})O_3$ (PZT) prepared by chemical solution deposition are shown. On top the single-crystalline nanoislands are flat whereas both the in-plane as well as the out-of-plane piezoresponse are modulated considerably. A possible microscopic origin of these modulations is discussed in [97] where edge-dislocations of the sample-substrate interface are observed by TEM. For the piezoresponse measurements a voltage of 1 V_{pp} at 7 kHz is applied to a PtIr-coated cantilever.

The following considerations are related to the technologically relevant case of a tetragonal sample with the polarization perpendicular to the substrate. This results in a fourfold symmetry

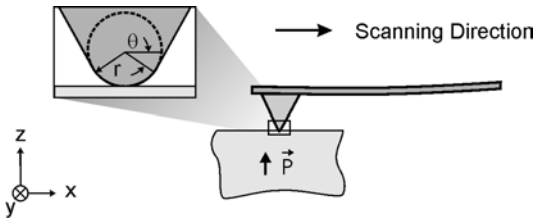

FIGURE 7.21: Illustration of the AFM-tip geometry on a piezoelectric crystal polarized in z-direction including the coordinate system as used in the text.

on the surface. Nonetheless my findings also hold true in a symmetry-reduced system with the polarization vector along other directions that require a more general but less instructive description of the phenomena [26].

I monitor the piezoelectric signal as amplitude and phase of the elastic response to a modulated electrical excitation [21] to obtain information about the piezoelectric tensor elements d_{ijk} and the polarization orientation $\vec{P}$. Ambiguity arises when other than the intrinsic effects contribute to the signal. The x be the direction of the cantilever, y the detectable in-plane deflection z and the vertical direction (see Fig. 7.21). The tip will also experience an in-plane deflection along x and thus cause crosstalk to the out-of-plane signal which is about 20 times less amplified than the in-plane signal [72, 125] (see also section 7.5). I now discuss several scenarios that induce an in-plane tip deflections even though the piezoelectric tensor remains globally homogeneous.

7.3.1 Topography

A major contribution to the in-plane piezoelectric response is given by the topography [47]. Any slope is an imbalance of material around the tip. While on one side the material responds to the field, the tip is free to move in the opposite direction. This causes a clearly visible perimeter enhancement. According to a finite element simulation the increase of the in-plane field E_z and the corresponding coupling to d_{15} for the out-of-plane movement plays a minor role due to the clamping at the interface [47]. Despite a homogeneous piezoelectric tensor, this effect resembles an enhanced piezoelectricity along the perimeter that needs to be carefully separated from strain interaction or etch damage. This effect is discussed in detail in section 7.4.

7.3.2 Tip Asymmetry

Whenever the tip radius varies along the y-direction, the electric field will be highest at the highest tip curvature; the maximum electric field strongly depends on the curvature of the PFM

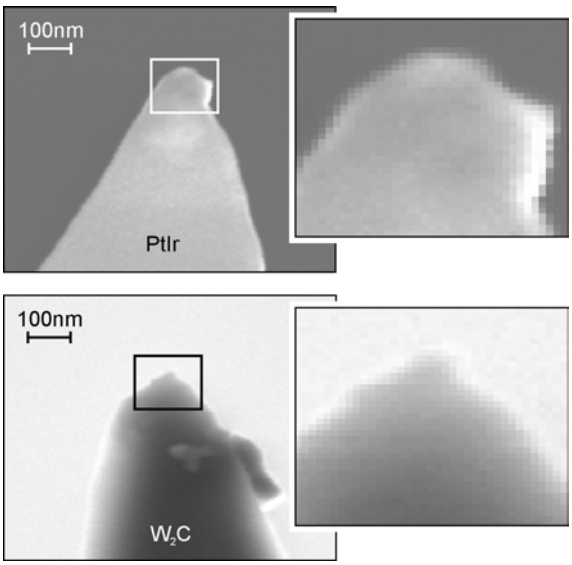

FIGURE 7.22: Scanning electron microscopy images of a used PtIr-coated (top images) and a new W_2C-coated (bottom images) AFM tip. The images show a non-spherical tip symmetry.

probe tip [88]. For the typically utilized tips this radius is about 25 nm but not necessarily over the full range of the radial angle θ as depicted in the scanning electron microscopy images of a PtIr and a W_2C coated tip in Fig. 7.22. In a worst-case scenario this also includes the possibility of a complete loss of metal coating of the tip. To assure a reasonably round apex it is worthwhile scanning a reference structure. This structure needs to have sharp features to scan the tip but should be sufficiently soft not to scratch off the metal coating of the tip. Finite element simulations of PFM measurements with an asymmetric tip are given in Fig. 7.23. As a piezoelectric, a 200 nm wide, 24 nm thick BTO thin film with dielectric constants ε_{11} = 1500 and ε_{33} = 75 [126] has been used. Part a shows the potential distribution if a voltage of -1 V is applied to the cantilever, part b illustrates the in-plane piezoresponse of a symmetric and part c the in-plane response of an asymmetric tip. In case of the symmetric tip the material deformation around the tip cancels out. A high piezoresponse can be seen in the case of a tip with an approximated radius of 16 nm on the right and 24 nm on the left. However, as this signal is omnipresent on flat surfaces, it can be easily identified as a background.

7.3.3 Local Variation of Material Parameters

All samples, including single crystals, are imperfect to a certain degree. Local variations in stoichiometry, mechanical properties or the dielectric constant cannot be ruled out completely.

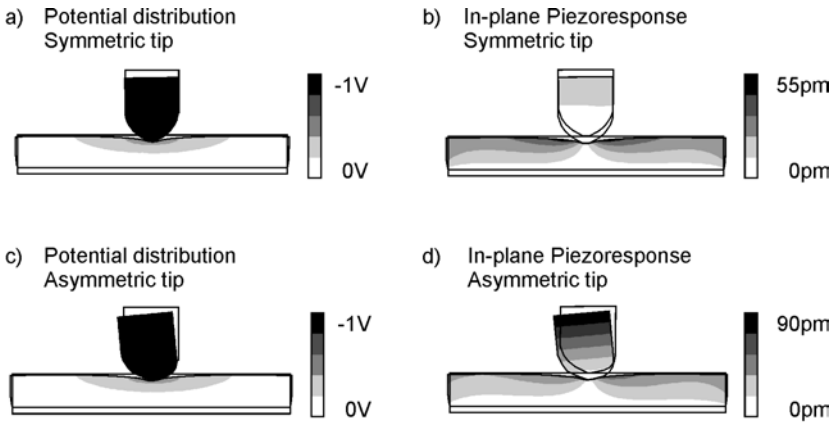

FIGURE 7.23: Simulation of the influence of different tip-radii on the in-plane piezoresponse of a symmetric BTO single crystal. Part a (symmetrical tip) and c (asymmetrical tip) show the potential distribution, part b the in-plane piezoresponse in case of a symmetrical tip and part c the in-plane piezoresponse in case of an asymmetrical tip. The piezoelectric deformation has been exaggerated to guide the eye.

For the following considerations the cause for the symmetry breaking is irrelevant. As an illustration, I discuss a change in the dielectric constant. A section of the setup for the finite element simulation is shown in Fig. 7.24. I simulate a 400 nm wide and 30 nm thick BTO layer contacted by a large electrode on the bottom and a point-like electrode on top. In the middle of the crystal a 3 nm wide plane has been introduced with an ε 10% above the bulk value also resulting in a changed polarization. A voltage of -1 V is applied to the point simulating the cantilever. In the top part of the figure the in-plane piezoresponse is given for the case where the cantilever is at the indicated position. The bottom part of the figure shows the in-plane piezoresponse at the point of contact as a function of the tip position. Depending on the local dielectric permittivity, mechanical constants and the tip radius either rings of in-plane response are created around these spots. Once the needle is in the centre of the varied area the symmetrical situation requires the signal to disappear. Note that due to the tilting of the cantilever in different directions on the two sides of the asymmetry the phase is 180°. Note that the tilting of the cantilever is symmetrical about the center of the asymmetry. This leads to a phase shift of 180° in the in-plane piezoresponse between two points equidistant on either side of the asymmetry.

My simulations (Fig. 7.24) indicate that the range in which the in-plane movement varies is around 1 nm in the presented case. If this drop in the in-plane response can be experimentally resolved depends on the size of the variation and the experimental resolution. The results are a very rough estimate without taking local conductivity into account. The presented inhomogeneity is not restricted to a varying dielectric constant but can also be formed by domain

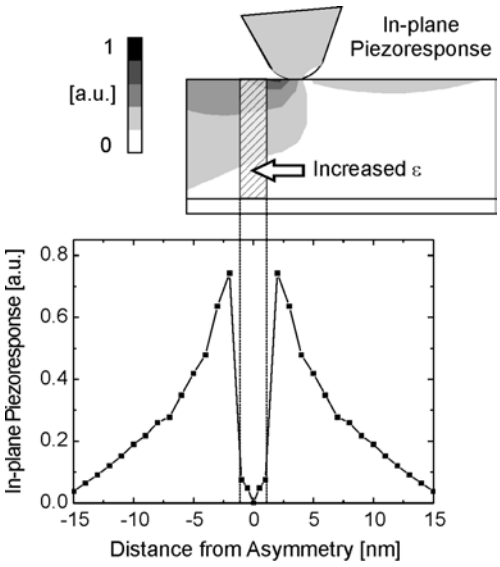

FIGURE 7.24: Simulation of the influence of an increased dielectric constant along z on the in-plane piezoresponse. The top part shows the piezoresponse amplitude distribution at the indicated tip position. In the bottom part the detectable in-plane response depending on the tip-position is depicted.

walls. Scrymgeour et al. have shown in [24] the domain wall influence on the in-plane and out-of-plane piezoresponse and used the measurements to determine an interaction length of the domain wall in ferroelectric $LiNbO_3$. Their amplitude of their in-plane response while scanning over a domain wall corresponds to the simulated response shown in Fig. 7.24.

7.3.4 Additional Contributions

Two other scenarios also reduce the symmetry of the tip and cause a deflection of the tip. Under the assumption of scanning parallel to the symmetry axis of the cantilever, the following effects contribute only along direction x and cannot be detected except for the case of mechanical crosstalk on a slope. The extent of these extra influences is unknown.

1. Bow-wave of surface adsorbates at the tip apex: Surface adsorbates have an immediate influence on quantitative piezoelectric measurements as they considerably reduce the applied field between tip and sample (Section 7.1). As the tip now propagates parallel to the surface it will create a bow wave (see Fig. 7.25) in a viscous adsorbate medium. Effectively, this wave enhances the electrical screening in scanning direction and slightly reduces it on the opposite side. However, this only creates an asymmetry along x where

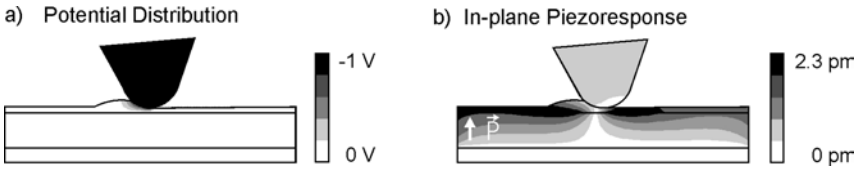

FIGURE 7.25: Simulated potential distribution (a) and in-plane piezoresponse (b) of a BTO single crystal in the presence of a bow wave.

the in-plane response can not be detected. A finite element simulation of this scenario is given in Fig. 7.25. Part a shows the potential distribution in the 12 nm thick BTO film covered by a 2 nm adsorbate layer with a dielectric constant of $\varepsilon = 6$. The rather small in-plane piezoresponse is presented in part b.

2. Space-charge fields: In case a biased needle is moved over a homogeneous semiconductor, the charge carriers will respond with a characteristic time. A quantitative analysis is omitted as the high local fields underneath the tip are probably beyond the small field approximation for Maxwell-relaxation. The resulting space charge field asymmetrically screens the field from the tip in the direction of motion x. As previously pointed out the in-plane sensitivity is along y where this effect does not contribute.

These two scenarios imply a speed dependent asymmetry. In case of the space charges the relaxation time has to be compared to the time the tip remains within the area that directly responds to the field. As for the bow wave nothing is known about the viscosity of these surface adsorbates and their adhesion to the tip.

This list of possible contributions of the experimental setup to the delicate interpretation of piezoelectric data should increase the awareness for the interaction of probe tip and sample.

7.4 Analysis of Shape Effects on the Piezoresponse in Ferroelectric Nanograins with and without Adsorbates

In the previous chapter possible origins of the in-plane piezoresponse on axially symmetrical samples have been discussed. Continuous perovskite thin films were used for the simulations in Fig. 7.11. When dealing with confined structures the additional boundary conditions have to be taken into account as well e.g. the thickness of the material is far less homogeneous in single grains as compared to a thin film. These aspects have a considerable influence on the in-plane piezoresponse, which will be elaborated in this chapter. Instead of only considering the ideal case where the AFM tip is in direct contact with the piezoelectric, I also analyze and

quantify the situation in the presence of adsorbates. The existence of the adsorbate layer and the influence on piezoresponse measurements for single crystals was shown in chapter 7.1. As a result the electric field applied via the tip to the perovskite is overestimated and misleading piezoelectric constants are calculated. This also applies to small grains.

7.4.1 Simulation

To quantify the effect of adsorbates on the electric potential distribution as well as the in-plane and out-of-plane piezoresponse of nanoislands, I modeled a 115 nm high and 300 nm wide BTO grain with ANSYS. An anisotropic dielectric permittivity of ε_{11} = 1500 and ε_{33} = 75 [46] ($\tan\delta = 0$) and the following piezoelectric constants are used [46]:

d_{33} = 85.6 pm/V
d_{31} = d_{32} = -34.5 pm/V
d_{15} = d_{24} = 392 pm/V

The d_{ij} coefficients (unit m/V = C/N) describe the mechanical strain produced by an electrical field. An equivalent piezoelectric equation system can be set up with the e_{ij} coefficients (unit C/m^2 = N/Vm) which correlate the mechanical strain with the applied charge density (see section 3). As ANSYS requires the e_{ij} coefficients, the following values have been calculated:

e_{33} = 13.67 pC/m^2
e_{31} = e_{32} = -9.01 pC/m^2
e_{15} = e_{24} = 21.17 pC/m^2

I simulate a c-axis oriented sample i.e. a polarization perpendicular to the bottom electrode.

In this model both the bottom electrode and the cantilever are made of Pt. The round tip with a diameter of 40 nm is approximated by a polygon, and the insulating adsorbate layer is modeled with a constant vertical thickness of 2 nm and $\varepsilon = 6$ [114]. A constant voltage of -1 V is applied to the cantilever. I only model a cross section of BTO which is possible without loss of generality due to the tetragonal symmetry (4mm). These 2D finite element simulation results are given in Fig. 7.26a-f. On the left (a, c and e) I show the case without an adsorbate layer, while the right parts (b, d and f) are calculated with an adsorbate layer. These images illustrate the steady state after the potential has been applied. A drastic influence of the adsorbates is visible in the potential distribution (parts a and b). In the case of direct contact between the tip and BTO, the voltage drops over large parts of the grain. Due to the curvature of the tip, the voltage drop is highest directly underneath the tip [88]. In Fig. 7.26b the potential drops almost completely across the adsorbate layer so that the actual voltage applied to the grain is about one order of magnitude less than the voltage applied to the tip. This effect of an

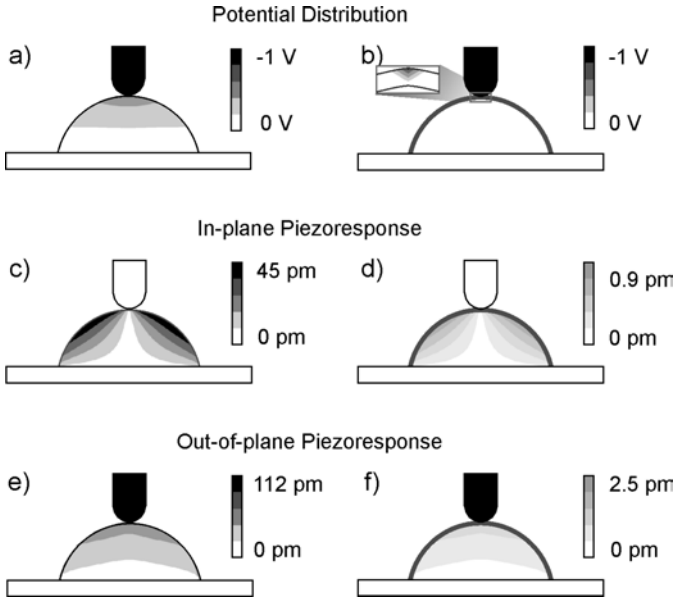

FIGURE 7.26: Simulation of the potential distribution (a and b), the in-plane piezoresponse (c and d) and the out-of-plane piezoresponse (e and f) for an adsorbate free nanograin (left) as well as for an adsorbate covered nanograin (right). The BTO nanograins are 300 nm wide and 115 nm high, the adsorbate layer 2 nm thick.

increasing thickness-fraction of adsorbates on the field applied to the sample becomes evident in Fig. 7.28: The out of plane signal with adsorbates follows the topography. Let the applied voltage be U, the voltage across the adsorbates U_a and the voltage across the piezoelectric U_p. The capacitance of the adsorbate is denoted by $C_a = \varepsilon_0 \varepsilon_a A/d_a$, the capacitance of the piezoelectric as $C_p = \varepsilon_0 \varepsilon_p A/d_p$. Under the assumption of equal areas, the ratio of the voltages is:

$$\frac{U_p}{U_a} = \frac{\varepsilon_0 \varepsilon_a \frac{A}{d_a}}{\varepsilon_0 \varepsilon_p \frac{A}{d_p}} = \frac{\varepsilon_a d_p}{\varepsilon_p d_a}.$$

The applied voltage U is the sum of the U_a and U_p:

$$U = U_a + U_p = U_p \left(1 + \frac{\varepsilon_p d_a}{\varepsilon_a d_p}\right)$$

$$U_p = U \left(\frac{1}{1 + \frac{\varepsilon_p d_a}{\varepsilon_a d_p}}\right)$$

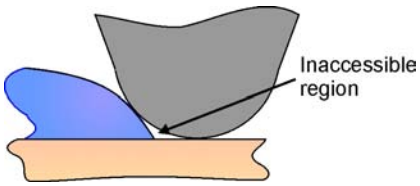

FIGURE 7.27: AFM tip at the perimeter of a nanograin. Note the inaccessible area due to the finite tip radius.

Using the values of the simulation ($\varepsilon_p = 75$, $\varepsilon_a = 6$, $d_a = 2$ nm) the voltage over the piezoelectric is the following function of the thickness:

$$U_p \approx U \frac{1}{1 + \frac{25\ \mathrm{nm}}{d_p}} \tag{7.5}$$

In a first approximation the voltage over the piezoelectric follows the topography. The electric field at the piezoelectric is given by

$$E_p = \frac{U_p}{d_p} \approx U \frac{1}{d_p + 25\ \mathrm{nm}}.$$

When the AFM tip moves over a grain the question arises if the applied electric field at the perimeter of the grain exceeds the coercive field. For a negligible thickness d_p the maximum electric field E_p for the case of $U = 1$ V is $E_{pmax} \approx 4 \times 10^7$ V/m. Due to the finite tip radius r, the minimum contactable thickness of the crystal is in the order r (see Fig. 7.27). This results in an electric field of $E_{pmax} \approx 2 \times 10^7$ V/m. As this is less than the coercive field E_C for a thin ferroelectric (see the Kay-Dunn law in section 2.4), it can be assumed that no ferroelectric switching occurs.

For a constant voltage the electric field is inversely proportional to the thickness of the grain. Therefore the electric field at the perimeter may become sufficiently large to cause significant non-linearities [127]. Depending on the radius of the tip and the form of the grain, this region may even be inaccessible to measurements.

In the in-plane piezoresponse (parts c and d of Fig. 7.26) as well as the out-of-plane piezoresponse (parts e and f) the maximum contraction is nearly two orders of magnitude smaller than in case of a clean surface. As the piezoresponse is directly proportional to the applied voltage, this confirms the expectation that the piezoresponse decreases dramatically in the case of present adsorbates. Figure 7.26c and d indicate that the in-plane response is effectively zero on a flat (001) surface. This finding becomes clear if we recall the signal detection process. The setup is only sensitive to the deflection of the beam reflected from the cantilever i.e. all we

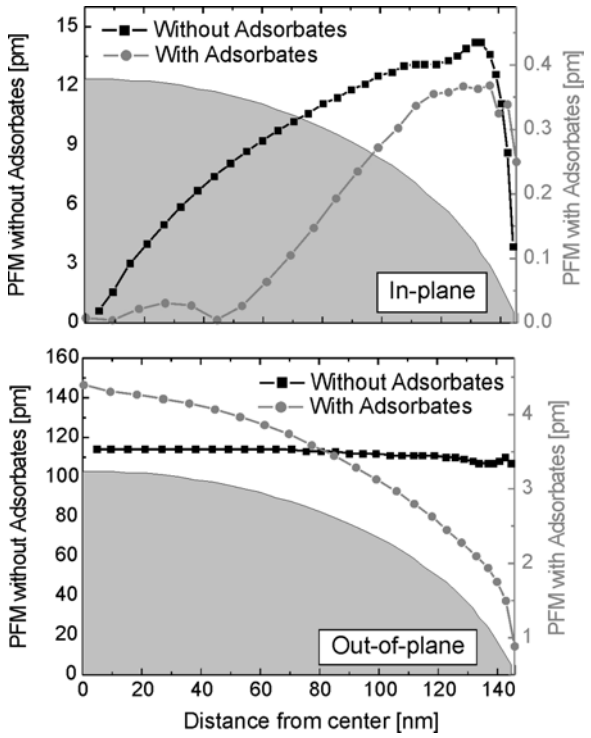

FIGURE 7.28: Simulated in-plane and out-of-plane piezoresponse as a function of the distance from the center of the nanograin. In both clean and contaminated surface the in-plane response changes drastically. The out-of-plane activity decreases at the edge in the case with adsorbates due to an increasing thickness fraction of the adsorbates leading to a reduced voltage applied to the BTO (Eq. 7.5). The shaded regions show the cross section of the topography of the modeled nanograin and the lines connecting the simulated points are a guide to the eye.

see is a somehow moving tip. In many cases this movement cancels out for symmetry reasons. This is exactly the case for the in-plane response on a flat surface of a (001) oriented sample with 4mm symmetry.

In a subsequent simulation the tip is moved off-center whereby it is modeled as a point contact. The results are given in Fig. 7.28. An in-plane signal cannot be detected in a symmetric arrangement (as can also be seen in Fig. 7.26c and d where the in-plane response is 0 on the flat part of the grain). The increase of the in-plane signal close to the perimeter is due to the broken radial symmetry underneath the tip. Note that for tetragonal symmetry no shearing is related with fields along the polar axis. In the presence of the adsorbate layer the in-plane piezoresponse near the edge is smaller compared to the case of a clean surface. The out-of-plane response without adsorbates is essentially thickness-independent as the increasing field is can-

celed out by the decreasing amount of expanding material. In the presence of adsorbates the out-of-plane response is dominated by the steadily growing thickness-fraction of the adsorbates as the perimeter is approached.

The variation of the out-of-plane response is a result of the asymmetric mesh used in the simulation. In the used mesh shown in Fig. 3.1 most elements are normal quadrilaterals. Due to the curved surface however, some of the quadrilaterals are deformed and can be nearly regarded as triangles. As the form of the elements has a considerable influence on structural analyses, this results in the mentioned out-of-plane variations as well as in a small in-plane uncertainty.

7.4.2 Measurement

Measuring these effects (constant piezoresponse in the out-of-plane direction and enhancement in the in-plane direction) is challenging as the polarization of the ferroelectric material needs to be uniform in the direction perpendicular to the substrate. Fig. 7.29 shows the topography and piezoresponse of a BTO grain prepared by pulsed laser deposition on a SRO (50nm) covered (100) STO single crystal. The original out-of-plane PFM data shows a background piezoresponse signal that is removed in Fig. 7.29c to provide zero response for the electrode. According to [128] and [22] this offset is a measuring artifact due to an electrostatic interaction between the cantilever and the electrode. While the out-of-plane response (c) is rather constant over the grain a pronounced enhancement is visible along the perimeter for the in-plane signal (d). Note the absence of an in-plane response at the very left and right end of the grain.

Consider the cantilever moving parallel to its symmetry axis along the x-direction (Fig. 7.30). Lateral torsion of the cantilever as a consequence of an in-plane motion can only occur perpendicular to this direction i.e. in y-direction. In this sense the two cases (A-B, C-D) illustrated in Fig.7.30a are different in their symmetry. Figure 7.30b shows the cantilever between two equivalent points A and B and the applied field will only cause a movement in -x–direction, a signal that cannot be detected as a lateral torsion. In contrast Fig.7.30c depicts the situation of the cantilever being shifted sideways as the grain expands and contracts. The difference between the positions C and D is a 180° phase shift of the in-plane signal, also experimentally confirmed. In this respect the correlation between the topography and in-plane signal can be approximated as the derivative along the direction perpendicular to the cantilever symmetry axis. Direct comparison between the derivative along the y-direction and the in-plane piezoelectric response for a ferroelectric BTO grain as illustrated in Figs. 7.29a, b shows excellent agreement. Note that in both cases the perimeter enhancement cannot be detected on the complete circumference.

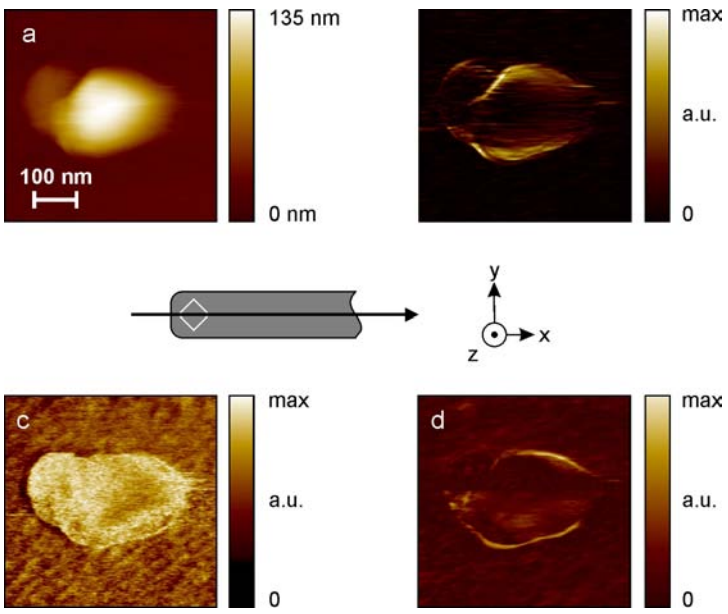

FIGURE 7.29: a) Topography (500nm $\times$ 500nm), b) absolute value of the derivative of the topography in y-direction, c) amplitude of the out-of-plane piezoresponse and d) in-plane piezoresponse of a BTO grain. The out-of-plane response is relatively constant over the total grain whereas the in-plane response is very small in the middle and high at the perimeter. Note also the correspondence between the derivative of the topography and the in-plane response.

7.4.3 Analysis

To sketch the physics of the converse piezoeffect of the tetragonal c-axis orientat system (most situations will be more complex), the applied electric field as well as the piezoelectric coefficients in all directions have to be taken into account. In order to adhere to the indexing conventions of the piezoelectric coefficients, the directions in this chapter are referred to as 1, 2 and 3 instead of x, y and z respectively. Fig. 7.31 depicts the electric field for the case of a voltage applied to point A and B. The components of the electrical field distribution in direction 1 are different for the two points (i.e. component in direction 1 of E_A and E_B). As a consequence $\vec{E}$ and $\vec{P}$ are no longer parallel and shear deformation (d_{15}) occurs.

For constant temperature and without additional mechanical stress the strain tensor S_{jk} is given as [31]

$$S_{jk} = d_{ijk}E_i.$$

For crystals like BTO with 4mm symmetry the piezoelectric tensor d_{ijk} can be written in the

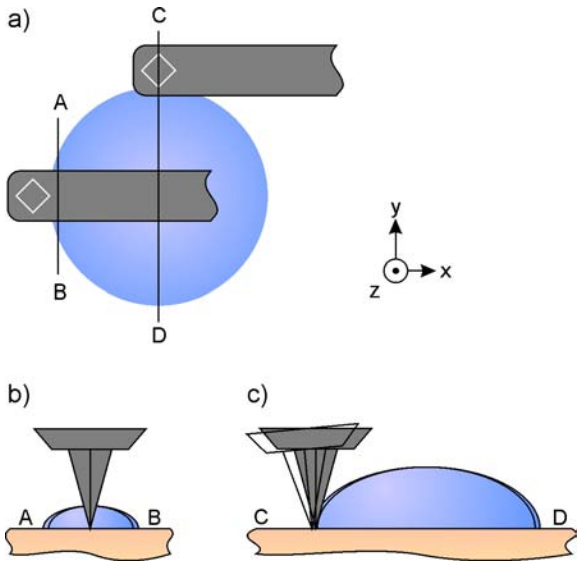

FIGURE 7.30: a) Top view of the cantilever-grain system for two different positions at the grain perimeter, b) side view along the x-direction for the tip in front of the grain and c) at a side of the grain, the first case with in-plane symmetry, the latter without.

Voigt notation as

$$d_{ij} = \begin{pmatrix} 0 & 0 & 0 & 0 & d_{15} & 0 \\ 0 & 0 & 0 & d_{24} & 0 & 0 \\ d_{31} & d_{32} & d_{33} & 0 & 0 & 0 \end{pmatrix} \quad \text{with} \quad \begin{matrix} d_{31} = d_{32} \\ d_{15} = d_{24} \end{matrix} .$$

Considering the field distribution the elements of the strain tensor are:

$$\begin{aligned} S_{11} &= d_{311}E_3 \\ S_{22} &= d_{322}E_3 \\ S_{33} &= d_{333}E_3 \\ S_{13} &= d_{113}E_1 = \epsilon_{31} = d_{131}E_1 \\ S_{23} &= d_{223}E_2 = \epsilon_{32} = d_{232}E_2 \end{aligned}$$

The PFM setup is sensitive to a contraction or expansion of the piezoelectric material. This length change is dependent on the strain tensor and on the distance from the origin. Here these changes are given as [47]:

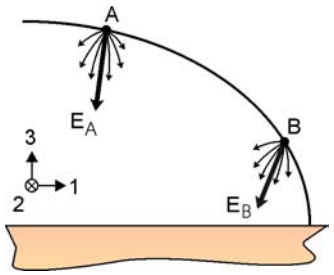

FIGURE 7.31: Electric field magnitude and direction at points A and B where a voltage is applied. Note the difference of the component in direction 1 between E_A and E_B.

$$
\begin{aligned}
\Delta\ell_1 &= \epsilon_{11}\ell_1 + \epsilon_{13}\ell_3 \\
&= d_{311}E_3\ell_1 + d_{113}E_1\ell_3 \\
&= d_{31}E_3\ell_1 + d_{15}E_1\ell_3 \\
\Delta\ell_2 &= \epsilon_{22}\ell_2 + \epsilon_{23}\ell_3 \\
&= d_{322}E_3\ell_2 + d_{223}E_2\ell_3 \\
&= d_{32}E_3\ell_2 + d_{24}E_2\ell_3 \\
\Delta\ell_3 &= \epsilon_{31}\ell_1 + \epsilon_{32}\ell_2 + \epsilon_{33}\ell_3 \\
&= d_{131}E_1\ell_1 + d_{232}E_2\ell_2 + d_{333}E_3\ell_3 \\
&= d_{15}E_1\ell_1 + d_{24}E_2\ell_2 + d_{33}E_3\ell_3
\end{aligned}
$$

The equations show that even in single crystalline material the out-of-plane piezoresponse is a function of the electric field in *all three* directions and that the in-plane response is a function of the electric field in directions 1 and 3 or in directions 2 and 3.

7.5 Mechanical Crosstalk

In chapter 7.4 I have shown the influence of the grain topography on in-plane piezoresponse measurements that essentially gives rise to an enhancement of the in-plane piezoelectric response along the perimeter. However, this enhancement is more pronounced in the direction perpendicular to the cantilever axis (usually identical with the scanning direction). As an in-plane movement of the cantilever tip *parallel* to the cantilever axis causes a vertical bending or vertical torsion (Fig. 5.4) instead of a lateral torsion, the respective signal is monitored in the channel for out-of-plane movements. The optical amplification of the vertical channel can be

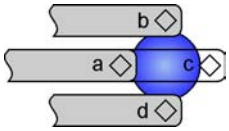

FIGURE 7.32: Top-view of the cantilever and the grain indicating the different positions of the cantilever at the grain.

up to a factor of 25 below that of the lateral channel for commercially available cantilever used in this work (450 μm long, tip height 15 μm), therefore this crosstalk is hard to detect.

7.5.1 Analysis

According to Eq. 5.3 the vertical torsion and the vertical bending cannot be detected independently, and due to the symmetry of the cantilever the in-plane piezoresponse can only be detected on the grain slopes parallel to the cantilever axis. In Fig. 7.32 these are positions b and d. Part a of Fig. 7.33 shows a deformation of the grain in y-direction. The cantilever is laterally twisted, resulting in a movement of the laser on the photo diode in the lateral direction. This is the normal case for in-plane PFM. The mechanical crosstalk can be seen in Fig. 7.33b. In the sketch I only consider the deformation in x-direction. Although this clearly is an in-plane deformation, due to the geometry of the cantilever, it leads to a out-of-plane movement of the cantilever. This movement is detected as a vertical displacement of the laser on the photo diode. An $out\text{-}of\text{-}plane$ response is recorded, even though its physical origin is $in\text{-}plane$.

7.5.2 Measurement

The question arises if this extrinsic piezoelectric effect is sufficiently pronounced to be experimentally detected. I analyze this on a (001) orientated BTO grain prepared by pulsed laser

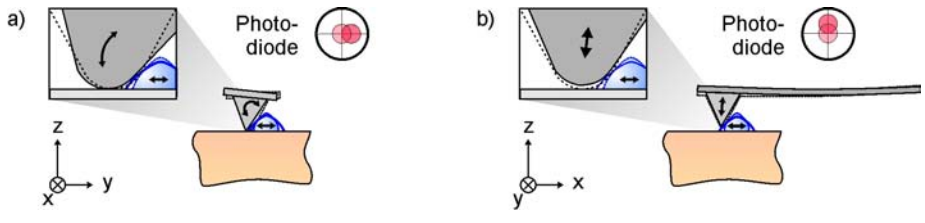

FIGURE 7.33: a) Analysis of the cantilever movement for an expansion of the grain in direction y and b) analysis of the cantilever movement for an expansion of the grain in direction x resulting in mechanical crosstalk.

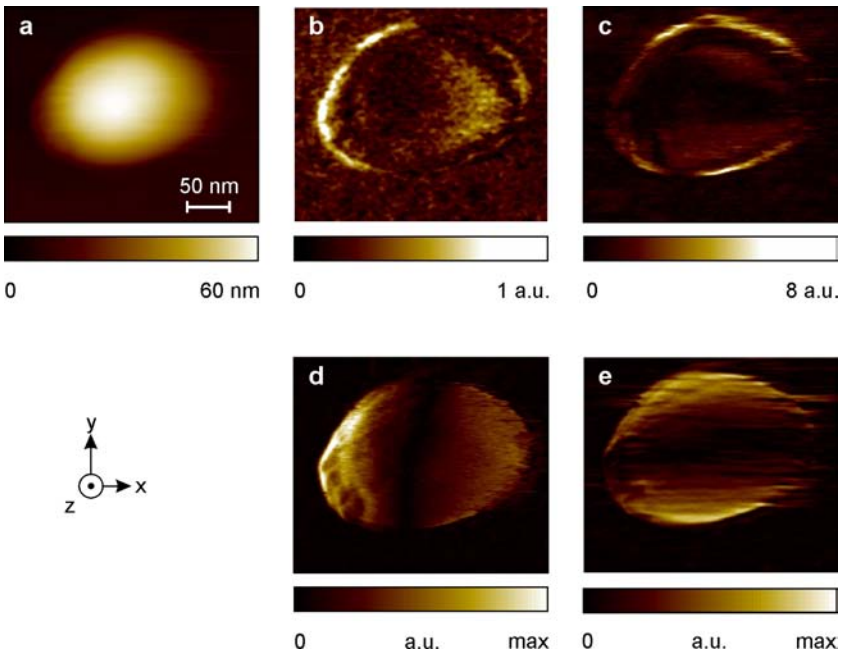

FIGURE 7.34: a) Topography, b) out-of-plane piezoresponse amplitude, c) in-plane piezoresponse amplitude, d) absolute value of the derivative of the topography in x-direction and e) absolute value of the derivative of the topography in y-direction. In the out-of-plane case the amplitude maximum is on the left and right of the grain whereas in the in-plane case it is on the top and the bottom. Note the similarities between the out-of-plane response and the derivative in x-direction as well as the in-plane response and the derivative in y-direction.

deposition on a SRO (50nm) covered (100) STO single crystal. A voltage of U = 5 V at 7 kHz is applied to a PtIr coated cantilever ("ContPt" from Nanosensors, f_0=13 kHz).

Figure 7.34 shows the topography as well as the in-plane and out-of-plane piezoresponse of this sample. The situation described in the previous section can be clearly identified: for the in-plane PFM scan (part c) the maximum amplitude is at positions b and d with practically no response at positions a and c. In the out-of-plane response (Fig. 7.34b) a significant response can only be seen in positions a and c which is the crosstalk from the in-plane response. Figure 7.34d and e show the absolute value of the derivative of the topography in y and x direction respectively. The out-of-plane response is strikingly similar to the derivative in x direction. This scenario is described in chapter 7.4. As the out-of-plane response originates from an in-plane crosstalk, it comes as no surprise that it is similar to the topography derivative in x-direction.

Two different physical effects can be the cause of this crosstalk. In the first case depicted in Fig.

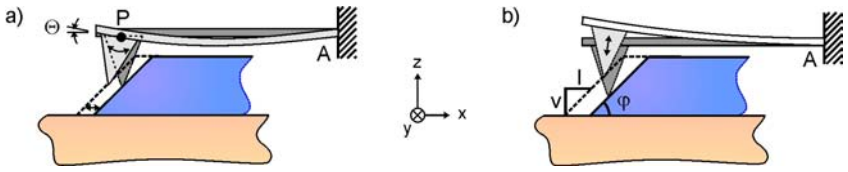

FIGURE 7.35: Two different situations resulting in a mechanical crosstalk. a) The cantilever tip 'sticks' to the grain and has to be stretched when the grain expands. This results in a tilting of the tip (angle Θ). b) The tip slips over the grain and an expansion of the grain leads to a lifting of the tip. The measured values prove that the second case is the dominating one. The images are not drawn to scale.

7.35a, the cantilever tip 'sticks' to the grain. When the grain expands along $-x$, the cantilever has to be vertically stretched, resulting in a tilting of the tip i.e. a detectable $out\text{-}of\text{-}plane$ signal. Taking the dimensions of the setup (cantilever length 450 μm, expansion of the grain a few pm) into account, I assume that the center of the tip (point P in Fig. 7.35a) remains stationary. As this situation is geometrically equivalent to the in-plane response [72], the ratio

$$R = \frac{\text{in-plane amplitude}}{\text{out-of-plane amplitude}}$$

should be almost unity and not differ by nearly one order of magnitude as observed. In the second scenario (Fig. 7.35b) the tip slips over the grain. An expansion of the grain along $-x$ thus leads to a lifting of the tip and cantilever. Here I expect the ratio of the amplifications to be R=18 [129]. The slope of the grain modifies this consideration as it translates the in-plane expansion into a vertical deflection of the cantilever. In Fig. 7.35b I observe a maximum inclination angle of 65° at position a of the grain (cf. Fig. 7.34a). According to

$$\frac{\text{out-of-plane deflection}}{\text{in-plane expansion}} = \frac{v}{l} = \tan\varphi \tag{7.6}$$

that provides an additional factor of 0.47 to the ratio R, i.e. $R' = 18/\tan 65° \approx 8.4$. This is within a 5% experimental error of the observed value. From this quantitative agreement I deduce slip as depicted in Fig. 7.35b to be the appropriate description. An explanation why an in-plane signal can at all be detected despite a (001) orientation is given in [47] and [129]. The crosstalk has a tremendous relevance for the investigation of size effects in ferroelectric nanostructures as the observed additional out-of-plane deflection of the laser beam is not caused by a modified polarization. According to [130], d_{33} (causing the out-of-plane expansion) is directly proportional to the polarization (in samples with a cubic paraelectric phase which is true for BTO). In that sense my experiment confirms that no intrinsic size effect has so far been observed due to lateral scaling in ferroelectric nanostructures.

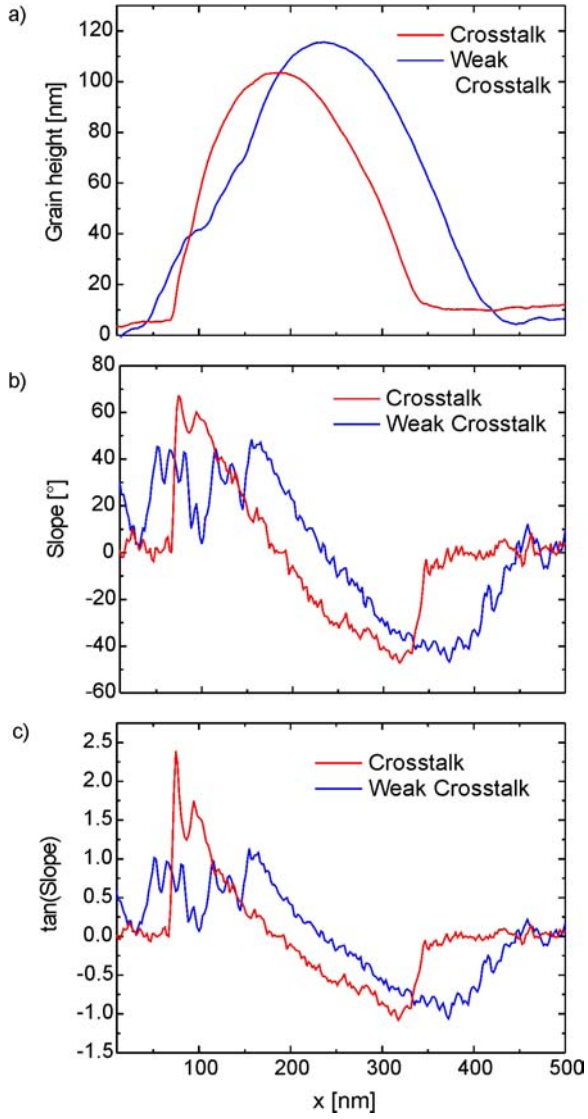

FIGURE 7.36: a) Cross section of the Topography, b) the corresponding slope and c) tan(slope) of the grain shown in Fig. 7.29 (labeled Weak Crosstalk) and Fig. 7.34 (labeled Crosstalk). Although the topography looks quite similar for the two grains, the difference of the influence on the crosstalk is a factor of 2.5 as tan(slope) is the decisive parameter.

The in-plane piezoresponse of the measurements shown in Fig. 7.29 and Fig. 7.34 is comparable. Why is the out-of-plane response that different, especially considering the fact that the measurements were taken on the same sample? In the first case the out-of-plane response is relative constant over the grain, in the second case a substantial crosstalk can be seen. I have shown, that the crosstalk depends on the slope of the grain (Eq. 7.6). A cross section through the center of the two grains and the corresponding slopes is given in Fig. 7.36. Although the grain look quite similar, the maximum slope on the left side of the grain is 45° and 65° respectively. For the presented mechanism the tangent of the slope and not the slope itself is the crucial factor. For the two measurements this difference is a factor a 2.5. This means that crosstalk in the out-of-plane image from the in-plane movement is 2.5 times stronger in the second case compared to the first case. As a result, in the first case very little crosstalk can be seen whereas in the second case it is pronounced. In this chapter I have shown the existence of mechanical crosstalk between in-plane and out-of-plane PFM. This crosstalk is inherent to the scanning method and occurs in addition to the misalignment crosstalk of the AFM photo detector. Measurements show that this effect can be substantial when analyzing piezoelectric grains.

I conclude that the observed perimeter enhancements of the in- and out-of-plane signal for c-axis oriented grains is an inevitable geometrical consequence of the setup and not due to an enhancement of the piezoelectric tensor element d_{33}.

7.6 System Crosstalk

In most modern atomic force microscopes (AFM) the laser beam reflected from the top of the cantilever is detected by a four quadrant photo diode. If the cantilever bends up or down, the reflected beam will be deflected up or down as dicussed in section 5.1.1. Torsion of the cantilever deflects the laser to the left or the right. A problem of this set-up occurs if the photo diode is rotated with respect to the cantilever-plane. As a result, a lateral motion of the laser spot will cause the out-of-plane signal to change [131]. If the photo diode can not be rotated or other system modifications are undertaken to eliminate the effect [132, 133], this crosstalk is present in all types of measurements with lateral sensitivity [134].

The principle of the crosstalk is shown in Fig. 7.37. For an ideally aligned system a movement of the cantilever in z-direction is detected as Δz with $\Delta x = 0$ (left case). However, if the photo diode is rotated an angle of φ relative to the reflective side of the cantilever (right image), a movement of the cantilever in z-direction is detected as $\Delta z'$ with $\Delta y' \neq 0$.

As the optical amplification for the cantilevers used within this work is approximately a factor of 18 larger for the lateral than for the vertical direction (section 7.2), the influence of the

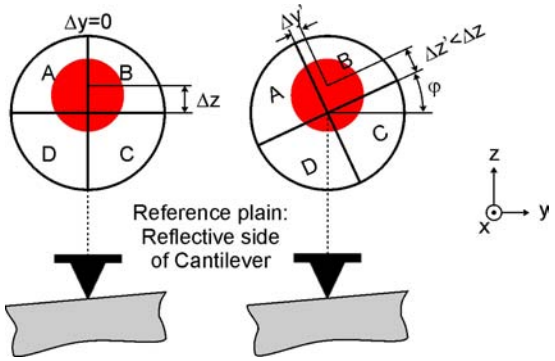

FIGURE 7.37: System crosstalk resulting from a misaligned photo diode. In the left case a movement of the cantilever in z-direction is detected as Δz with $\Delta y = 0$. If the photo diode is rotated by an angle of φ relative to the reflective side of the cantilever (right image), a movement of the cantilever in z-direction is detected as $\Delta z'$ with $\Delta y' \neq 0$.

crosstalk can be substantial, even if the photo diode is only marginally rotated.

For a misalignment of the photo diode of $\arcsin \frac{1}{20} = 2.87°$ a lateral cantilever movement will result in an equal response in the in-plane as well as out-of-plane directions. This results in the in-plane and out-of-plane PFM measurements being equal, which has already been experimentally observed [135]. This renders the discussion of the vertical piezoresponse highly ambiguous.

This situation may also lead to another problem: The feedback-loop of the AFM regulates the z-piezo, so that the pressure on the cantilever is constant. Any movement of the sample relative to the tip in z-direction must be controlled. If a lateral signal is superposed on the vertical deflection due to crosstalk, the feedback is not regulated solely according to the varying height any more. This does not only lead to wrong in-plane or out-of-plane measurements, even the topography can can be distorted. This does not apply to PFM as the external excitation frequency is substantially larger than the frequency of the feedback-loop. However it has to be considered in most tribology measurements.

To overcome this problem measures for compensation have to be introduced, e.g. mounting the cantilever so that it can be rotated. After every cantilever change, the system has to be calibrated. This can be done by exciting the z-piezo scanner and thereby rotating the photo diode so that the lateral signal becomes zero [136]. Thereby the ideal situation for which all the aforementioned considerations (section 7.2, 7.3, and 7.4) apply is restored.

8 Summary

The major aim of this work has been to identify and quantify extrinsic influences on the piezoresponse measurements of ferroelectric nanograins. The following paragraphs summarize the main results.

- **Multichannel measurements**
  Most conventional PFM setups do not allow for a rotation of the sample around the tip contact and are therefore only capable of a partial reconstruction of the strain tensor. Even this partial reconstruction requires the knowledge of both amplitude and phase of the in- and out-of-plane piezoresponse. A simultaneous detection of these four signals overcomes previous limitations due to thermal drift and sample modification during the scanning process. The higher bandwidth of most lock-in amplifiers for the real and imaginary signal processing should readily be sacrificed for the sake of a physically meaningful amplitude and phase presentation. A numerical post-measurement conversion is unfavorable as the noise levels of both measured channels add up. In any case the signal range should be displayed by a color bar.

- **Influence of adsorbates on PFM**
  XPS and PFM measurements have confirmed that perovskite ferroelectrics are covered by adsorbates under ambient conditions. In PFM this leads to a severe reduction of the electric field applied to the sample and attenuates the piezoresponse on average by 250%. Heat treatment in high vacuum has been successfully employed to lessen the amount and impact of adsorbates and to substantially recover the piezoresponse. The additional experimental effort is justified by the superior reliability and the enhanced measurement resolution [86, 107, 137].

- **Direction-dependent optical amplification**
  Due to the cantilever geometry the optical amplification for the in-plane response is larger than for the out-of-plane response in our AFM configuration. As a result, the in-plane measurements on ferroelectric nanostructures usually show substantially more detail and less noise. The geometrically predicted amplification ratio of about 20 for our standard cantilever has been experimentally confirmed [72].

- **Piezoresponse on axially symmetrical samples**
  The large optical amplification makes the in-plane piezoresponse measurements highly attractive. However, in c-axis oriented thin films no in-plane piezoresponse should be detected at all due to the radial potential distribution underneath the tip. Measurements and simulations have been presented showing that an in-plane response can be detected

whenever the radial symmetry is broken. Without need for an in-plane projection of the polarization this can be due to an asymmetric cantilever, local variations of material parameters or an uneven surface [138].

- **Topography-induced piezoresponse**
  Especially on the slopes of ferroelectric nanoislands, the topography has a significant influence on the in-plane PFM signal. As a result of the broken symmetry of the radial potential distribution and the unbalanced amount of material underneath the AFM tip a significant enhancement of the in-plane response occurs at the perimeter even of c-axis oriented grains. Due to the cantilever geometry, this enhancement is restricted to slopes of the grain parallel to the axis of the cantilever. However, the enhancement may also be observed on the slopes perpendicular to the cantilever-axis in out-of-plane measurements as a result of a mechanical crosstalk. A detailed analysis of our measurements revealed slip on the slope of a nanograin as the origin of this crosstalk [47, 129, 139].

- **System crosstalk**
  Another kind of crosstalk originates from a misalignment of the cantilever with respect to the four sector photo diode. In this case the pronounced in-plane response supersedes the out-of-plane signal and in some lateral force microscopy configurations this may even result in the in-plane signal impacting the z-feedback-loop of the AFM. Taking the high in-plane optical amplification into account, a misalignment of only 3° results in two equally large in-plane contributions in both channels. I have suggested a novel mechanical compensation scheme to eliminate this crosstalk [136].

In the quest for the ferroelectric limit PFM does not provide a straightforward approach. This work has identified and quantified several extrinsic contributions to the piezoresponse signal from ferroelectric nanostructures and thus paves the way for a more quantitative understanding of piezoresponse imaging and new techniques to monitor local heterogeneities emerge.

9 Outlook

PFM is a well established method to analyze ferroelectric materials. However, the present study indicates that several new aspects of PFM have to be considered in order to avoid misinterpretations. Extrinsic effects from PFM need to be carefully identified and independent investigations (such as independent measurement of ε) have to complement future studies.

Future studies should focus on obtaining a more quantitative understanding of piezoresponse data. A prerequisite is therefore to calibrate the system after each modification. Measurements under UHV open the door to the real physical properties of nanosized ferroelectrics. When heating the samples under UHV conditions caution has to be exercised not to chemically reduce them.

The radial potential distribution underneath the AFM tip should be analyzed in more detail. This will provide valuable insight into the penetration depth of the method that can possibly be made use of.

Furthermore it will be interesting to combine PFM with local conductivity measurements. Xiao et al. have recently shown [34] a possible charge accumulation at 90° domain walls in contrast to 180° domain walls where no charges accrue. If these charges exist, they should blurr the lateral resolution of PFM at domain walls. A complementary question is if these domain walls can be detected by conductivity measurements.

The chemical composition and the homogeniety of nanograins are still a subject of debate. Combining PFM with a chemically sensitive analysis method could provide valuable information about the ferroelectric properties on the nanoscale. Possible methods are Kelvin Probe Microscopy and Tip-Enhanced Raman Spectroscopy in conjunction with PFM and complemented by Transmission Electron Microscopy. To really image the ferroelectric and not the adsorbates, these measurements should be conducted in UHV.

In order to get a better insight into the size induced ferroelectric phase transition the temperature is an interesting parameter to vary. Data on the ferroelectric phase transition in individual nanoislands as a function of size will be a cross-check for predictions from both phenomenological and first-principle theory.

References

[1] S. B. Lang, Pyroelectricity: From ancient curiosity to modern imaging tool, *Physics Today* **58**, 31 (2005)

[2] S. B. Lang, The history of Pyroelectricity: from Ancient Greece to Space Missions, *Ferroelectrics* **230**, 99 (1999)

[3] J. Valasek, Piezo-Electric and Allied Phenomena in Rochelle Salt, *Physical Review* **17**, 475 (1921)

[4] J. G. Schmidt, *Curiöse Speculationes bey Schlaflosen Nächten* (1707)

[5] G. H. Haertling, Ferroelectric Ceramics: History and Technology, *Journal of the American Ceramic Society* **82**, 797–818 (1999)

[6] T. Woike, W. Kirchner, G. Schetter, T. Barthel, K. Hyungsang, and S. Haussuhl, New Information-Storage Elements on the basis of Metastable Electronic States, *Optics Communications* **106**, 6 (1994)

[7] O. Auciello, J. F. Scott, and R. Ramesh, The physics of ferroelectric memories, *Physics Today* **51**, 22–27 (1998)

[8] S. Buhlmann, B. Dwir, J. Baborowski, and P. Muralt, Size effect in mesoscopic epitaxial ferroelectric structures: Increase of piezoelectric response with decreasing feature size, *Applied Physics Letters* **80**, 3195–3197 (2002)

[9] M. Alexe, C. Harnagea, D. Hesse, and U. Gösele, Polarization imprint and size effects in mesoscopic ferroelectric structures, *Applied Physics Letters* **79**, 242–244 (2001)

[10] A. Roelofs, T. Schneller, K. Szot, and R. Waser, Piezoresponse force microscopy of lead titanate nanograins possibly reaching the limit of ferroelectricity, *Applied Physics Letters* **81**, 5231–5233 (2002)

[11] S. Clemens, T. Schneller, A. van der Hart, F. Peter, and R. Waser, Registered Deposition of Nanoscale Ferroelectric Grains by Template-Controlled Growth, *Advanced Materials* **17**, 1375–1361 (2005)

[12] S. Clemens, T. Schneller, R. Waser, A. Rüdiger, F. Peter, S. Kronholz, T. Schmitz, and S. Tiedke, Integration of ferroelectric lead titanate nanoislands for direct hysteresis measurements, *Applied Physics Letters* **87**, 142904 (2005)

[13] A. Gruverman, O. Auciello, and H. Tokumoto, Scanning force microscopy for the study of domain structure in ferroelectric thin films, *Journal of Vacuum Science & Technology B: Microelectronics and Nanometer Structures* **14**, 602–605 (1996)

[14] A. Gruverman, O. Auciello, and H. Tokumoto, Nanoscale investigation of fatigue effects in Pb(Zr,Ti)O_3 films, *Applied Physics Letters* **69**, 3191–3193 (1996)

[15] T. Hidaka, T. Maruyama, M. Saitoh, N. Mikoshiba, M. Shimizu, T. Shiosaki, L. A. Wills, R. Hiskes, S. A. Dicarolis, and J. Amano, Formation and observation of 50 nm polarized domains in $PbZr_{1-x}Ti_xO_3$ thin film using scanning probe microscope, *Applied Physics Letters* **68**, 2358–2359 (1996)

[16] L. M. Eng, H.-J. Güntherodt, G. Rosenman, A. Skliar, M. Oron, M. Katz, and D. Eger, Nondestructive imaging and characterization of ferroelectric domains in periodically poled crystals, *Journal of Applied Physics* **83**, 5973–5977 (1998)

[17] L. M. Eng, H.-J. Güntherodt, G. A. Schneider, U. Kopke, and J. M. Saldana, Nanoscale reconstruction of surface crystallography from three-dimensional polarization distribution in ferroelectric barium–titanate ceramics, *Applied Physics Letters* **74**, 233–235 (1999)

[18] M. Abplanalp, L. Eng, and P. Günter, Mapping the domain distribution at ferroelectric surfaces by scanning force microscopy, *Applied Physics A: Materials Science & Processing* **66**, S231 (1998)

[19] A. Roelofs, U. Böttger, R. Waser, F. Schlaphof, S. Trogisch, and L. M. Eng, Differentiating 180° and 90° switching of ferroelectric domains with three-dimensional piezoresponse force microscopy, *Applied Physics Letters* **77**, 3444–3446 (2000)

[20] E. L. Colla, S. Hong, D. V. Taylor, A. K. Tagantsev, N. Setter, and K. No, Direct observation of region by region suppression of the switchable polarization (fatigue) in Pb(Zr,Ti)O_3 thin film capacitors with Pt electrodes, *Applied Physics Letters* **72**, 2763–2765 (1998)

[21] S. V. Kalinin, E. Karapetian, and M. Kachanov, Nanoelectromechanics of piezoresponse force microscopy, *Physical Review B (Condensed Matter and Materials Physics)* **70**, 184101 (2004)

[22] S. V. Kalinin, *Nanoscale Electric Phenomena at Oxide Surfaces and Interfaces by Scanning Probe Microscopy*, Dissertation, University of Pennsylvania (2002)

[23] C. Harnagea, M. Alexe, D. Hesse, and A. Pignolet, Contact resonances in voltage-modulated force microscopy, *Applied Physics Letters* **83**, 338–340 (2003)

[24] D. A. Scrymgeour and V. Gopalan, Nanoscale piezoelectric response across a single antiparallel ferroelectric domain wall, *Physical Review B (Condensed Matter and Materials Physics)* **72**, 024103 (2005)

[25] T. Otto, S. Grafström, and L. M. Eng, Electric Field Modeling in Anisotropic Dielectrics, *Ferroelectrics* **303**, 149–153 (2004)

[26] C. Harnagea, A. Pignolet, M. Alexe, and D. Hesse, Piezoresponse Scanning Force Microscopy: What Quantitative Information Can We Really Get Out of Piezoresponse Measurements on Ferroelectric Thin Films, *Integrated Ferroelectrics* **44**, 113–124 (2002)

[27] M. E. Lines and A. M. Glass, *Principles and applications of ferroelectrics and related materials*, Clarendon Press (1977)

[28] F. Jona and G. Shirane, *Ferroelectric crystals*, Clarendon Press (1962)

[29] B. A. Strukov and A. Levanyuk, *Ferroelectric phenomena in crystals*, Springer (1998)

[30] B. Jaffe, W. Cook, and H. Jaffe, *Piezoelectric ceramics*, Academic Press (1971)

[31] J. Nye, *Physical Properties of Crystals*, Clarendon Press Oxford (1985)

[32] A. Roelofs, *Size Effects in Ferroelectric Thin Films*, Dissertation RWTH Aachen (2004), ISBN 3-89700-405-4

[33] D. Damjanovic, Ferroelectric, dielectric and piezoelectric properties of ferroelectric thin films and ceramics, *Reports on Progress in Physics* **61**, 1267–1324 (1998)

[34] Y. Xiao, V. B. Shenoy, and K. Bhattacharya, Depletion Layers and Domain Walls in Semiconducting Ferroelectric Thin Films, *Physical Review Letters* **95**, 247603 (2005)

[35] T. Schmitz, K. Prume, B. Reichenberg, A. Roelofs, R. Waser, and S. Tiedke, In-situ compensation of the parasitic capacitance for nanoscale hysteresis measurements, *Journal of the European Ceramic Society* **24**, 1145–1147 (2004)

[36] W. J. Merz, The Electric and Optical Behavior of $BaTiO_3$ Single-Domain Crystals, *Physical Review* **76**, 1221 (1949)

[37] W. L. Zhong, B. D. Qu, P. L. Zhang, and Y. G. Wang, Thickness dependence of the dielectric susceptibility of ferroelectric thin films, *Physical Review B* **50**, 1237512380 (1994)

[38] W. L. Zhong, Y. G. Wang, P. L. Zhang, and B. D. Qu, Phenomenological study of the size effect on phase transitions in ferroelectric particles, *Physical Review B* **50**, 698703 (1994)

[39] M. E. Caspari and W. J. Merz, The Electromechanical Behaviour of $BaTiO_3$ Single Domain Crystals, *Physical Review* **80**, 1082 (1950)

[40] I. N. Bronstein and K. A. Semendjajew, *Teubner-Taschenbuch der Mathematik*, B. G. Teubner Stuttgart (1996)

[41] M. Dawber, I. Szafraniak, M. Alexe, and J. F. Scott, Self-patterning of arrays of ferroelectric capacitors: description by theory of substrate mediated strain interactions, *Journal of Physics: Condensed Matter* **15**, L667 (2003)

[42] H. Fujisawa, M. Okaniwa, H. Nonomura, M. Shimizu, and H. Niu, Ferroelectricity of the 1.7 nm-high and 38 nm-wide self-assembled $PbTiO_3$ island, *Journal of the European Ceramic Society* **24**, 1641–1645 (2004)

[43] A. Roelofs, T. Schneller, K. Szot, and R. Waser, Towards the limit of ferroelectric nanosized grains, *Nanotechnology* **14**, 250–253 (2003)

[44] H. F. Kay and J. W. Dunn, Thickness Dependence of the Nucleation Field of Triglycine Sulphate, *Philosophical Magazine* **7**, 2027 (1962)

[45] M. Dawber, P. Chandra, P. B. Littlewood, and J. F. Scott, Depolarization corrections to the coercive field in thin-film ferroelectrics, *Journal of Physics: Condensed Matter* **15**, L393 (2003)

[46] K.-H. Hellwege (Editor), *Landolt-Börnstein Condensed Matter III*, volume 36A1, Springer-Verlag Heidelberg (1981)

[47] F. Peter, A. Rüdiger, R. Dittmann, R. Waser, K. Szot, B. Reichenberg, and K. Prume, Analysis of shape effects on the piezoresponse in ferroelectric nanograins with and without adsorbates, *Applied Physics Letters* **87**, 082901 (2005)

[48] W. Schätzing (Editor), *FEM für Praktiker*, Expert Verlag (2003)

[49] F. Matthews (Editor), *Finite element modelling of composite materials and structures*, CRC Press (2000)

[50] K. Prume, Private Communication

[51] ANSYS theory reference, Release 8.1

[52] R. Lerch, Simulation of Piezoelectric Devices by Two- and Three-Dimensional Finite Elements, *IEEE Trans. on Ultrasonics, Ferroelectrics, and Frequency Control* **37**, 233 (1990)

[53] H. Allik and T. J. R. Hughes, Finite Element Method for Piezoelectric Vibration, *International Journal for Numerical Methods in Engineering* **2**, 151–157 (1970)

[54] ANSYS element reference, Release 8.1

[55] K. Prume, R. Waser, K. Franken, and H. R. Maier, Finite-Element Analysis of Ceramic Multilayer Capacitors: Modeling and Electrical Impedance Spectroscopy for a Nondestructive Failure Test, *Journal of the American Ceramic Society* **83**, 1153–1159 (2000)

[56] D. Brandon and W. D. Kaplan, *Microstructural Characterization of Materials*, John Wiley & Sons (1999)

[57] D. P. Woodruff and T. A. Delchar (Editors), *Modern Techniques of Surface Science*, Cambridge University Press (1994)

[58] G. Binnig, H. Rohrer, C. Gerber, and E. Weibel, Tunneling through a controllable vacuum gap, *Applied Physics Letters* **40**, 178–180 (1982)

[59] R. Wiesendanger, *Scanning Probe Microscopy and Spectroscopy*, Cambridge University Press (1994)

[60] D. Sarid, *Scanning Force Microscopy*, Oxford University Press (1994)

[61] D. Sarid and V. Elings, Review of scanning force microscopy, *Journal of Vacuum Science and Technology B* **9**, 431–437 (1991)

[62] D. A. Bonnell (Editor), *Scanning probe microscopy and spectroscopy: theory, techniques and applications*, Wiley-VCH (2001)

[63] C. Bai, *Scanning tunneling microscopy and its application*, Springer (2000)

[64] C. J. Chen, *Introduction to Scanning Tunneling Microscopy*, Oxford University Press (1993)

[65] J. A. Stroscio and W. J. Kaiser (Editors), *Scanning tunneling microscopy*, Academic Press (1993)

[66] D. P. DiLella, J. H. Wandass, R. J. Colton, and C. R. K. Marrian, Control systems for scanning tunneling microscopes with tube scanners, *Review of Scientific Instruments* **60**, 997–1002 (1989)

[67] M. Okano, K. Kajimura, S. Wakiyama, F. Sakai, W. Mizutani, and M. Ono, Vibration isolation for scanning tunneling microscopy, *Journal of Vacuum Science & Technology A: Vacuum, Surfaces, and Films* **5**, 3313–3320 (1987)

[68] Y. Kuk and P. J. Silverman, Scanning tunneling microscope instrumentation, *Review of Scientific Instruments* **60**, 165–180 (1989)

[69] G. Meyer and N. M. Amer, Novel optical approach to atomic force microscopy, *Applied Physics Letters* **53**, 1045–1047 (1988)

[70] A. L. Weisenhorn, P. K. Hansma, T. R. Albrecht, and C. F. Quate, Forces in atomic force microscopy in air and water, *Applied Physics Letters* **54**, 2651–2653 (1989)

[71] K.-H. Grote (Editor), *Dubbel Taschenbuch für den Maschinenbau*, Springer (2004)

[72] F. Peter, A. Rüdiger, R. Waser, K. Szot, and B. Reichenberg, Comparison of in-plane and out-of-plane optical amplification in AFM measurements, *Review of Scientific Instruments* **76**, 046101 (2005)

[73] R. Waser (Editor), *Nanoelectronics and Information Technology*, Wiley-VCH (2003)

[74] J. Kerssemakers, *Concepts of interactions in local probe microscopy*, Dissertation Rijksuniversiteit Groningen (1997)

[75] T. J. Senden and W. A. Ducker, Experimental Determination of Spring Constants in Atomic Force Microscopy, *Langmuir* **10**, 1003 (1994)

[76] J. P. Cleveland, S. Manne, D. Bocek, and P. K. Hansma, A nondestructive method for determining the spring constant of cantilevers for scanning force microscopy, *Review of Scientific Instruments* **64**, 403–405 (1993)

[77] J. M. Neumeister and W. A. Ducker, Lateral, normal, and longitudinal spring constants of atomic force microscopy cantilevers, *Review of Scientific Instruments* **65**, 2527–2531 (1994)

[78] A. Rüdiger, T. Schneller, A. Roelofs, S. Tiedke, T. Schmitz, and R. Waser, Nanosize ferroelectric oxides - tracking down the superparaelectric limit, *Applied Physics A: Materials Science & Processing* **80**, 1247–1255 (2005)

[79] A. Gruverman, A. Kholkin, A. Kingon, and H. Tokumoto, Asymmetric nanoscale switching in ferroelectric thin films by scanning force microscopy, *Applied Physics Letters* **78**, 2751–2753 (2001)

[80] C. S. Ganpule, V. Nagarajan, B. K. Hill, A. L. Roytburd, E. D. Williams, R. Ramesh, S. P. Alpay, A. Roelofs, R. Waser, and L. M. Eng, Imaging three-dimensional polarization in epitaxial polydomain ferroelectric thin films, *Journal of Applied Physics* **91**, 1477–1481 (2002)

[81] B. J. Rodriguez, A. Gruverman, A. I. Kingon, R. J. Nemanich, and J. S. Cross, Three-dimensional high-resolution reconstruction of polarization in ferroelectric capacitors by piezoresponse force microscopy, *Journal of Applied Physics* **95**, 1958–1962 (2004)

[82] G. Suyal, E. Colla, R. Gysel, M. Cantoni, and N. Setter, Piezoelectric Response and Polarization Switching in Small Anisotropic Perovskite Particles, *Nanoletters* **4**, 1339–1342 (2004)

[83] Stanford Research Systems SRS830 lock-in manual

[84] Ametek Signal Recovery, Technical note TN 1000

[85] L. Pellegrino, E. Bellingeri, I. Pallecchi, A. S. Siri, D. Marr, and A. Chincarini, $SrTiO_3$ Based Side Gate Field Effect Transistor Realized by Submicron Scale AFM Induced Local Chemical Reactions, *Journal of Electroceramics* **13**, 331–337 (2004)

[86] S. Kalinin and A. Gruverman (Editors), *Scanning Probe Microscopy - Electrical and Electromechanical Phenomena at the Nanoscale*, Springer-Verlag (2006)

[87] K. Kuepfmueller and G. Kohn, *Theoretische Elektrotechnik und Elektronik*, Springer Verlag (1993)

[88] J. Fleig and J. Maier, Point contacts in solid state ionics: finite element calculations and local conductivity measurements, *Solid State Ionics* **86-88**, 1351–1356 (1996)

[89] H. Völz, *Elektronik*, Akademie Verlag Berlin (1986)

[90] M. Alexe, C. Harnagea, W. Erfurth, D. Hesse, and U. Gösele, 100-nm lateral size ferroelectric memory cells fabricated by electron-beam direct writing, *Apllied Physics A* **70**, 247–251 (2000)

[91] A. Gruverman, Scaling effect on statistical behavior of switching parameters of ferroelectric capacitors, *Applied Physics Letters* **75**, 1452–1454 (1999)

[92] A. Gruverman, B. J. Rodriguez, A. I. Kingon, R. J. Nemanich, J. S. Cross, and M. Tsukada, Spatial inhomogeneity of imprint and switching behavior in ferroelectric capacitors, *Applied Physics Letters* **82**, 3071–3073 (2003)

[93] C. H. Ahn, T. Tybell, L. Antognazza, K. Char, R. H. Hammond, M. R. Beasley, Ø. Fischer, and J.-M. Triscone, Local, Nonvolatile Electronic Writing of Epitaxial $Pb(Zr_{0.52}Ti_{0.48})O_3/SrRuO_3$ Heterostructures, *Science* **276**, 1100 (1997)

[94] Sample provided by Dr. Pankrath, Osnabrück

[95] R. Waser, T. Schneller, S. Hoffmann-Eifert, and P. Ehrhart, Advanced Chemical Deposition Techniques - from Research to Production, *Integrated Ferroelectrics* **36**, 3–20 (2001)

[96] U. Hasenkox, C. Mitze, R. Waser, R. Arons, J. Pommer, and G. Güntherodt, Chemical Solution Deposition of Epitaxial $La_{1-x}(Ca, Sr)_xMnO_3$ Thin Films, *Journal of Electroceramics* **3**, 255 (1999)

[97] M. Chu, I. Szafraniak, R. Scholz, C. Harnagea, D. Hesse, M. Alexe, and U. Gösele, Impact of misfit dislocations on the polarization instability of epitaxial nanostructured ferroelectric perovskites, *Nature Materials* **3**, 87–90 (2005)

[98] Obtained from CrysTec GmbH, Berlin

[99] I. Szafraniak, C. Harnagea, R. Scholz, S. Bhattacharyya, D. Hesse, and M. Alexe, Ferroelectric epitaxial nanocrystals obtained by a self-patterning method, *Applied Physics Letters* **83**, 2211–2213 (2003)

[100] PZT9906, Chemat Technology, Inc.

[101] T. Schneller and R. Waser, Chemical solution deposition of ferroelectric thin films - State of the art and recent trends, *Ferroelectrics* **267**, 293–301 (2002)

[102] S. Buhlmann, P. Muralt, and S. V. Allmen, Lithography-modulated self-assembly of small ferroelectric $Pb(Zr,Ti)O_3$ single crystals, *Applied Physics Letters* **84**, 2614–2616 (2004)

[103] D. J. Jung, M. Dawber, A. Ruediger, J. F. Scott, H. H. Kim, and K. Kim, Dielectric loss peak due to platinum electrode porosity in lead zirconate titanate thin-film capacitors, *Applied Physics Letters* **81**, 2436–2438 (2002)

[104] Supplied as Fox-12 (flowable oxide), Dow Corning Inc.

[105] PM4 precision lapping & polishing machine, Logitech Ltd. (Glasgow, UK)

[106] E. Vasco, S. Karthäuser, R. Dittmann, J.-Q. He, C.-L. Jia, K. Szot, and R. Waser, Nanopatterning Using Self-Organized $SrRuO_3$ as a Template, *Advanced Materials* **17**, 281 (2005)

[107] F. Peter, K. Szot, R. Waser, B. Reichenberg, S. Tiedke, and J. Szade, Piezoresponse in the light of surface adsorbates: Relevance of defined surface conditions for perovskite materials, *Applied Physics Letters* **85**, 2896–2898 (2004)

[108] D. Brune, R. Helmborg, H. Whitlow, and O. Hunderi, *Surface Characterization*, Wiley-VCH (1997)

[109] J. F. Moulder, W. F. Stickle, P. Sobol, and K. Bomben, *Handbook of X-ray Photoelectron Spectroscopy*, Perkin-Elmer Corporation (1992)

[110] H. Sugimura, Y. Ishida, K. Hayashi, O. Takai, and N. Nakagiri, Potential shielding by the surface water layer in Kelvin probe force microscopy, *Applied Physics Letters* **80**, 1459–1461 (2002)

[111] R. J. Meyer (Editor), *Gmelins Handbuch der Anorganischen Chemie*, Verlag Chemie (1932)

[112] Obtained from MaTeck, Jülich

[113] M. Zgonik, R. Schlesser, I. Biaggio, E. Voit, J. Tscherry, and P. Gunter, Materials constants of $KNbO_3$ relevant for electro- and acousto-optics, *Journal of Applied Physics* **74**, 1287–1297 (1993)

[114] J. Halbritter, Charge transfer via interfaces, especially of nanoscale materials, *Applied Physics A: Materials Science and Processing* **68**, 153–162 (1999)

[115] W. Känzig, Space Charge Layer Near the Surface of a Ferroelectric, *Physical Review* **98**, 549 (1955)

[116] A. Roelofs, N. A. Pertsev, R. Waser, F. Schlaphof, L. M. Eng, C. Ganpule, V. Nagarajan, and R. Ramesh, Depolarizing-field-mediated 180° switching in ferroelectric thin films with 90° domains, *Applied Physics Letters* **80**, 1424–1426 (2002)

[117] P. Lehnen., J. Dec, and W. Kleemann, Ferroelectric domain structures of $PbTiO_3$ studied by scanning force microscopy, *Journal of Physics D: Applied Physics* **33**, 1932–1936 (2000)

[118] M. Abplanalp and P. Gunter, Influence of stress on the domain formation in barium-titanate films, *Ferroelectrics* **258** (2001)

[119] This equation is corrected by a factor of 2 as compared to [72].

[120] ContPt-Cantilever from Nanosensors

[121] PointProbe tips obtained from Nanosensors

[122] C. Harnagea, M. Alexe, J. Schilling, J. Choi, R. B. Wehrspohn, D. Hesse, and U. Gösele, Mesoscopic ferroelectric cell arrays prepared by imprint lithography, *Applied Physics Letters* **83**, 1827–1829 (2003)

[123] L. B. Sharos, A. Raman, S. Crittenden, and R. Reifenberger, Enhanced mass sensing using torsional and lateral resonances in microcantilevers, *Applied Physics Letters* **84**, 4638–4640 (2004)

[124] T. Kawagishi, A. Kato, Y. Hoshi, and H. Kawakatsu, Mapping of lateral vibration of the tip in atomic force microscopy at the torsional resonance of the cantilever, *Ultramicroscopy* **91**, 37–48 (2002)

[125] F. Peter, A. Rüdiger, and R. Waser, Mechanical crosstalk between vertical and lateral piezoresponse force microscopy, *Review of Scientific Instruments* **77**, 036103 (2006)

[126] K.-H. Hellwege (Editor), *Landolt-Börnstein Condensed Matter III*, volume 16A, Springer-Verlag Heidelberg (1981)

[127] S. Röhrig, Private Communication

[128] S. Hong, J. Woo, H. Shin, J. U. Jeon, Y. E. Pak, E. L. Colla, N. Setter, E. Kim, and K. No, Principle of ferroelectric domain imaging using atomic force microscope, *Journal of Applied Physics* **89**, 1377–1386 (2001)

[129] F. Peter, A. Rüdiger, K. Szot and R. Waser, *IEEE Transactions on Ultrasonics, Ferroelectrics and Frequency control*, In press

[130] A. L. Kholkin, K. G. Brooks, and N. Setter, Electromechanical properties of $SrBi_2Ta_2O_9$ thin films, *Applied Physics Letters* **71**, 2044–2046 (1997)

[131] R. Piner and R. S. Ruoff, Cross talk between friction and height signals in atomic force microscopy, *Review of Scientific Instruments* **73**, 3392–3394 (2002)

[132] M. Varenberg, I. Etsion, and G. Halperin, Crosstalk problems in scanning-by-probe atomic force microscopy, *Review of Scientific Instruments* **74**, 3569–3571 (2003)

[133] M. Such, D. E. Kramer, and M. Hersam, Reproducible lateral force microscopy measurements for quantitative comparisons of the frictional and chemical properties of nanostructures, *Ultramicroscopy* **99**, 189–196 (2004)

[134] S. Jeon, Y. Braiman, and T. Thundat, Cross talk between bending, twisting, and buckling modes of three types of microcantilever sensors, *Review of Scientific Instruments* **75**, 4841–4844 (2004)

[135] A. Gruverman, Private Communication

[136] Rastersondenmikroskop und Charakterisierungsverfahren, Patent application 10 2005 061 422.1-54 at the Deutsche Patent- und Markenamt, 22.12.2005

[137] F. Peter, J. Kubacki, K. Szot, B. Reichenberg, and R. Waser, Influence of adsorbates on the piezoresponse of $KNbO_3$, *phys. stat. sol. (a)* **203**, 616–624 (2006)

[138] F. Peter, A. Rüdiger, R. Waser, K. Szot, and B. Reichenberg, Contributions to in-plane piezoresponse on axially symmetrical samples, *Review of Scientific Instruments* **76**, 106108 (2005)

[139] F. Peter, B. Reichenberg, A. Rüdiger, R. Waser, and K. Szot, Extrinsic Contributions to Piezoresponse Force Microscopy, *Mater. Res. Soc. Symp. Proc.* **902E**, 6 (2006)

Acknowledgements

Many people have provided me with assistance, guidance and support while I was working on my PhD.

First I am greatly indebted to Prof. Dr. R. Waser for giving me the opportunity to do research at the *Institut für Festkörperforschung* of the *Forschungszentrum Jülich*, Germany in the exciting field of nanoscale ferroelectrics. I would like to thank him for giving me the freedom and resources from which I greatly benefited.

I am also indebted to Prof. Dr. H. Lüth who kindly agreed to be the co-examiner in the jury.

Furthermore I wish to express my deepest gratitude to Prof. Dr. K. Szot for his unwavering enthusiasm, relentless pursuit of excellence, superb guidance, innumerable ideas and tremendous support during my time at the research center.

I am immensely grateful and deeply indebted to Dr. A. Rüdiger for his continuous assistance. His support during my thesis is truly above and beyond the call of duty. He deserves more than the traditional “thanks”. This also applies to the many kilometers spend together cycling in the alps.

Many thanks also to B. Reichenberg for stimulating and fruitful discussions and support; M. Gebauer for his help in all problems regarding mechanics and vacuum systems; Dr. R. Dittmann, Dr. T. Schneller, S. Clemens, Dr. I. Szafraniak and Dr. M. Alexe for providing samples; Dr. K. Prume for FEM-support; Dr. A. Roelofs for introducing me into the fascinating world of the AFM; S. Röhrig for his support; my room mates J. Puchalla, Dr. R. Meyer and Dr. T. Watanabe for the great time as well as all colleagues at the *Institut für Festkörperforschung*, the *Institut für Werkstoffe der Elektrotechnik* of the *RWTH Aachen* and *aixACCT Systems GmbH* for their valuable support and many great moments spend together.

I am grateful to my family and parents for their encouragement and support.

Schriften des Forschungszentrums Jülich
Reihe Informationstechnik / Information Technology

1. **SAM - Untersuchung von Aushandlungen in Gruppen mittels Agentensimulation**
   von N. Lepperhoff (2002), VI, 278 Seiten
   ISBN: 3-89336-298-3

2. **Praxisbezogene IDL-Programmierung**
   von M. Busch, R. Bauer, H. Heer, M. Wagener (2002), XVI, 216 Seiten, 12 farb. Abb.
   ISBN: 3-89336-308-4

3. **Segmentierung von Volumendatensätzen mittels dreidimensionaler hierarchischer Inselstrukturen**
   von J.-F. Vogelbruch (2002), V, 191 Seiten, zahlr. farb. Abb.
   ISBN: 3-89336-309-2

4. **ComputerMathematik mit Maple**
   von J. Grotendorst (2003), VI, 274 Seiten mit beiliegender CD-ROM, zahlr. farb. Abb.
   ISBN: 3-89336-325-4

5. **ComputerMathematik mit Maple – Zweite überarbeitete und erweiterte Auflage**
   von J. Grotendorst (2004), VI, 294 Seiten mit beiliegender CD-ROM, zahlr. farb. Abb.
   ISBN: 3-89336-354-8

6. **The Internet in Germany: Atlas of Providers and Regions**
   by N. Lepperhoff, W. Fischer (2004), VIII, 103 pages, many coloured fig.
   ISBN: 3-89336-358-0

7. **Störstellen in Galliumnitrid-basierenden Transistoren**
   von M.J. Wolter (2004), V, 132 Seiten, 19 farb. Abb.
   ISBN: 3-89336-361-0

8. **Programming in C++: Audio-Visual Lecture of the course "Object-oriented programming in C++"**
   von B. Mohr, M. Boltes, R. Koschmieder (2004), DVD (18 hours, 22 minutes recorded in 15 sessions)
   ISBN: 3-89336-369-6

9. **Fabrication and characterization of planar Gunn diodes for Monolithic Microwave Integrated Circuits**
   by S. Montanari (2005), c. 150 pages, 26 col. fig.
   ISBN: 3-89336-396-3

10. **IDL Referenz der ICG-Daten-Struktur**
    von R. Bauer (2006), XIV, 130 Seiten
    ISBN: 3-89336-426-9

Schriften des Forschungszentrums Jülich
Reihe Informationstechnik / Information Technology

11.**Piezoresponse Force Microscopy and Surface Effects of Perovskite Ferroelectric Nanostructures**
by F. Peter (2006), 106 Seiten
ISBN: 3-89336-444-7

Band/Volume 11
ISBN 3-89336-444-7

Informationstechnik
Information Technology